PIEZOELECTRIC PROPERTIES OF III-V NITRIDES

SUBMITTED BY

LUENG CHIU MING

FOR THE DEGREE OF

MASTER OF PHILOSOPHY IN PHYSICS

AT

THE HONG KONG POLYTECHNIC UNIVERSITY

IN 1999

ACKNOWLEDGMENTS

Firstly, I would like to thank my chief supervisor Prof. Helen L.W. Chan and co-supervisor Prof. C.L. Choy for their help and invaluable suggestions throughout the period of the research work.

Thanks are also due to Dr. C. Surya and Mr. W.K. Fong of Department of Electronic and Information Engineering, The Hong Kong Polytechnic University, Hong Kong, for allowing me to use the Molecular Beam Epitaxy (MBE) facility and for their precious advice in the III -V nitride film growth. I would also thank Dr. P. Chow and Dr. M. Rosamond, SVT Associates, Inc., Prairie, MN, USA, for supplying the GaN/AlN/Si composite thin film samples.

Moreover, it is my pleasure to thank Dr. B. Sundaravel of Department of Electronic Engineering, The Chinese University of Hong Kong, Hong Kong, for his help in carrying out the Rutherford Backscattering Spectrometry (RBS) measurements.

Thanks are also due to Dr. Bernd Ploss, Dr. K.W. Kwok, Dr. K.H. Pang, and the technicians in Department of Applied Physics for their helpful discussion and technical supports throughout the work. Last, but not least, I would like to thank my family for their understanding and support.

ABSTRACT

The main objective of this work is to measure the piezoelectric coefficients of III-V nitride thin films, namely aluminum nitride (AlN) and gallium nitride (GaN), by an interferometric technique. The nitride films were grown on Si substrates by Molecular Beam Epitaxy (MBE) and were characterized by Rutherford Backscattering Spectrometry (RBS) and X-ray Diffraction (XRD). Through these measurements, the nitride films were found to consist of mainly a hexagonal wurtzite structure.

In order to grow epitaxial gallium nitride film on silicon, an aluminum nitride buffer layer is often needed, hence, some of the samples we measured are GaN/AlN/Si composite films. When a voltage is applied to a multilayer thin film, the voltage drop across each layer is determined by the ratio of the resisitivity and permittivity of the individual layer. A method to estimate the voltage drop across each layer as a function of frequency is described and used to evaluate the voltage drop across each piezoelectric layer.

A single beam Mach-Zehnder type heterodyne interferometer was used to measure the displacements induced in the piezoelectric AlN and GaN samples. Using the voltage drop estimated above, the d_{33} and d_{31} coefficients of AlN were found to be (5.10 ± 0.1) pmV^{-1} and (2.55 ± 0.1) pmV^{-1}, respectively and the d_{33} and d_{31} coefficients of GaN were found to be (2.60 ± 0.1) pmV^{-1} and (1.30 ± 0.1) pmV^{-1}, respectively.

By collating data in the literature, together with the measured d_{33} and d_{31}, computer programs were compiled to calculate the velocity curves, power flow angles and electromechanical coupling coefficients in AlN, GaN, GaAs and ZnO. These results will be used for our future work in designing surface acoustic wave (SAW) devices based on these materials.

TABLE OF CONTENTS

CHAPTER ONE INTRODUCTION

CHAPTER TWO FABRICATION AND CHARACTERIZATION OF III-V NITRIDE FILMS

CHAPTER THREE RESISTIVITY AND DIELECTRIC PERMITTIVITY OF AlN AND GaN

CHAPTER FOUR MEASUREMENT OF PIEZOELECTRIC COEFFICIENTS BY OPTICAL INTERFEROMETRY

CHAPTER FIVE PIEZOELECTRIC COEFFICIENTS OF GALLIUM NITRIDE AND ALUMINUM NITRIDE

LIST OF SYMBOLS

A	*area of electrode*
C	*capacitance*
c	*elastic stiffness*
D	*electrical displacement*
d, e, g, h	*piezoelectric coefficient*
E	*electric field*
R	*resistance*
S	*strain*
s	*elastic compliance*
T	*stress*
t	*thickness*
u	*displacement*
V	*voltage*
v_a	*phase velocity*
v_e	*group velocity*
Z	*impedance*
β	*electrical impermittivity*
ω_r	*relaxation frequency*
ω_B	*Bragg cell frequency*
ω_L	*Laser frequency*
ε_o	*permittivity of free space*
ε	*electrical permittivity*
ρ	*density, resistivity*
λ	*wavelength*
Γ	*Christoffel matrix*

CHAPTER ONE

INTRODUCTION

1.1 Thesis Outline and Significance of the Work

"Piezo" is a Greek word meaning "to press"; so it follows that piezoelectricity means electricity induced by pressure. A piezoelectric crystal with electrodes on both sides not only can act as a capacitor for storing electrical energy, but also as a motor for converting electrical energy into mechanical energy, and as a generator for converting mechanical energy into electrical energy [1, p.1]. Only insulating solids and crystals without a center of symmetry have a piezoelectric effect. When a solid has a centre of symmetry, no piezoelectric effect can occur because no net dipole moment is produced. Most crystalline materials are anisotropic and they do not have the same properties in all directions. Crystals can be classified into 32 classes on the basis of the symmetry they possess. Of these 32 classes, 20 are piezoelectric and 12 are not [1, p.1].

The magnitude of the effect is defined by various piezoelectric coefficients, which will be described later in this chapter. The piezoelectric coefficients can be measured by either the direct or converse piezoelectric effect. The direct effect means measurement of charge induced on the sample by a known mechanically stress and the converse effect is a measurement of the strain induced on the sample by a known voltage.

Recently, advances in film growth technology for III-V nitrides have led to a rapid development in devices based on AlN and GaN. These devices include blue-green lasers [2], light emitting diodes [3], ultraviolet photodetectors [4], AlGaN/GaN heterostructure field effect transistor [5, 6] and AlN bulk acoustic wave device [7]. Aluminum nitride (AlN) and gallium nitride (GaN) are usually grown in the [0001] direction (when they have the hexagonal wurtzite crystal structure) and in the [111] direction (when they have the cubic zinc blende structure). These are polar axes, hence AlN and GaN exhibit piezoelectric properties. As these nitride films can withstand high temperatures, they are uniquely suited for applications in high temperature piezoelectric and acoustic devices. For GaN films, many physical properties, measured on films prepared using different methods, have been reported [8]. However, to date, there appears to be a limited amount of measured data for piezoelectric coefficients of GaN [9], especially on a composite film of GaN on AlN buffer layer deposited on a silicon substrate. As both AlN and GaN are piezoelectric, the AlN buffer layer will enhance the piezoelectric properties of GaN when they are used as strained piezoelectric layer in a semiconductor-insulator-semiconductor (SIS) Structure [5].

The aim of the present work is to utilize the converse piezoelectric effect to measure the piezoelectric coefficient of III-V nitride compounds, namely, AlN and GaN. The mechanical strain induced by an applied voltage is measured using a Mach-Zehnder type heterodyne interferometer.

Chapter 1 describes the fundamental of piezoelectricity, tensors and matrix representation and the problem arises in measuring the piezoelectric coefficients in thin film samples.

Chapter 2 describes the fabrication and characterizations of the thin film samples. The characterization methods include Rutherford Backscattering Spectrometry (RBS) and X-Ray Diffractometry (XRD). The crystal quality, crystal structure and orientation can be obtained by these characterizations.

Since all the samples can be considered as a multilayer structure, i.e.multilayer thin films and substrate, Chapter 3 describes methods to measure the resistivity and dielectric permittivity of the samples. The measured data are used to estimate the potential drop across each layer of the samples which are important parameters essential for the calculation of the piezoelectric coefficients.

Chapter 4 describes the setup of the Mach-Zehnder type heterodyne interferometer. Principles of detection, limitations of the method and the calibration results are also discussed.

Chapter 5 describes the measurements of piezoelectric coefficients (d_{33} and d_{31}) of AlN and GaN films. Details of the experiments are also discussed.

In Chapter 6, three computer programs have been compiled to calculate the phase velocities, power flow angles and electromechanical coupling coefficientsin different materials, including GaN, AlN, GaAs and ZnO. These three parameters are important for our future work in using these materials in acoustic sensors.

The last chapter is conclusions and suggestions for future work.

1.2 Fundamental of Piezoelectricity

1.2.1 The Piezoelectric Effect

If a stress is applied to a certain type of crystal, it develops an electric dipole moment with magnitude proportional to the applied stress. This phenomenon is called the direct piezoelectric effect. However, the converse piezoelectric effect is: when an electric field is applied to a certain crystal, the shape of the crystal changes. Eq. (1.1) shows the equation for the direct piezoelectric effect:

$$D = dT \tag{1.1}$$

where D is the electric displacement, d is the piezoelectric coefficient, and T is the applied mechanical stress. Existence of the converse piezoelectric effect is a thermodynamic consequence of the direct effect and the coefficients relating the field and the strain in the converse effect are the same as those relating the stress and the electric displacement in the direct effect. Therefore the converse effect can be written as below;

$$S = dE \tag{1.2}$$

Hence, the piezoelectricity is a coupling between the mechanical and electrical constants. The mechanical variables can be either the stress or strain, while the electrical constants can be the electrical displacement or electric field [10, p.115] and four different piezoelectric coefficients d, e, g and h are defined as:

$$d = \left(\frac{\partial D}{\partial T}\right)_E = \left(\frac{\partial S}{\partial E}\right)_T \tag{1.3}$$

$$e = \left(\frac{\partial D}{\partial S}\right)_E = \left(\frac{\partial T}{\partial E}\right)_S \tag{1.4}$$

$$g=\left(\frac{\partial E}{\partial T}\right)_D=\left(\frac{\partial S}{\partial D}\right)_T \qquad (1.5)$$

$$h=\left(\frac{\partial E}{\partial S}\right)_D=\left(\frac{\partial T}{\partial D}\right)_S \qquad (1.6)$$

where e and h are referred to as the piezoelectric stress coefficients and d and g are referred to the piezoelectric strain coefficients [12]. Each of these coefficients has two forms. One corresponds to the direct effect while the other corresponds to the converse piezoelectric effect. Not all of the four piezoelectric coefficients are independent variables, the following equations show the relation between them [11, p.17];

$$d=\varepsilon g=es \qquad (1.7)$$

$$e=\varepsilon h=dc \qquad (1.8)$$

$$g=\beta d=hs \qquad (1.9)$$

$$h=\beta e=gc \qquad (1.10)$$

where s and c are the elastic compliance and stiffness, respectively, while ε and β are the electrical permittivity and impermittivity, respectively.

1.2.2 Piezoelectric Constitutive Equations

The piezoelectric constitutive equations can be derived from the thermodynamic functions. For example, the Gibbs free energy, and the Helmholz free energy [11, p.16]. These equations assumed that the interaction between the mechanical and the electrical systems are reversible and isothermal.

Table 1.1 shows the piezoelectric constitutive equations in which the superscripts correspond to the measurement of those parameters under certain boundary conditions. More details of these parameters will be given in the next section.

Independent variables	Fundamental	Equations
	Direct effect	*Converse effect*
(S,E)	$D = eS + \varepsilon^S E$	$T = c^E S + eE$
(T,D)	$E = -gT + \beta^T D$	$S = s^D T + gD$
(S,D)	$E = -hS + \beta^S D$	$T = c^D S + hD$
(T,E)	$D = dT + \varepsilon^T E$	$S = s^E T + dE$

Table 1.1 The piezoelectric constitutive equations [11, p.16].

1.2.3 Piezoelectric Effects and the Elastic and Dielectric Constants

The parameters used to describe the piezoelectric properties are the elastic constants, dielectric constants and piezoelectric coefficients. The definition of piezoelectric properties is a coupling between the mechanical and electrical constants. Therefore, the mechanical properties are affected by the electrical properties and vice versa.

Consider the case when we applied a mechanical stress to a piezoelectric material, the strain induced in the material is not only determined by the stress, but also by the electrical conditions. An electrically clamped state is defined when the polarization is constant, while an electrically free state is when the surrounding medium has infinite dielectric susceptibility. Therefore, when measuring the elasticity or stiffness of piezoelectric materials, the measurement conditions must be specified. To identify the measurement conditions, a superscript is added to the parameter. The symbols c^E and s^E represent the stiffness and compliance measured under the conditions of a constant electric field (short circuit condition) , while c^D and s^D correspond to the stiffness and compliance measured under the conditions of constant dielectric displacement (open circuit condition).

Also, when we measure the dielectric constants of a piezoelectric material, the mechanical conditions needs to be specified. In most cases, two conditions are used. The first one is a clamped (constant strain) condition. In this state, the surface of the piezoelectric material is attached to a surrounding medium with infinite rigidity, so that there are no strains in the material. The other condition is a free (constant stress) state, the surface of the material is attached to a medium with infinite compliance and the piezoelectric material is free from any external stress. A superscript is added to the dielectric constant to indicate the condition under which it is measured. The dielectric permittivity measured under constant stress and strain, is represented by ε^T and ε^S, respectively.

1.2.4 The Piezoelectric Tensor and Transformation Rules

The dielectric, elastic and piezoelectric coefficients can be described in both the tensors and matrix notation. Eq. (1.2) can be written in a full tensor notation:

$$S_{jk} = d_{ijk} E_i \qquad (1.11)$$

In eq. (1.11), there are three constants, *i, j,* and *k*, with values varies from 1 to 3. The piezoelectric coefficient d_{ijk} is a third rank tensor with 27 components. As d_{ijk} has symmetry in *j* and *k*, this reduces the number of components to 18. If the material has higher symmetry, the number of independent elements will decrease further. For example, the piezoelectric coefficients of a wurtzite structure material have three non-zero components while in a cubic zinc blende structure, it has only one non-zero component.

By transformation of axes, we can change from one set of axes to another with respect to the same origin. The piezoelectric coefficients are related to a set of axes, and the axes are in turn related to the crystal axes. Suppose there is a set of axes denoted by x, and we want to rotate it to a new axes x', the transformation can be done by using the follows equation:

$$x_i' = a_{ij}x_j \qquad i,j = 1, 2, 3 \qquad (1.12)$$

Eq (1.12) is the transformation law for a first-rank tensor [11, p.9] where a_{ij} is the cosine of the angle between the new axis x_i' and the old axis x_j. The relation between the axis is shown in Figure 1.1.

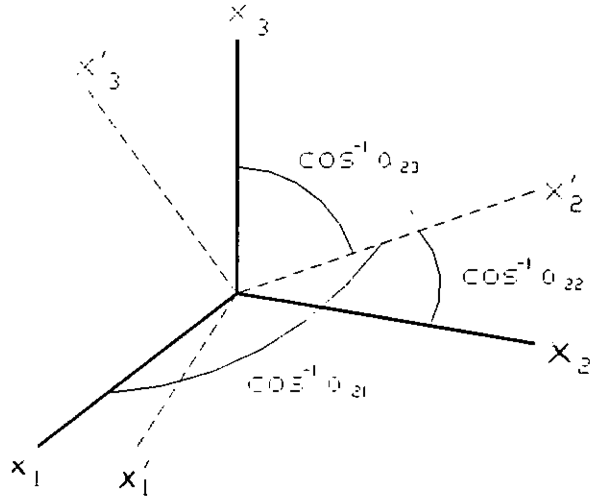

Figure 1.1 The transformation of axes.

For a third rank tensor, the tensor components can also be changed by rotation of the axes. The transformation laws of third-rank tensor is given by [11, p.111]:

$$x_{ijk}' = a_{il}a_{jm}a_{kn}x_{lmn} \qquad (1.13)$$

where x_{ijk}' is the new coordinate system, while x_{ijk} is the old one.

As the piezoelectric tensor is also a third-rank tensor, we can apply eq. (1.13) to the transformation. The piezoelectric tensor elements in the original coordinate system d_{ijk} can be transformed to d_{ijk}' using the following equation:

$$d_{ijk}' = a_{il}a_{jm}a_{kn}d_{lmn} \qquad (1.14)$$

This transformation is important for crystals grown on non-conventional growth planes.

Tensor components can be written in either a tensor notation or a matrix notation. The matrix notation relies on the symmetry of the tensor components. For example, stress, strain and permittivity are symmetric in two subscripts and we can replace the two subscripts with values running from 1 to 3 by one subscript whose value runs from 1 to 6. The replacements are shown as follows:

Table 1.2 The tensor and matrix notations.

	subscripts					
Tensor notation	11	22	33	23, 32	13, 31	12, 21
Matrix notation	1	2	3	4	5	6

According to the matrix notations, the piezoelectric constitutive equations can be simplified. Table 1.3 shows one of the constitutive equations represented by both notations.

Table 1.3 The piezoelectric constitutive equation represented by both notations.

	Tensor notation	*Matrix notation*
Direct effect	$D_i = e_{ikl} S_{kl} + \varepsilon_{ij}^{S} E_k$	$D_i = e_{iq} S_q + \varepsilon_{ik}^{S} E_k$
Converse effect	$T_{ij} = c_{ijkl}^{E} S_{kl} - e_{kij} E_k$	$T_p = c_{pq}^{E} S_q - e_{kp} E_k$

The stress, strain, dielectric and elastic coefficients can be also transformed by using the above notation. For example, T_{12} becomes T_6 and s_{1223} becomes s_{64}.

However, in order to keep the constitutive equations simple, there are some addition rules used in the strain, compliance and the piezoelectric *d* and *g* tensors. These equations are [12, p.239, 245]:

$$S_i = S_{pq} \quad \text{when } p = q,\ i = 1, 2, 3 \tag{1.15}$$

$$S_i = 2S_{pq} \quad \text{when } p \neq q,\ i = 4, 5, 6 \tag{1.16}$$

$$d_{ip} = d_{ijk} \quad \text{when } j = k,\ p = 1, 2, 3 \tag{1.17}$$

$$d_{ip} = 2d_{ijk} \quad \text{when } j \neq k,\ p = 4, 5, 6 \tag{1.18}$$

$$s^E_{jk} = s^E_{pqmn} \quad \text{when } p = q \text{ and } m = n, j,k = 1, 2, 3 \tag{1.19}$$

$$s^E_{jk} = 2s^E_{pqmn} \quad \text{when } p = q \text{ and } m \neq n, j = 1, 2, 3,\ k = 4, 5, 6 \tag{1.20}$$

$$s^E_{jk} = 4s^E_{pqmn} \quad \text{when } p \neq q \text{ and } m \neq n, j, k = 4, 5, 6 \tag{1.21}$$

The matrix notation used two subscripts to represent four subscripts given in the tensor notation. A two dimensional array can be used to represent a tensor up to the fourth-rank. Figure 1.2 shows the physical meanings of the subscripts of the matrix notation. The subscripts 1, 2, and 3 denote the directions along the x_1, x_2, and x_3 axes, while 4, 5, and 6 denote the shear about the axis x_1, x_2, and x_3, respectively.

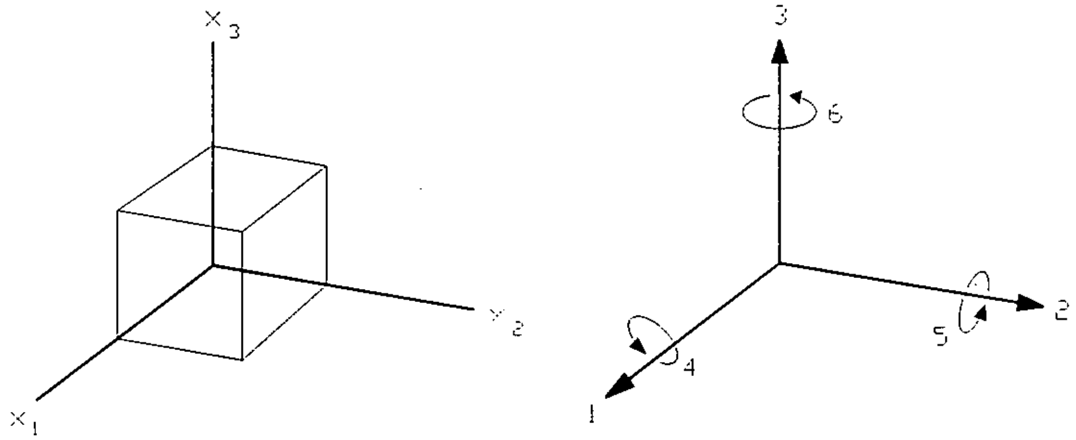

Figure 1.2 The directions represented by the subscript in the matrix notation.

1.3 Piezoelectric Coefficient Measurement in Thin Films

There is a large difference between piezoelectric coefficient measured in bulk samples and that in thin films. In the bulk samples, the sample can freely expand or contract. However, in the form of thin film, it was rigidly mounted on a thick substrate (due to the deposition process) and cannot move freely. Therefore, the measured piezoelectric coefficients cannot represent true values of the coefficients for the bulk material. This is called the substrate clamping effect, and the effect is shown in Figure 1.3.

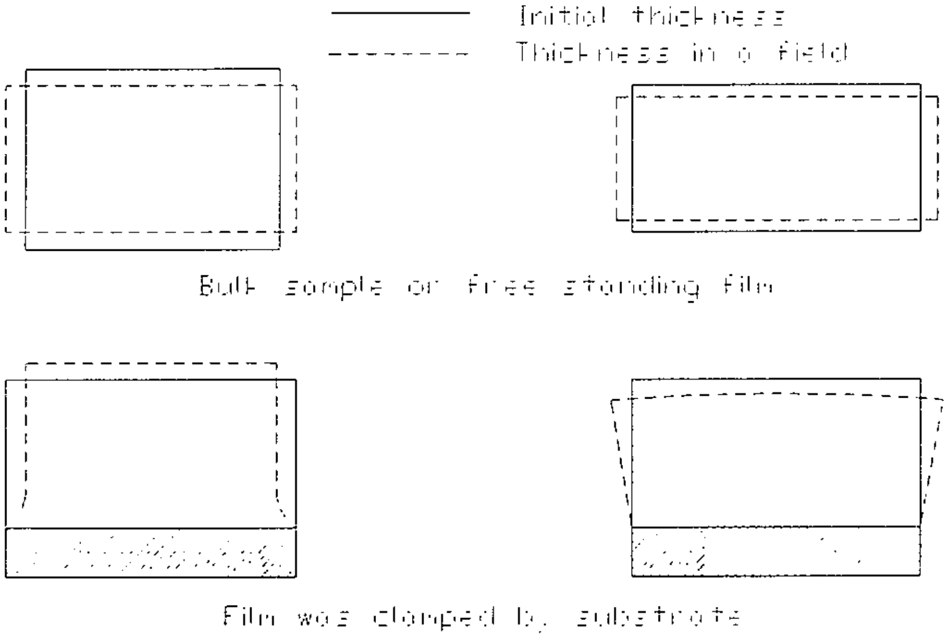

Figure 1.3 Clamping effect occurred in a thin film sample with a substrate.

D. Royer *et al.* suggested that one could correct for this clamping effect [13]. By recalling the indirect effect of the appropriate piezoelectric constitutive equations (Table 1.1), we have:

$$S_j = s_{jk}^E T_k + d_{ij} E_i \qquad j, k = 1 \text{ to } 6;\ i = 1 \text{ to } 3 \qquad (1.22)$$

Assuming that a sample changing its length in the x_1 direction while it is mounted to a support that is free of stress. Eq. (1.22) becomes $S_1=d_{11}E_1$ due to the absence of stress in any direction. We can obtain the piezoelectric coefficient d_{11} by integrating over the length of the sample. Hence, $u=-d_{11}v$, where u is the displacement on the free surface and v is the applied voltage.

However, if a thin film sample is rigidly mounted to a thick substrate and the film cannot freely expand or contract, the piezoelectric coefficient measured is modified by the stresses induced in the piezoelectric thin film. The modification of the coefficients depends on the symmetry and the orientation of the piezoelectric thin film samples.

For an aluminum nitride thin film with z-direction grown on a silicon substrate. There is no displacement induced in the x_1 and x_2 directions at the interface between the film and the substrate (i.e. $u_1 = u_2 = 0$). Therefore, the strain components S_1, S_2, and S_6 are equal to zero. Suppose the measurements are carried out at frequencies well below the resonance frequency of the sample, these assumptions can be held in the whole thickness of the sample. In the same case, there is no stress in the free surface of the sample (i.e. T_3, T_4, and T_5 are equal to zero). Therefore, Eq. (1.22) becomes:

$$S_j = s_{j1}^E T_1 + s_{j2}^E T_2 + s_{j6}^E T_6 + d_{3j} E_3 \qquad (1.23)$$

and eq. (1.23) can be expanded into:

$$S_1 = s_{11}^E T_1 + s_{12}^E T_2 + s_{16}^E T_6 + d_{31} E_3 = 0 \qquad (1.24)$$

$$S_2 = s_{21}^E T_1 + s_{22}^E T_2 + s_{26}^E T_6 + d_{32} E_3 = 0 \qquad (1.25)$$

$$S_6 = s_{61}^E T_1 + s_{62}^E T_2 + s_{66}^E T_6 + d_{36} E_3 \qquad (1.26)$$

Considering the compliance and piezoelectric matrix for the 6mm (wurtzite) symmetry:

$$s_{jk} = \begin{bmatrix} s_{11} & s_{12} & s_{13} & 0 & 0 & 0 \\ s_{12} & s_{11} & s_{13} & 0 & 0 & 0 \\ s_{13} & s_{13} & s_{33} & 0 & 0 & 0 \\ 0 & 0 & 0 & s_{44} & 0 & 0 \\ 0 & 0 & 0 & 0 & s_{44} & 0 \\ 0 & 0 & 0 & 0 & 0 & 2(s_{11} - s_{12}) \end{bmatrix} \qquad (1.27)$$

$$d_{3j} = \begin{bmatrix} 0 & 0 & 0 & 0 & d_{15} & 0 \\ 0 & 0 & 0 & d_{15} & 0 & 0 \\ d_{31} & d_{31} & d_{33} & 0 & 0 & 0 \end{bmatrix} \qquad (1.28)$$

From the compliance matrix, we found that $s_{11} = s_{22}$, $s_{12} = s_{21}$, s_{16}, s_{26}, s_{61} and s_{62} are equal to zero. Moreover, from the piezoelectric matrix, we found that $d_{31} = d_{32}$ and $d_{36} = 0$.

Combining the above information obtained from the compliance and piezoelectric matrix as well as eqs. (1.24) – (1.26), we obtain:

$$T_6 = 0 \qquad \text{and} \qquad T_1 = T_2 = \frac{-d_{31}E_3}{\left(s_{11}^E + s_{12}^E\right)} \qquad (1.29)$$

From eq. (1.23), we obtained:

$$S_3 = s_{31}^E T_1 + s_{32}^E T_2 + s_{36}^E T_6 + d_{33}E_3 \qquad (1.30)$$

Substituting eq. (1.29), and $T_6 = 0$ into eq. (1.30), the equation becomes:

$$S_3 = \left(d_{33} - 2\left(\frac{s_{31}^E d_{31}}{s_{11}^E + s_{12}^E}\right)\right)E_3 \qquad (1.31)$$

Since the piezoelectric coefficients was measured using the converse effect, the measured coefficient $d_{33}' = S_3 / E_3$ with the substrate clamping effect is:

$$d_{33}' = \frac{S_3}{E_3} = d_{33} - 2\left(\frac{s_{31}^E d_{31}}{s_{11}^E + s_{12}^E}\right) = d_{33} - \delta_{33} \qquad (1.32)$$

where δ_{33} is the correction term. Rearranging eq. (1.32), we obtain [13]:

$$d_{33} = d_{33}' + 2\left(\frac{s_{31}^E d_{31}}{s_{11}^E + s_{12}^E}\right) \qquad (1.33)$$

In eq. (1.33), d_{33}' is the piezoelectric coefficient measured by using the laser interferometer (having substrate clamping), and the second term should be added to the measured d_{33}' to obtain the true value of d_{33}.

CHAPTER TWO

FABRICATION AND CHARACTERIZATION OF III-V NITRIDE FILMS

2.1 III-V Nitride Film Grown by Molecular Beam Epitaxy

2.1.1 Introduction

Molecular Beam Epitaxy (MBE) is a versatile technique for growing thin epitaxial semiconductor, metal or insulator films [14-16]. In MBE, the thin film grows through reactions between the molecular or atomic beams of the constituent elements and a substrate surface, and the growing condition is maintained at an elevated temperature and in ultrahigh vacuum. The composition of the grown epilayer and its doping level depend on the relative arrival rates of the constituent elements and the dopants, which in turn depend on the evaporation rates of the appropriate sources. The growth rate is about 1 monolayer per second, which is low enough for the surface migration of the impinging species on the growing surface so that the surface of the grown film is smooth. A simple mechanical shutter placed in front of the beam sources can be used to start or to stop the deposition and doping of the film [17, p.1].

The major difference between MBE and other vacuum deposition techniques is that beam fluxes and growth conditions in MBE can be more precisely controlled. MBE growth is carried out under conditions far from thermodynamic equilibrium and is governed mainly by the kinetics of surface processes occurring when the impinging beams react with the outermost atomic layers of the substrate crystal. This is different from other epitaxial growth techniques such as the liquid or vapor phase epitaxy, which proceeds at conditions near thermodynamic equilibrium and are most frequently controlled by diffusion processes occurring in the crystallizing phase surrounding the substrate [17, p.1].

In the present work, the III-V nitride films were grown using a SVTA BLT-N35 MBE with conventional thermal sources (K-cells) as the group III elements (Al and Ga). Nitrogen (N_2) gas cannot be directly used for the AlN or GaN growth and must be dissociated prior to reaching the surface of the substrate in order to form the AlN or GaN. The technique used to break the nitrogen molecule is to apply a 13.56 MHz RF energy using a SVTA RF plasma source to form a nitrogen plasma. The atomic nitrogen and the group III elements then react to form AlN or GaN on a substrate.

2.1.2 Sample Preparation

2.1.2.1 AlN films

AlN films were prepared by a MBE system installed in The Hong Kong Polytechnic University Electronic and Information Engineering Department (PolyU EIE). Si (111) was used as the substrate because Miyauchi *et al.* have successfully obtained epitaxial AlN on this substrate by MBE [18]. The substrate was cleaned by ultrasonic degreasing processes and etched in buffered HF to remove the oxides on the surface of the silicon. The substrate was then transferred into the MBE chamber. In the deposition chamber, the substrate was thermally cleaned at 940°C for 1 hour. The substrate temperature was then decreased to about 600°C and the AlN thin film started to grow. AlN film of about 450 nm thick was deposited at a growth rate of ~0.60 μm/hr.

2.1.2.2 GaN films

GaN/AlN/Si(111) and GaN/AlN/Si(100) thin films were grown on Si (111) and Si (100) with AlN buffer layers, respectively. The AlN buffer layer is essential for the epitaxial growth of GaN on Si substrates [19]. The thickness of the GaN films are 140 nm, while the AlN buffer layer is about 30 nm on both the (111) and (100) silicon substrates. The films were grown by P. Chow and M. Rosamond in SVT Associates, Inc., Eden Prairie, MN, USA using a similar molecular beam epitaxy (MBE) system.

GaN film on Si(111) was prepared by the MBE system at the PolyU EIE department. In order to grow GaN thin films with wurtzite structure on silicon (111) substrates, Morimoto *et al.* (1973) [20] and T.D. Moustakas *et al.* (1993) [21] suggested that an amorphous GaN buffer layer can be used instead of AlN. The Si substrate was cleaned by a degreasing process and etched in buffered HF before being transferred into the MBE chamber. A two-step growth of GaN was used. A GaN buffer layer was deposited on the substrate at a substrate temperature of 500°C for 3 minutes. After that the substrate was heated up to a higher temperature at about 730°C and a GaN film of about 640 nm thick was growth at a growth rate of ~0.59 μm/hr.

2.2 Film Characterization by Rutherford Backscattering Spectrometry (RBS)

2.2.1 Introduction

Rutherford backscattering spectrometry (RBS) is performed by bombarding a sample with a monoenergetic beam of high energy particles. The most common case is using helium with energy of a few MeV. The RBS studies were carried out in the Department of Electronic Engineering, the Chinese University of Hong Kong. The incident helium ion beam has an energy of 2 MeV and a lateral resolution of 1 mm. Some of the incident ions are scattered backwards from the heavier atoms near the surface region of the sample and their energy measured by a solid state detector. The energy of the backscattered atoms is related to the depth of penetration and to the mass of the atom in the sample. However, the number of backscattered particles detected for any given element is proportional to its concentration.

There are several common uses of RBS analysis: quantitative depth profiling, concentration measurements, and crystal quality and impurity analysis. In this work, we used RBS to find the quantitative depth profiling and the crystal quality.

2.2.2 Basic Principles of RBS

RBS was named after Lord Ernest Rutherford who first presented the concept of atoms having nuclei and the working principles of RBS base on collisions between atomic nuclei. When a sample is bombarded with high-energy particles, most incident particles implant into the sample and remain inside the material because the diameter of atomic nucleus is ~ 10^{-4} Å, while the spacing between nuclei is ~ 1 Å. Only a small amount of particles directly collides with the nuclei of the atoms in the sample and the collision process can be modeled as an elastic collision using classical physics.

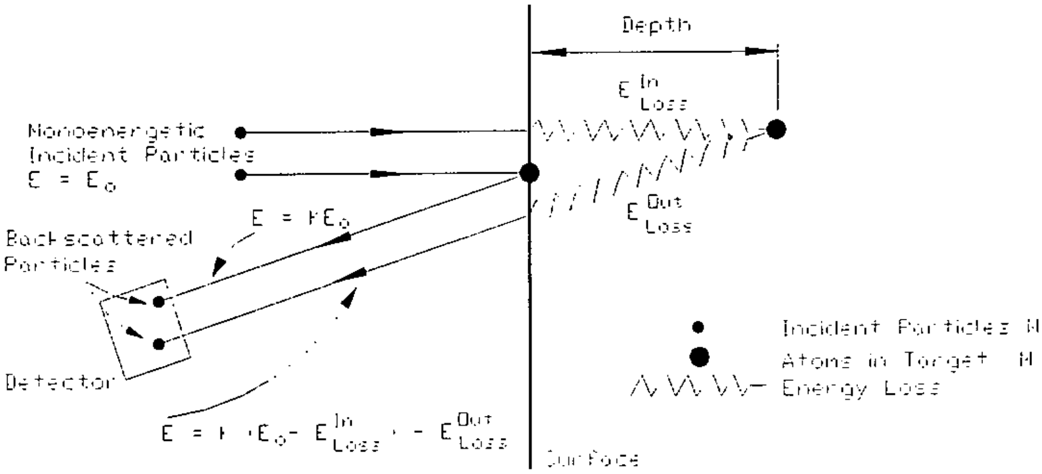

Figure 2.1 A schematic diagram showing the various energy loss processes for backscattering from a given depth in a sample [22, p.478]

The energy of the backscattered particles detected depends upon two processes. The first one is the loss of energy due to the transfer of momentum to the sample nucleus, while the other is the loss of energy during transmission along the sample material (attenuation loss). Figure 2.1 shows a schematic diagram of the backscattering of particles occurring at the surface of sample and at a depth *d* in the sample.

The ratio of the energy after collision to the energy before collision (E_1/E_0) is defined as the kinematic factor *K* [22, p.478]:

$$K = \left(\frac{\sqrt{1-((M_1/M_2)\sin\theta)^2} + (M_1/M_2)\cos\theta}{1+(M_1/M_2)} \right)^2 \qquad (2.1)$$

where M_1 is the mass of the incident probe particle, M_2 is the mass of the target atom, and θ is the angle between the path of the probe particle before and after scattering.

In our work, the probe particles are He atoms (2 MeV) and the attenuation loss is in the range of 100-800 eV/nm depending on the composition and density of the sample. For the same element, the deeper the probe particle penetrates, the lower the energy measured by the detector. Hence, RBS can be used to determine the thickness of layers and the depth profiling.

The other characteristic of RBS is that it is more sensitive if the target consists of light elements because of the larger momentum transferred from the probe particle to a light target atom. The heavier the mass of the target atom, the lower is the momentum transfer. Therefore RBS has a good mass resolution for light elements, but poor mass resolution for heavy elements. For example, it is possible to resolve C from O but it is not possible to resolve W from Ta when these elements are present at the same depths in the sample.

RBS is a technique not only can give the elemental composition information, but also can be used to study the structure of a single crystal sample [23, p.37; 24, p.10]. The meaning of a sample being channelled is that the rows of atoms in the sample are aligned parallel to the incident ion beam. The probe particles will also be backscattered from the first few monolayers of the sample similar to a non-aligned sample. However, the backscattering from other atoms in the lattice will be greatly reduced due to the channelling. For example, the backscattered signal from a single crystal Si sample being channelling aligned will only be 3 – 5 % of the signal from the same sample, which is not aligned. The c-factor can be defined as the ratio of the integrated signal obtained from the aligned spectrum to the random spectrum. The film is polycrystalline when the c-factor is 100% while the c-factor is close to 0 for a single crystal film. Therefore, by measuring the reduction in the backscattered signal when a sample is channelled, it is possible to profile the crystal perfection of a sample, and/or to determine its crystal orientation.

2.2.3 Experimental Results

2.2.3.1 AlN grown on Si (111)

Figure 2.2 shows typical RBS spectra of the AlN/Si(111) thin film sample with the incident beam along a random direction and the beam aligned along the [0001] direction of AlN. In the random spectrum, the region around channel number 520 is due to the He ions backscattered by Al atoms at the surface while the region around channel number 230 is due to the probe particles backscattered by N atoms. The width of the Al signal peak can be used to estimate the size of the crystalline cluster in the film. By using a RBS program GISA3, the cluster size in AlN film is estimated to be 235 nm if the density of AlN is assumed to be 3255 kgm^{-3} [25]. The other information obtained from Figure 2.2 is the c-factor of the AlN thin film. By integrating both the aligned and the random backscattered signal arose from the Al atoms (channel number 500-520), the ratio of them will give the c-factor of the thin film. From the figure, the c-factor of the AlN film is estimated to be 97 %.

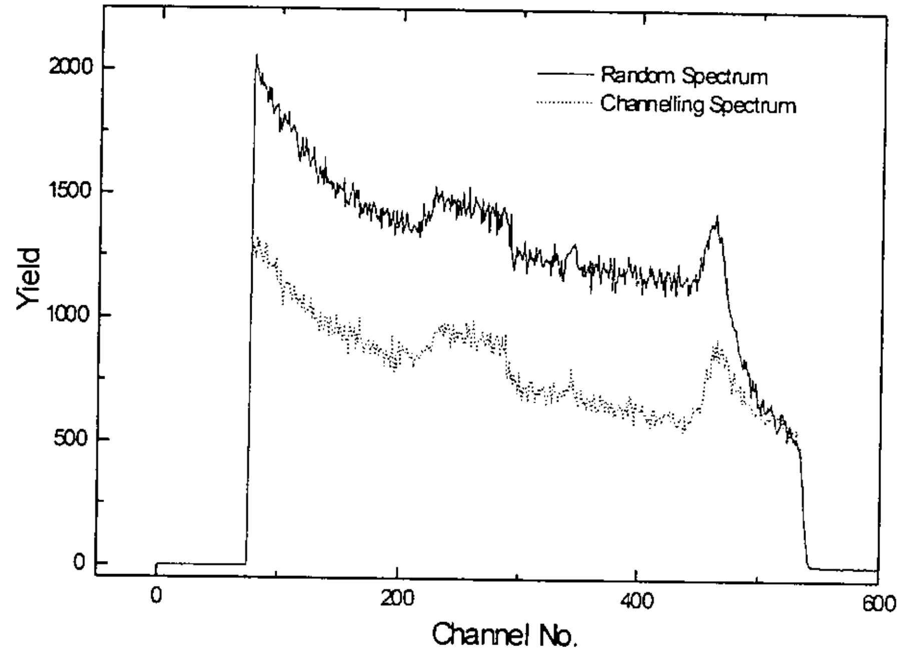

Figure 2.2 RBS spectra of the AlN/Si(111) thin film sample with the incident beam along a random direction and the beam aligned along the [0001] direction of AlN.

2.2.3.2 GaN grown on Si (111)

Figure 2.3 shows a RBS spectra of the GaN/Si(111) thin film sample with the incident beam along a random direction and the beam aligned along the [0001] direction of the GaN. In the spectra, the region around channel number 760 are due to the He ions backscattered by Ga atoms at the surface. There is a tailing (not a clear edge at around channel number 650) in the Ga signal which indicates that there are different sizes of GaN clusters in the film. By using a RBS program, the GaN cluster size is estimated to range from 350 to 720 nm if the density of GaN is assumed to be 6100 kgm^{-3} [25]. By integrating both of the aligned and random backscattered signal arose from the Ga atoms (channel number 720-760), the c-factor of the GaN film is found to be 64 %.

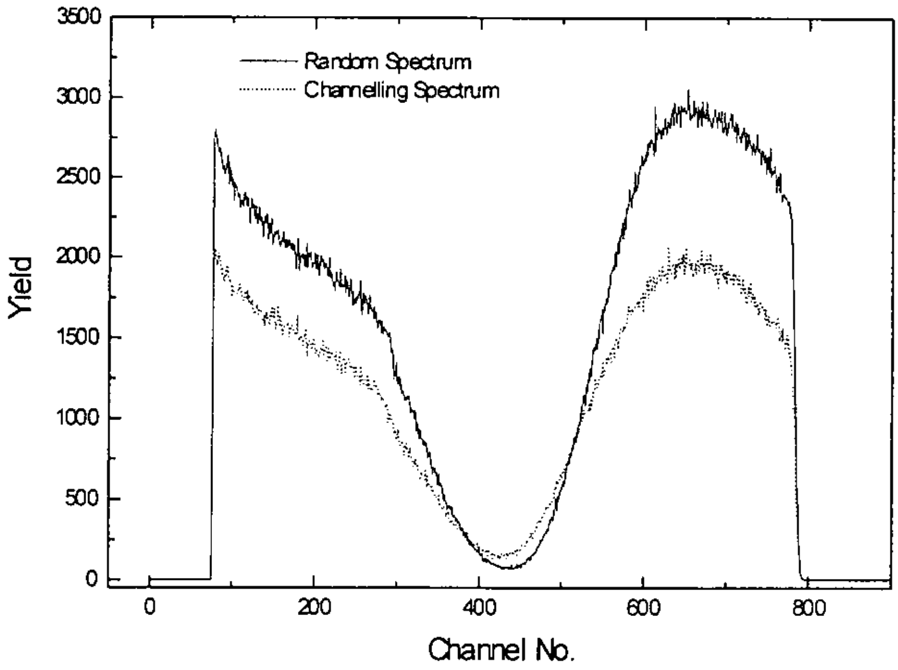

Figure 2.3 RBS spectra of the GaN/Si(111) thin film sample with the incident beam along a random direction and the beam aligned along the [0001] direction of GaN.

2.2.3.3 GaN with AlN buffer layer grown on Si (111)

Figure 2.4 shows the RBS spectra of the GaN/AlN/Si(111) thin film sample with the incident beam along a random direction and the beam aligned along the [0001] direction of GaN. In the spectra, there are also tailing in the Ga signal. By using a RBS program, the GaN cluster size is estimated to range from 40 to 120 nm if the density of GaN is 6100 kgm^{-3} [25]. By integrating both of the aligned and random backscattered signal arose from Ga atoms (channel number 710-790), the c-factor of the GaN film is found to be 46 %.

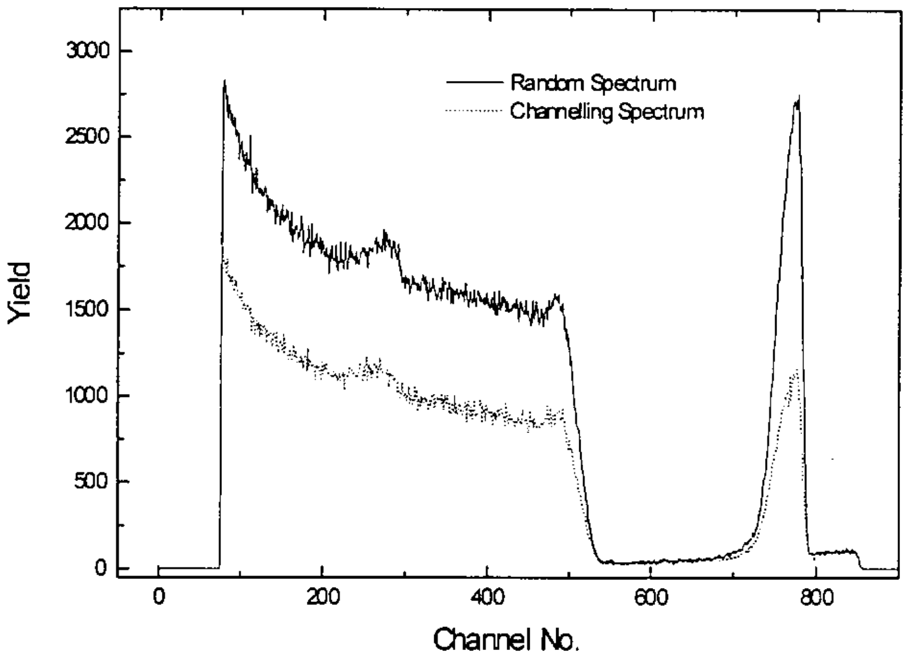

Figure 2.4 RBS spectra of the GaN/AlN/Si(111) thin film sample with the incident beam along a random direction and the beam aligned along the [0001] direction of GaN.

To further investigate the in-plane orientation of GaN and Si(111), azimuthal angular scans for GaN and Si are taken at a tilt angle of 5°. (Figures 2.5 and 2.6) The dips in the spectra correspond to channeling in different planes. For example, in Figure 2.5, the dips in the scan correspond to channeling in GaN planes, while the dips in Figure 2.6 correspond to channeling in Si planes. We can see dips correspond to planes in GaN and Si at the same angular positions which implies that the in-plane orientation is GaN $[11\bar{2}0] \parallel$ Si $[\bar{1}10]$.

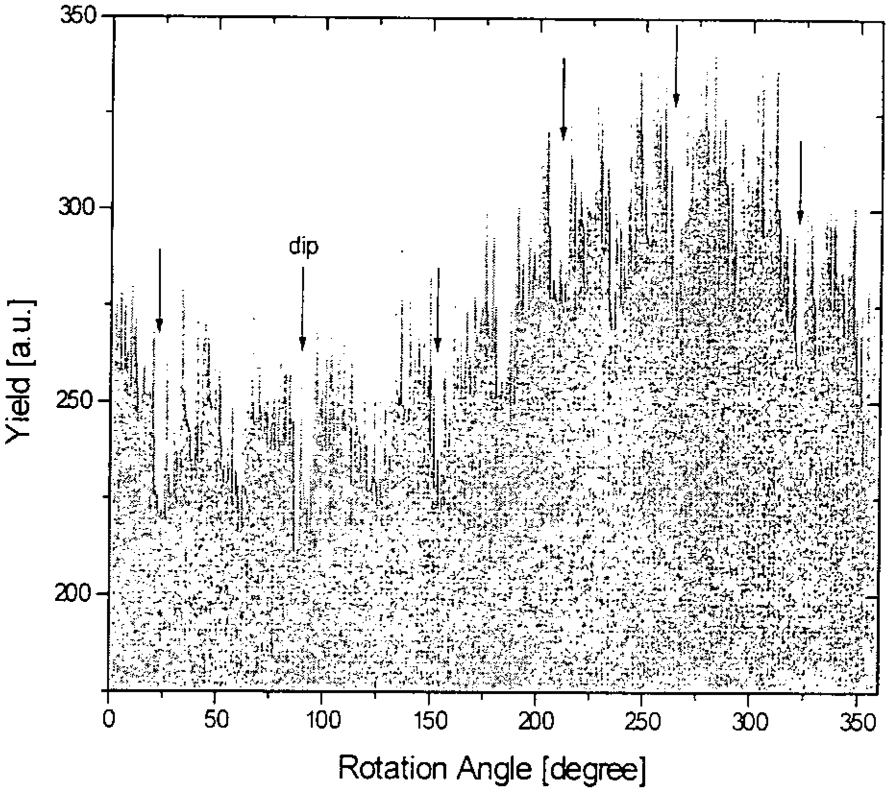

Figure 2.5 Azimuthal angular scan of GaN at a tilt angle of 5°.

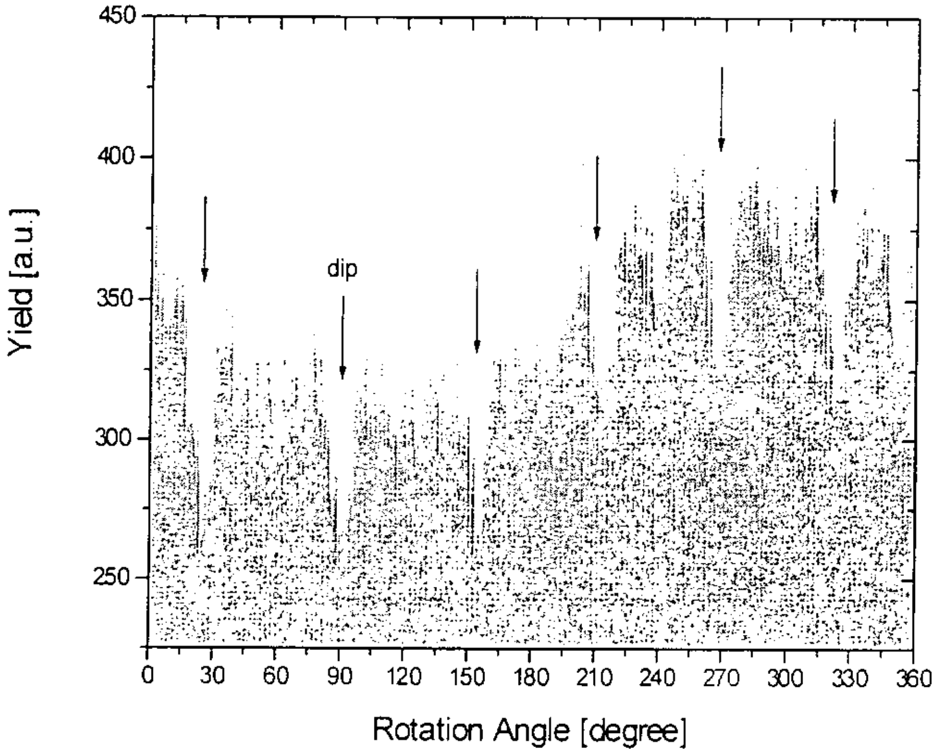

Figure 2.6 Azimuthal angular scan of silicon at a tilt angle of 5°.

Figure 2.7 and Figure 2.8 show the tilt angular scans of the RBS yield near the surface about the [0001] axis of the GaN and the [111] axis of the Si substrate, respectively. By comparing the angular scans, the minimum yield for Ga signal from the film and Si signal from the substrate are found at the same angular position, indicating that there is no angular misorientation between the [0001] GaN and [111] Si directions.

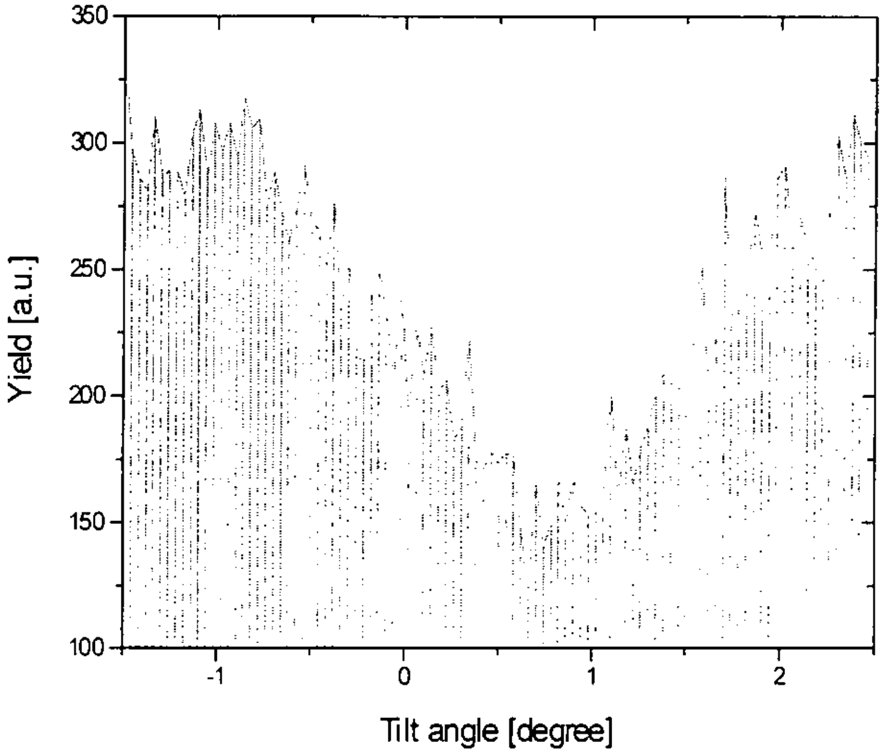

Figure 2.7 Tilt angular scan from GaN in the [0001] axis.

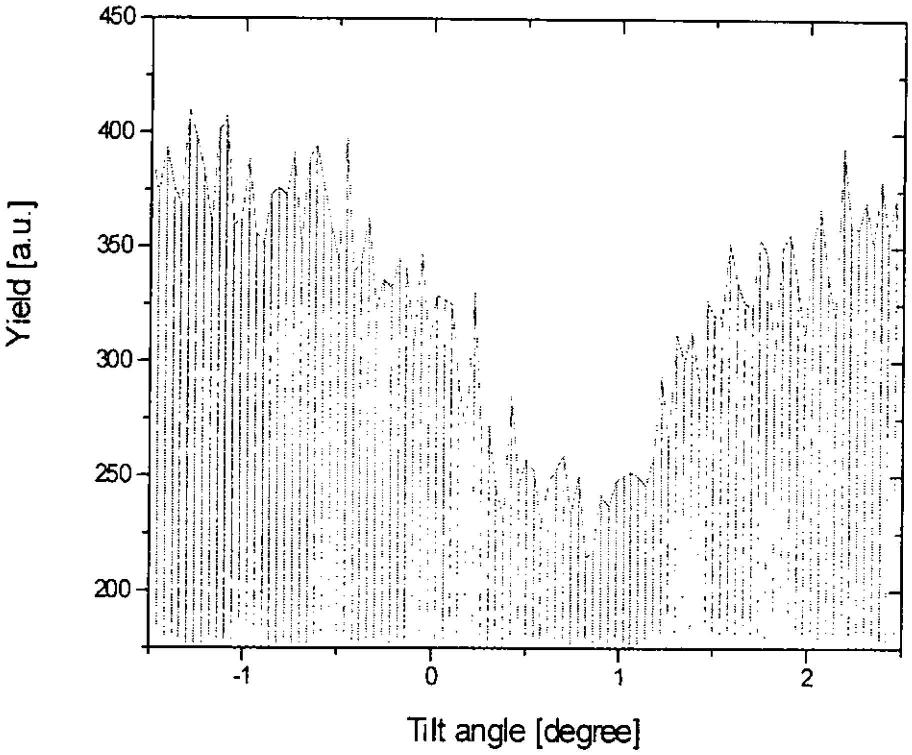

Figure 2.8 Tilt angular scan from silicon in the [111] axis.

2.2.3.4 GaN with AlN buffer layer grown on Si (100)

Figure 2.9 shows the RBS spectra of the GaN/AlN/Si(100) thin film sample with the incident beam along a random direction and the beam aligned along the [0001] direction of GaN. In the spectra, there are also tailings in the Ga signal, and by using a RBS program, the GaN cluster size is estimated to range from 50 to 150 nm when the density of GaN is 6100 kgm^{-3} [25]. By integrating both of the aligned and random backscattered signal arose from Ga atoms (channel number 720-790), the c-factor of the GaN film is found to be 80 %.

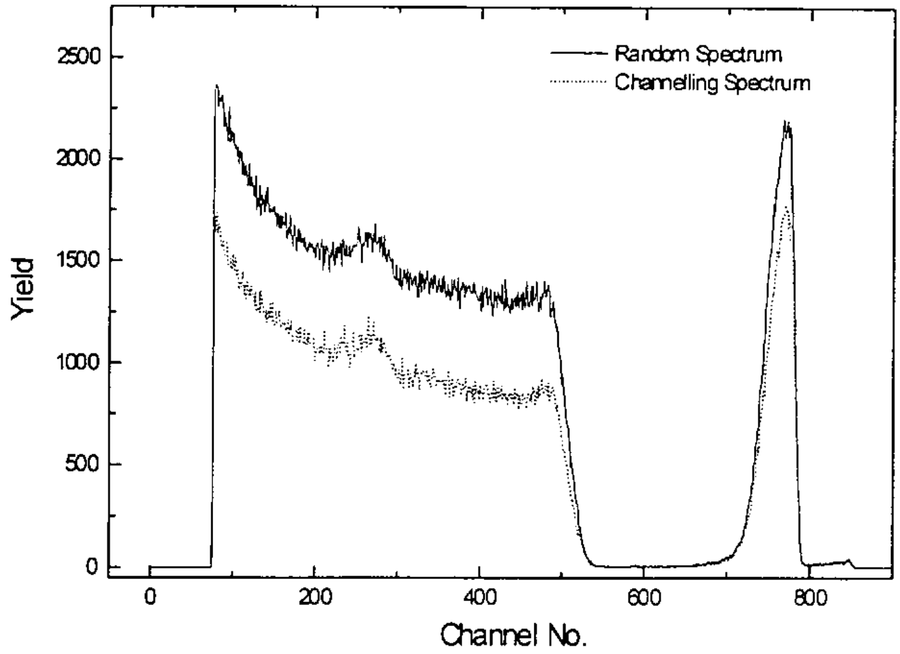

Figure 2.9 RBS spectra of the GaN/AlN/Si(100) thin film sample with the incident beam along a random direction and the beam aligned along [0001] direction of GaN.

2.2.4 Conclusions

Table 2.1: A summary of results obtaining from the RBS measurements.

Sample No	*thickness*	*Cluster Size (nm)*	*C-factor (%)*
1) AlN/Si(111)	450nm/0.3mm	235	97
2) GaN/Si(111)	640nm/0.3mm	350 – 720	64
3) GaN/AlN/Si(111)	140nm/30nm/0.3mm	40 – 120	46
4) GaN/AlN/Si(100)	140nm/30nm/0.3mm	50 – 150	80

Table 2.1 shows a summary of results obtained from the RBS measurements. By comparing the c-factor of sample 2 and sample 3 on a similar Si (111) substrate, it is found that the crystal quality of GaN is better when an AlN buffer layer is used. Amano *et al.* [19] reported that using an AlN buffer layer was used in the growth of GaN film, could improve the GaN morphology and minimize the defect density resulting from substrate lattice mismatch [8]. In sample 3, from the RBS measurements, it is found that the in-plane orientation is GaN $[11\bar{2}0] \parallel$ Si $[\bar{1}10]$ and there is no angular misorientation (tilting) between the [0001] GaN and [111] Si directions.

It is important to measure these parameters as when we measure the piezoelectric coefficient d_{33} of GaN, we need to identify the pointing direction of the *c*-axis of the GaN film. If the *c*-axis of the GaN film has a tilting relative to the substrate orientation, the d_{33} will be underestimated.

2.3 Film Characterization by X-Ray Diffraction (XRD)

2.3.1 Introduction

X-Ray diffraction (XRD) is a powerful technique for identifying the crystalline phases existed in a material. It can be used to measure the structural properties of the materials such as strain, grain size, epitaxy, composition, preferred orientation, and defect structure.

XRD is a non-contact and non-destructive measurement and can be used for in-situ studies. Materials composed of different elements can be analyzed with XRD. However, XRD is more sensitive to elements with higher atomic numbers because the diffracted intensities from these elements are much stronger. Therefore, the sensitivity of XRD depends on the material of interest. When the diffracted intensities are small, a larger film specimen is required and the information obtained is an average over a large area.

Thin-film XRD is important in many technical applications. For example, in the analyses of semiconductor and optical materials, XRD can be used to measure the orientation, strain state, and defects in epitaxial thin films. These parameters are important as they affect the electronic and optical properties of the films.

2.3.2 Basic Principles of XRD

Figure 2.10 shows the basic setup of a XRD system. The diffraction angle 2θ is the angle between the incident and diffracted X rays. In the XRD measurements, the diffracted intensity is measured as a function of 2θ and the orientation of the specimen, which then yields the diffraction pattern. In the present study, the wavelength λ of the X-ray is 0.1540 nm.

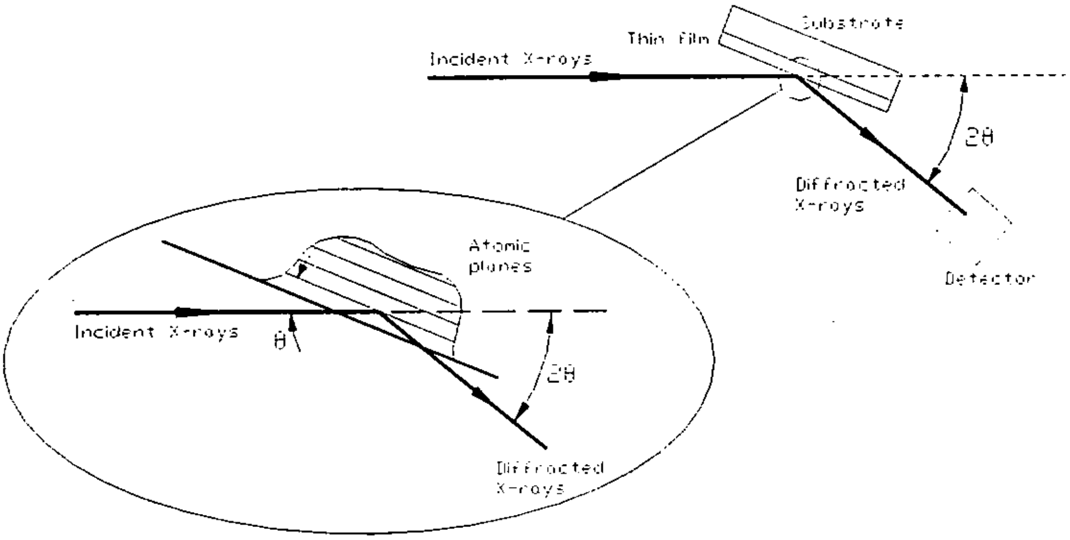

Figure 2.10 Basic features of an XRD system [26, p.200].

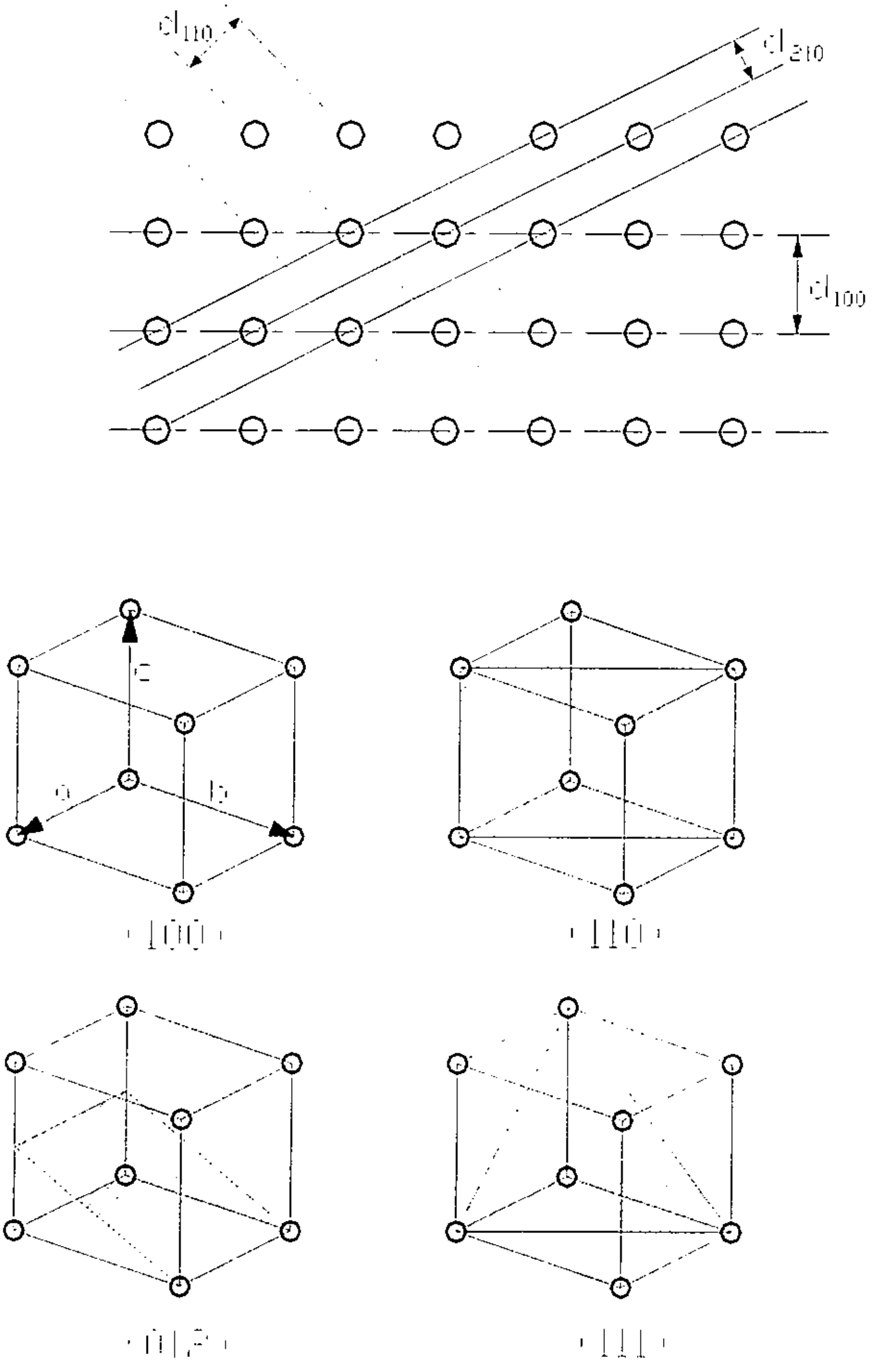

Figure 2.11 Several atomic planes and their d-spacings in a cubic crystal [26, p.201].

Figure 2.11 shows crystal planes of atoms that are spaced with a distance d apart. However, they can be resolved into many different atomic planes with different d spacings. In order to identify them, a coordinate system is introduced with unit vectors a, b, and c. Let us consider a cubic crystal with $a = b = c$, an orthogonal system can be formed by using these unit vectors. We can now identify any atomic plane uniquely defined by its Miller indices. These are the three reciprocal intercepts of the plane with the a-, b-, and c-axes and are reduced to the smallest integers having the same ratio. Therefore, an *(hkl)* plane intercepts the crystallographic axes at a/h, b/k, and c/l. For cubic crystals, the atomic plane spacing d between *(hkl)* planes, denoted by d_{hkl}, is equal to:

$$d_{hkl} = \frac{a_o}{\sqrt{h^2 + k^2 + l^2}} \tag{2.2}$$

where a_o is the lattice constant of the crystal. However, for a hexagonal structure, the atomic planes would have another representation, *(hkil)*, which are defined by two different lattice constants, a and c of the crystal. The atomic plane spacing d between (hkil) planes, d_{hkil}, in a hexagonal structure is equal to:

$$d_{hkil} = \frac{1}{\sqrt{\left[\frac{4}{3}\frac{h^2 + k^2 + hk}{a^2} + \frac{l^2}{c^2}\right]}} \tag{2.3}$$

When there is constructive interference between X rays scattered by the atomic planes in a crystal, a diffraction peak is observed. The condition for a constructive interference from planes with spacing d_{hkl} (for cubic structure) or d_{hkil} (for hexagonal structure) is given by the Bragg's law:

$$n\lambda = 2d_{hkl}\sin\theta_{hkl} \qquad (2.4)$$

$$n\lambda = 2d_{hkil}\sin\theta_{hkil} \qquad (2.5)$$

where λ is the wavelength of the X rays, θ_{hkl} or θ_{hkil} is the angle between the atomic planes and the incident X rays beam. In order to observe the diffraction peak, the detector must be placed at the diffraction angle equal to $2\theta_{hkl}$, and the sample must be oriented with the angle between the diffracting plane and the incident X rays equal to the Bragg angle θ_{hkl}.

The orientation of crystallites in a thin film can be one of the following categories: single crystal, epitaxial, complete fiber texture, preferred orientation (incomplete fiber texture), or randomly distributed (powder). Actually, the degree of orientation not only influences the film properties, but also affect the method of measurement and identification of phases present in the thin film with multiple phases.

In the present work, we used XRD measurements to obtain the lattice constant(s) of the thin films, as well as the phase(s) existed in the samples. To obtain the lattice constants of the thin films, we can use the method described above, i.e. by measuring the diffraction peaks at the Bragg angles, then use eqs. (2.2) and (2.4) (or eqs. (2.3) and (2.5) in the case of a hexagonal crystal) to calculate *d* and the lattice constants. Tsuchiya *et al.* [27] reported that the ratio of zinc blende (cubic) to wurtzite (hexagonal) structure in a GaN sample could be estimated from the ratio of the integrated X-ray diffraction intensities of the cubic (002) and the hexagonal planes measured by omega (ω) scans. Since AlN and GaN have similar structures and properties, we can use the same method (described below) to determine the relative amounts of the two phases existed in our AlN and GaN samples.

The theoretical integrated XRD intensities I of the cubic and hexagonal GaN are calculated [27] and shown in Table 2.2. I of the cubic (002) plane was nearly equal to that from the hexagonal $(10\bar{1}1)$ plane. So, the ratio of cubic to hexagonal phases in grown GaN layer can be estimated from the ratio of the integrated XRD intensity from the cubic (002) plane to the those from the hexagonal $(10\bar{1}1)$ plane measured by an omega ω scan.

Structure	*Diffraction Peak*	*θ (deg.)*	*I ($\times 10^4$)*	*$I/I_{c\text{-}(002)}$*
	(111)	17.2	18.8	2.35
	(002)	20.0	7.98	1
Cubic	(220)	28.9	4.86	0.61
	(311)	34.5	2.10	0.26
	(222)	36.3	1.33	0.17
	$(10\bar{1}0)$	16.1	7.60	0.95
	(0002)	17.3	18.5	2.32
Hexagonal	$(10\bar{1}1)$	18.4	8.47	1.06
	$(10\bar{1}2)$	24.2	1.63	0.20
	$(11\bar{2}0)$	28.9	4.84	0.61

Table 2.2 Theoretical XRD intensities of cubic and hexagonal GaN [27].

The procedures of the measurement are that, firstly a θ-2θ scan is carried out for the nitride film. From Table 2.2, it is noted that θ of the diffraction peak of cubic (111) and hexagonal (0002) are almost identical and if a peak appears at that angle and if both phases coexist in the sample, it is very difficult to tell whether it comes from the cubic or hexagonal phase and another scan is necessary. If the sample is cubic and the cubic (111) plane has been identified in the first scan, an addition peak due to the cubic (001) plane will be found when the sample is tilted at an angle of 54.7° [27]. We can do a *θ-2θ scan* as well as *a ϕ scan* at a prescribed tilted angle to look for the peaks. While for the hexagonal phase, the (0002) peak occurs at the same position as the cubic (111) but in *a ϕ scan*, the $(10\bar{1}1)$ peak will appear at a different tilted angle of 61.9°. Hence, by looking for diffraction peaks at different tilting angles, we can identify the two phases. If both the cubic and hexagonal phases coexist in the sample, peaks can be located at tilted angles of 54.7° and 61.9°. We can then carry out a ω scan and use the ratio of the intensities of these two ω scan peaks to determine the ratio of the two phases.

2.3.3 Experimental Results

2.3.3.1 AlN grown on Si (111)

Figure 2.12 shows a XRD pattern of the AlN/Si(111) thin film sample, the 2θ peak at 36.15° may correspond to either the cubic (111) plane or the hexagonal (0002) plane. However, in a θ-2θ scan and a *ϕ scan* at a tilted angle of 54.7°, we cannot observe any diffraction peak, which indicates that there is no cubic phase in the sample.

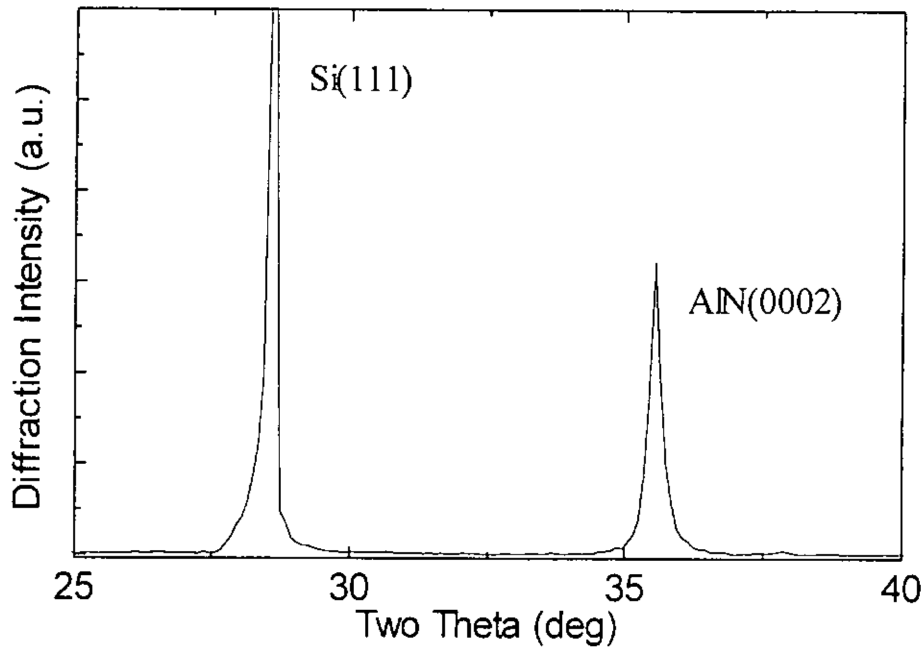

Figure 2.12 The XRD pattern of the AlN/Si(111) thin film sample.

Figures 2.13 and 2.14 show a θ-2θ *scan* and *a* ϕ *scan* pattern of the AlN/Si(111) thin film sample (tilted at 61.9°), respectively. From Figure 2.13, we can observe a peak at 37.985° corresponding to the hexagonal plane. We can now conclude that the sample consists of only hexagonal phase. By using eqs. (2.3) and (2.5), as well as $2\theta_{(0002)} = 36.150°$ and $2\theta = 37.985°$, the lattice constants of the AlN thin film are found to be: a = 3.112 Å and c = 4.970 Å. Also, from Figure 2.14, we can identify the hexagonal plane with a six-fold symmetry.

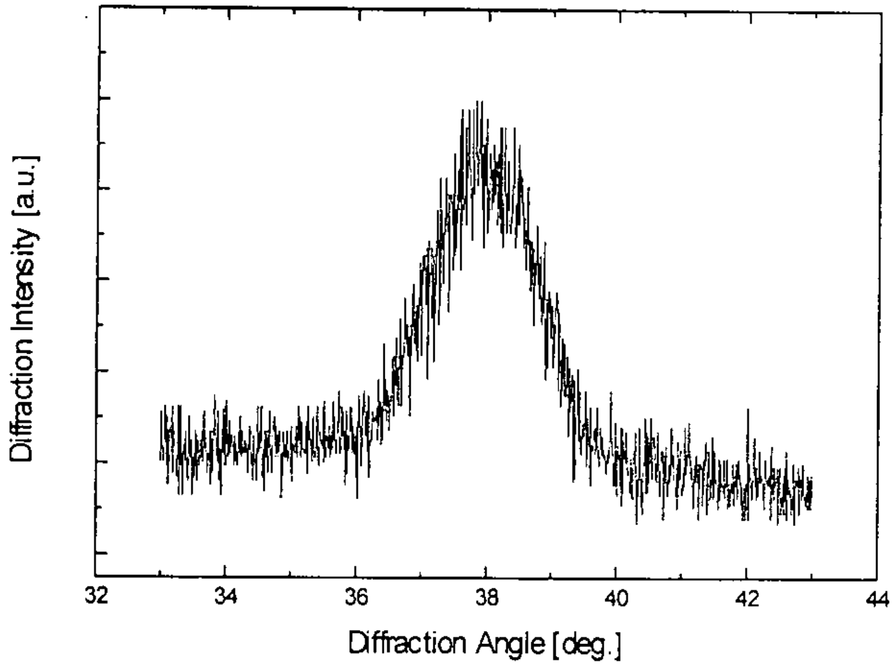

Figure 2.13 The *θ-2θscan* XRD pattern of the AlN/Si(111) thin film sample when the sample is tilted at 61.9°.

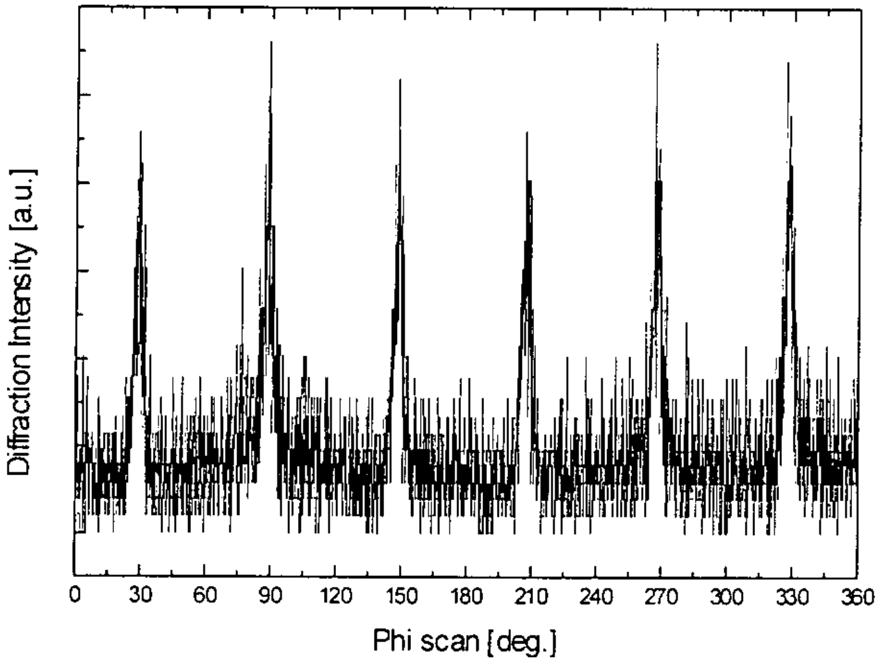

Figure 2.14 The *ϕscan* XRD pattern of the AlN/Si(111) thin film sample when the sample is tilted at 61.9°.

2.3.3.2 GaN grown on Si (111)

The results is quite similar to the AlN/Si(111) sample. Figure 2.15 shows a XRD pattern of the GaN/Si(111) thin film sample, the peak at 34.656° may correspond to either the cubic (111) plane or the hexagonal (0002) plane. However, after we have done a *θ-2θ scan* as well as *a ϕ scan* at a tilted angle of 54.7°, we cannot observe any diffraction peak which indicates that there is no cubic phase in the sample and the diffraction peak observed in the first scan corresponds to the hexagonal (0002) plane.

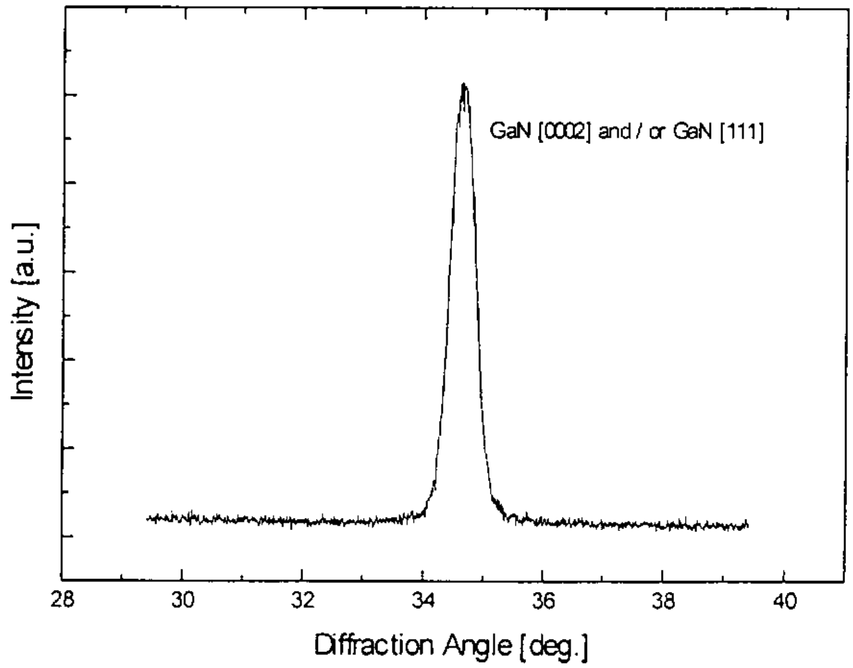

Figure 2.15 The XRD pattern of the GaN/Si(111) thin film sample.

Figures 2.16 and 2.17 show a *θ-2θscan* and *a ϕscan* pattern of the GaN/Si(111) thin film sample (tilted at 61.9°), respectively. From Figure 2.16, we can observe a peak at 36.687° corresponding to the hexagonal planes. Hence, we can conclude that the sample is only in hexagonal phase. By using eqs. (2.3) and (2.5), together with $2\theta_{(0002)}$ = 34.656° and 2θ = 36.687°, the lattice constants of the GaN thin film are found to be: a = 3.211 Å and c = 5.177 Å. From Figure 2.17, we can also observe that the hexagonal plane has a six-fold symmetry.

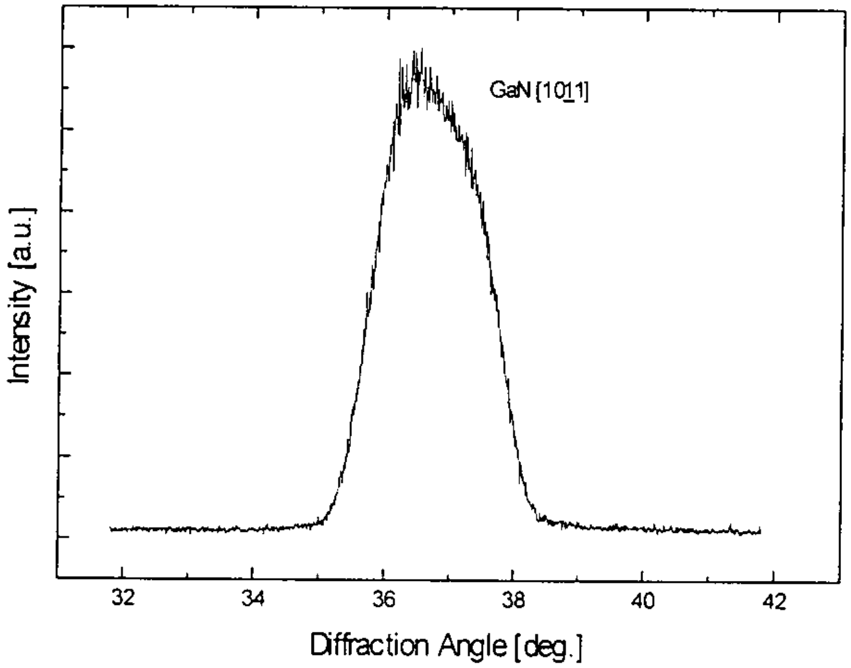

Figure 2.16 The θ-2θ *scan* XRD pattern of the GaN/Si(111) thin film sample when the sample is tilted at 61.9°.

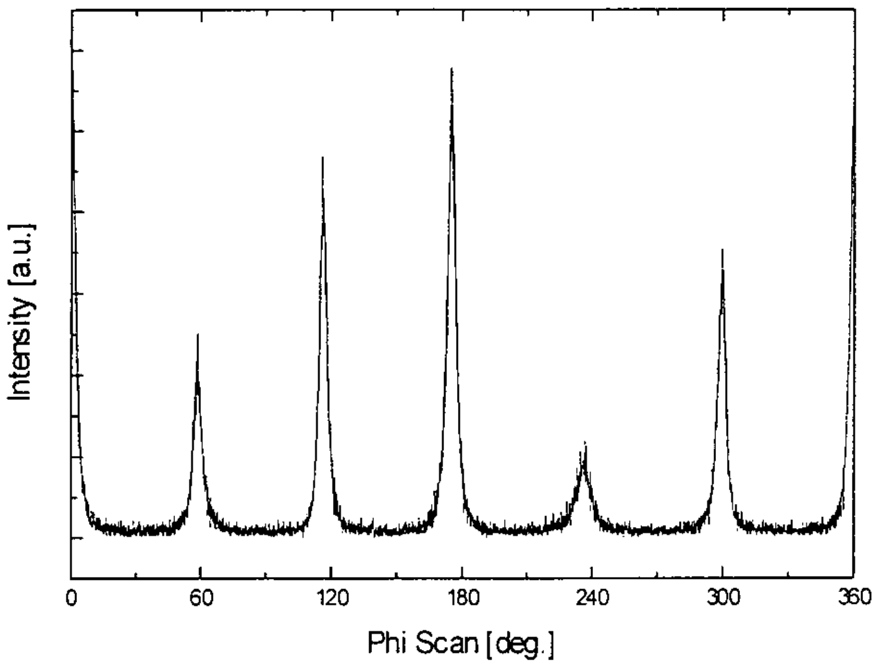

Figure 2.17 The ϕ *scan* XRD pattern of the GaN/Si(111) thin film sample when the sample is tilted at 61.9°

2.3.3.3 GaN with AlN buffer layer grown on Si (111)

Figure 2.18 shows a XRD pattern of the GaN/AlN/Si(111) thin film sample, the peak at 34.723° may correspond to either the cubic (111) plane or the hexagonal (0002) plane. After we have made a θ-2θ *scan* at a tilted angle of 54.7°, we found that a peak appears at 40.016°, which corresponded to the (002) reflection of cubic GaN (Figure 2.19).

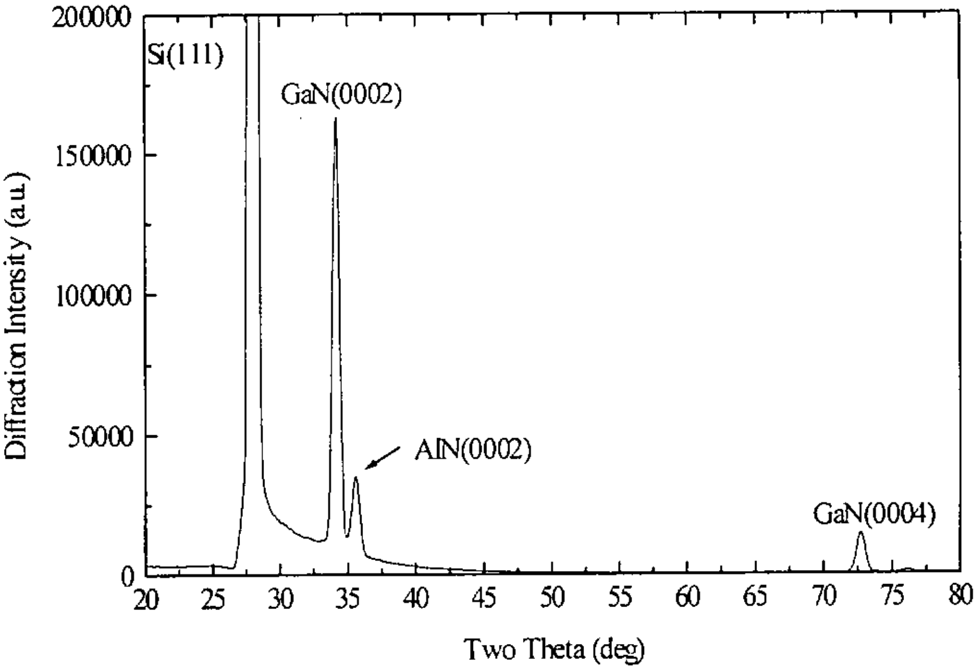

Figure 2.18 The XRD pattern of the GaN/AlN/Si(111) thin film sample.

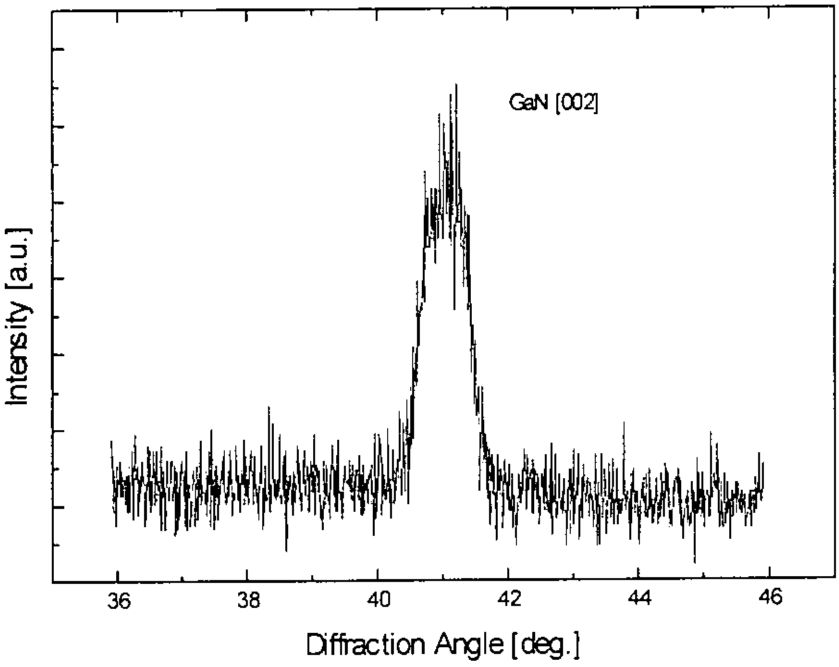

Figure 2.19 The θ-2θ *scan* XRD pattern of the GaN/AlN/Si(111) thin film sample when the sample is tilted at 54.7°.

However, when we did the θ-2θ *scan* and the ϕ *scan* of the GaN/AlN/Si(111) with the film tilted at 61.9°, we can also observe a peak at 37.223° corresponding to the hexagonal plane (Figure 2.20). By using eqs. (2.3) and (2.5), as well as the $2\theta_{(0002)}$ = 34.723° and 2θ = 37.223°, we can obtain the lattice constants of the hexagonal GaN as: a = 3.156 Å and c = 5.168 Å. While using eqs. (2.2) and (2.4) as well as $2\theta_{(002)}$ = 41.016°, the lattice constant of the cubic GaN is a = 4.401 Å. From figure 2.21, we can also observe that the hexagonal plane has a six-fold symmetry.

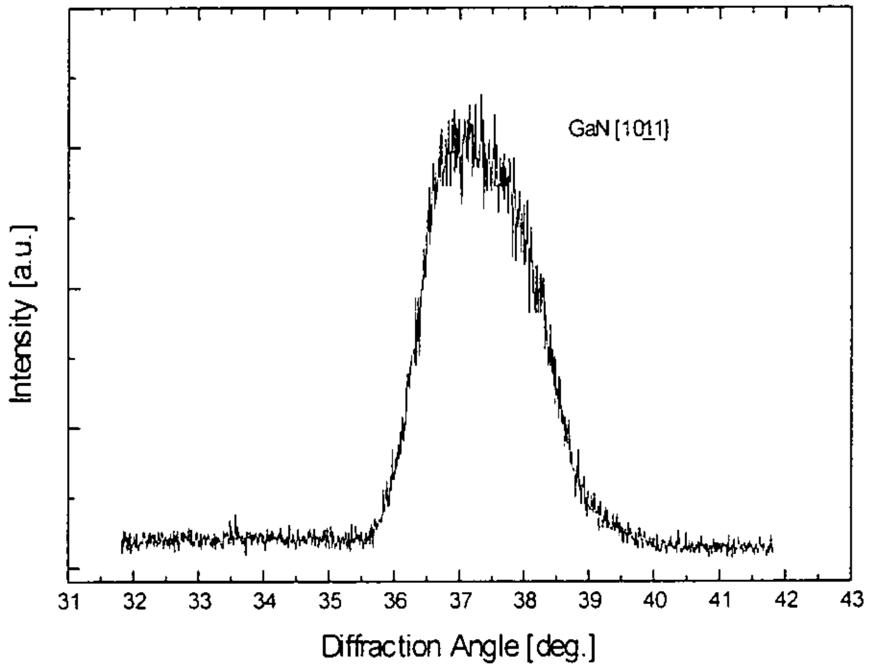

Figure 2.20 The θ-2θ *scan* XRD pattern of the GaN/AlN/Si(111) thin film sample when the sample is tilted at 61.9°.

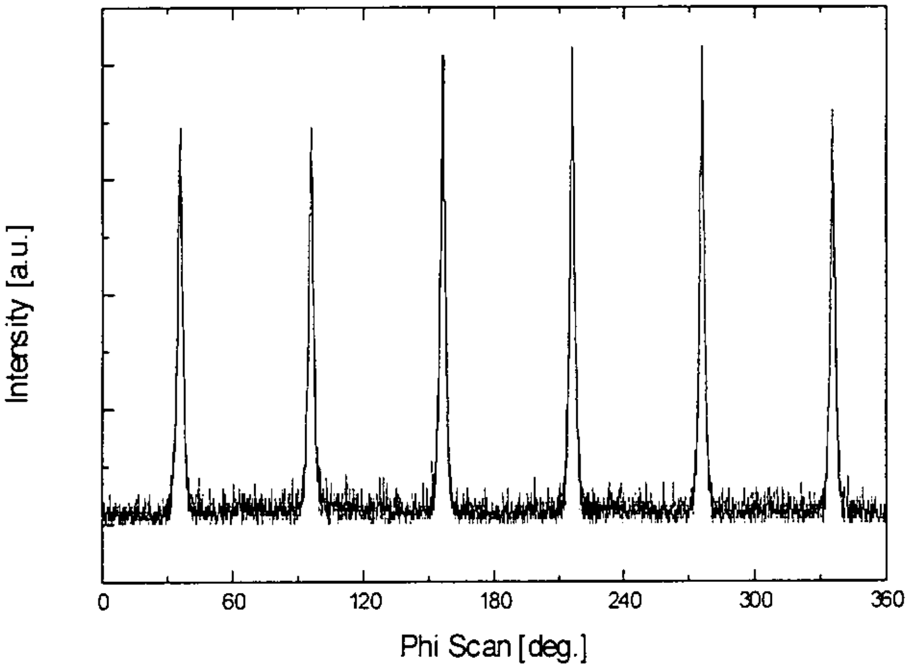

Figure 2.21 The ϕ *scan* XRD pattern of the GaN/AlN/Si(111) thin film sample when the sample is tilted at 61.9°.

In this sample, It was found that both of the cubic phase and hexagonal phase coexisted. By using the method Tsuchiya et al. reported [27], the ratio of the integrated X-rays diffraction intensities of the cubic (002) and the hexagonal $(10\bar{1}1)$ give the zinc blende structure to wurtzite structure in the sample. From the experimental data, we found that the percentage of cubic phase in the GaN/AlN/Si(111) is 2 % and the hexagonal phase is 98 %.

2.3.3.4 GaN with AlN buffer layer on Si (100)

The results are quite similar to the AlN/Si(111) as well as GaN/Si(111) samples. Figure 2.22 shows a XRD pattern of the GaN/AlN/Si(100) thin film sample, the peak at

34.737° may correspond to either the cubic (111) plane or the hexagonal (0002) plane. However, after we have done a θ-2θ scan and a ϕ scan at a tilted angle of 54.7°, we cannot observe any diffraction peak which indicates that there is no cubic phase in the sample, and we can be sure that the diffraction peak observed in the first scan corresponds to the hexagonal (0002) plane.

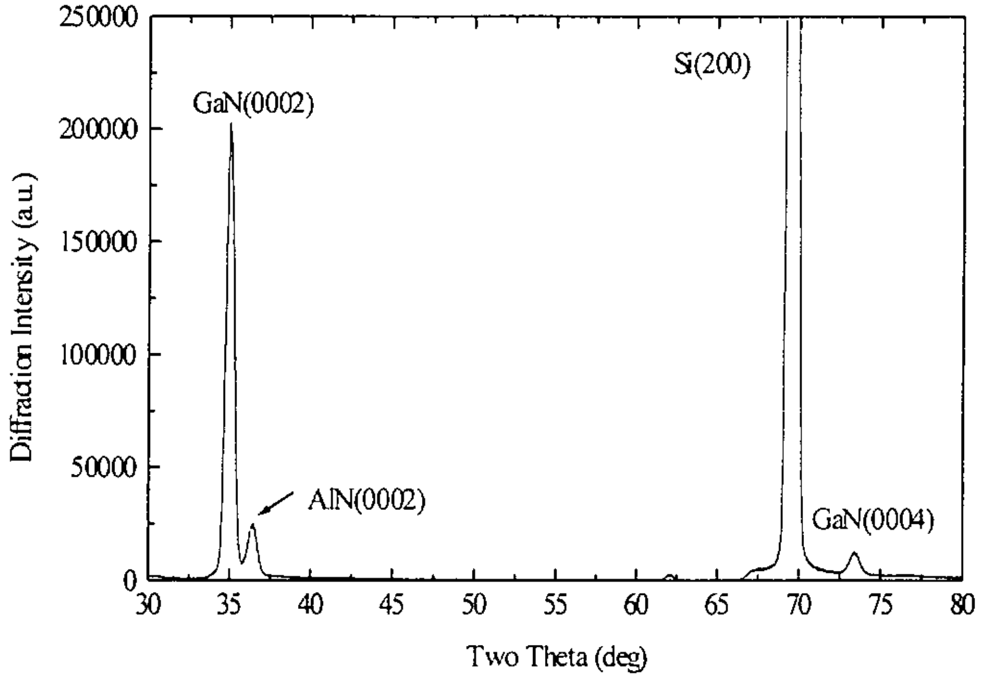

Figure 2.22 The XRD pattern of the GaN/AlN/Si(100) thin film sample.

Figure 2.23 and 2.24 show the *θ-2θ scan* and *ϕ scan* patterns of the GaN/AlN/Si(100) thin film sample (tilted at 61.9°), respectively. From Figure 2.23, we can observe a peak at 36.508° corresponding to the hexagonal plane. This shows that only the hexagonal phase existed in the sample. By using eqs. (2.3) and (2.5), as well as $2\theta_{(0002)}$ = 34.737° and 2θ = 36.508°, we can obtain the lattice constants of the GaN thin film as: a = 3.233 Å and c = 5.166 Å. From Figure 2.24, we observed that the hexagonal plane has a 12-fold symmetry.

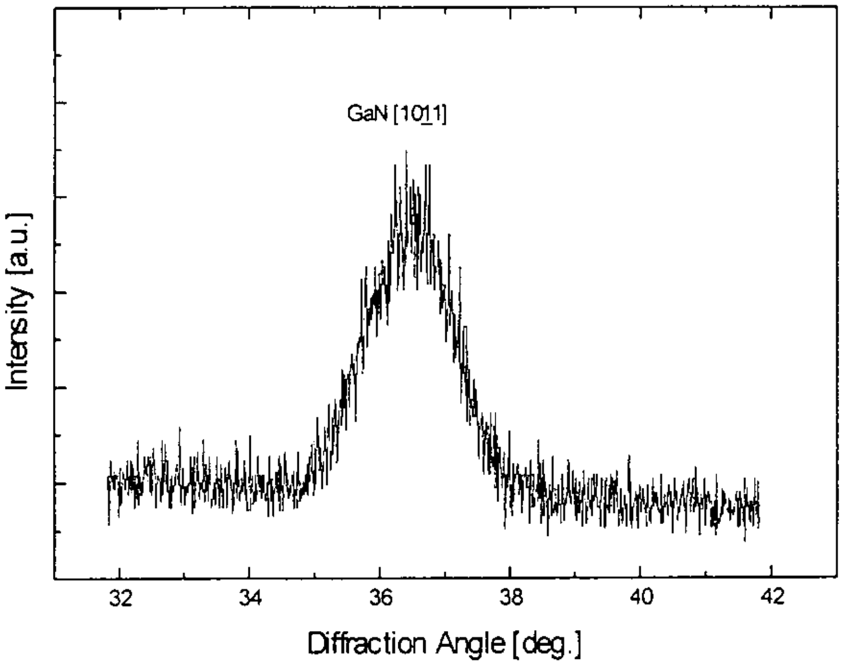

Figure 2.23 The *θ-2θ scan* XRD pattern of the GaN/AlN/Si(100) thin film sample when the sample is tilted at 61.9°.

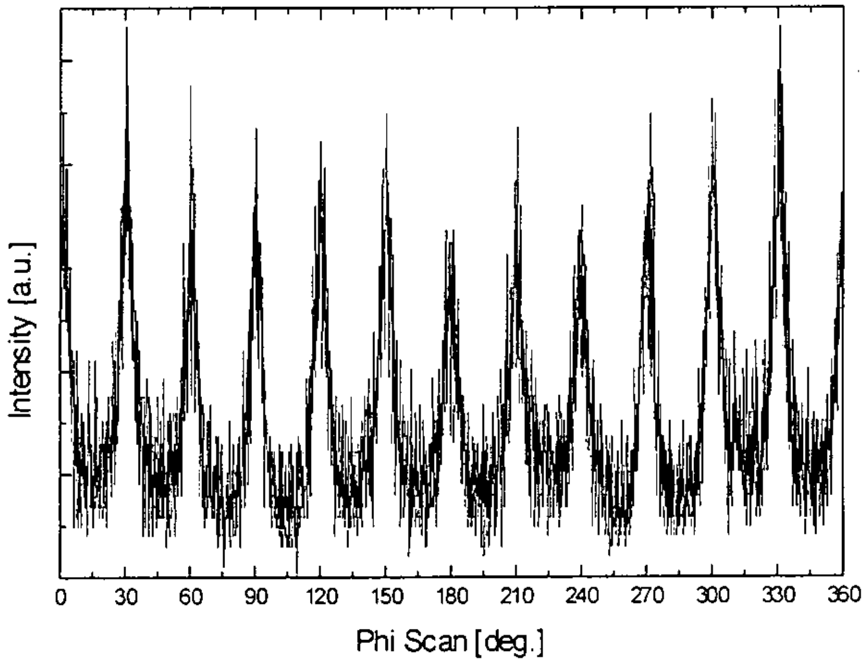

Figure 2.24 The *ϕ scan* XRD pattern of the GaN/AlN/Si(100) thin film sample when the sample is tilted at 61.9°.

2.3.4 Conclusions

Table 2.3 Summary of results obtaining from the XRD measurements.

Sample No.	*Lattice Constants (Å)*	*Phase(s) exist*
1) AlN/Si(111)	$a = 3.112$ $c = 4.970$	Only hexagonal phase
2) GaN/Si(111)	$a = 3.211$ $c = 5.177$	Only hexagonal phase
3) GaN/AlN/Si(111)	$a = 3.156$; $c = 5.168$ (hcp) $a = 4.401$ (cubic)	Hexagonal phase ≈ 98 % cubic phase ≈ 2 %
4) GaN/AlN/Si(100)	$a = 3.233$ $c = 5.166$	Only hexagonal phase

Table 2.3 shows results obtained from the XRD measurements from which the different phase(s) (cubic and/or hexagonal) existed in the samples have been identified. These are important information for identifying the piezoelectric coefficients we measured as different crystal structures have different piezoelectric coefficients. For example, cubic GaN has only one non-zero piezoelectric coefficient, d_{14} while hexagonal GaN have 3 non-zero piezoelectric coefficients, d_{31}, d_{33}, and d_{15}.

CHAPTER THREE

RESISTIVITY AND DIELECTRIC PERMITTIVITY OF AlN AND GaN

3.1 Introduction

In the previous chapter, we have described the fabrication and characterization of the samples. All the samples used in the d_{33} measurements are thin films (140nm ~ 450nm) grown on silicon substrates. Moreover, two of them were composite films (GaN/AlN/Si). To measure d_{33}, one should know the resistance, R, and capacitance, C in order to estimate the potential drop *(p.d.)* across the different layers of the sample when a voltage V is applied.

The d_{33} coefficient of a film can be calculated by the following equation:

$$d_{33} = \frac{strain}{E-field} = \frac{\frac{u}{t}}{\frac{V}{t}} = \frac{u}{V} \qquad (3.1)$$

where u is the displacement measured by an interferometer, V is the applied voltage and t is the thickness of the film. Suppose there is a multilayer sample, irrespective of whether the layer is piezoelectric or not, there is *p.d.* across each layer. In addition, if more than one of them are piezoelectric, the small displacement measured by the laser interferometer will be the sum of all the displacements induced in different layers. A more accurate equation will become:

$$u = \sum_n u_n = d_{33}(layer1)V_1 + d_{33}(layer2)V_2 + ... + d_{33}(layern)V_n \qquad (3.2)$$

where u_n is the displacement induced in layer n, d_{33} (layern) and V_n are the d_{33} and the *p.d.* across the layer n, respectively. Hence, it is important to obtain the *p.d.* if we wish to evaluate the d_{33} of a multilayer sample.

3.2 Resistivity and Dielectric Permittivity Measurements

Assuming each layer of the sample to be consisted of a R and C in parallel. The impedance, Z, across the circuit can be described as

$$Z = \frac{1}{i\omega C + \frac{1}{R}} \qquad (3.3)$$

where i is the imaginary number √-1, ω is the angular frequency, C is the capacitance and R is the resistance of the film. The total impedance can be expressed as a real part plus an imaginary part of impedance, i.e. $Z = Re\ Z + Im\ Z$. Hence eq. (3.3) can be written as:

$$\operatorname{Re} Z + \operatorname{Im} Z = \frac{\frac{1}{R} - i\omega C}{(\omega C)^2 + \left(\frac{1}{R}\right)^2} \tag{3.4}$$

and we can consider the real part and imaginary part separately. The real part and imaginary part of impedance are given below

$$\operatorname{Re} Z = \frac{\frac{1}{R}}{(\omega C)^2 + \left(\frac{1}{R}\right)^2} \tag{3.5}$$

$$\operatorname{Im} Z = \frac{-\omega C}{(\omega C)^2 + \left(\frac{1}{R}\right)^2} \tag{3.6}$$

The relaxation frequency, ω_r, can be found by differentiating *Im Z* with respect to ω and at its maximum, the differential is zero which gives:

$$\omega_r = \frac{1}{RC} \tag{3.7}$$

$$R = 2 \operatorname{Im} Z \tag{3.8}$$

The impedance (both the real and imaginary part) can be measured using the experimental setup shown in Figure 3.1. Aluminum was thermally evaporated with circular dots of diameter 1mm on the top surface of the films. The silicon substrate was attached to an IC package and the substrate and the dots act as electrodes and were wire-bonded to the legs of the package. The electrodes were connected to a Hewlett Packard HP 4194A impedance analyzer and the complex impedance was measured in the frequency range of 100 Hz to 15 MHz.

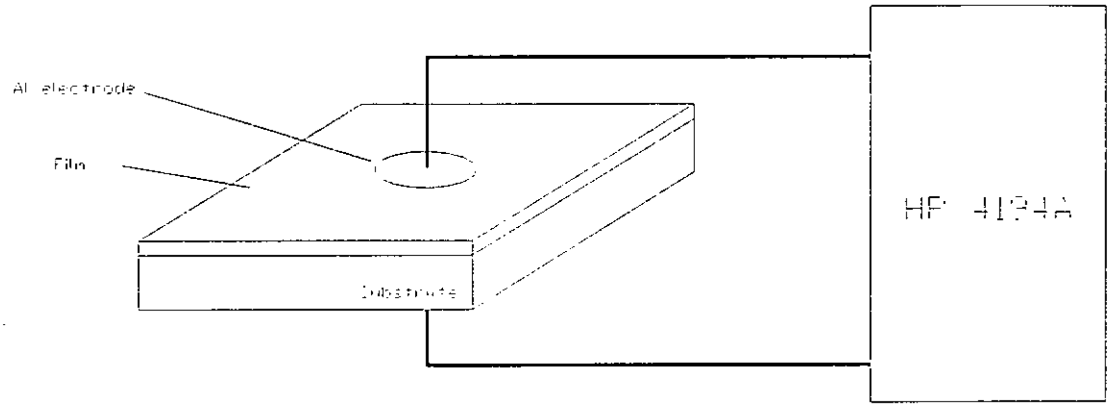

Figure 3.1 The experimental setup of measuring sample resistivity and dielectric permittivity.

Experimentally, the frequency (relaxation frequency), f_r, at which maximum *Im Z* occur is found by the impedance vs frequency scan, then eqs. (3.7) and (3.8) can be used to calculate *R* and *C* of the sample. Using these *R*, *C* values and eqs. (3.5) and (3.6), the theoretical impedance (both the real and imaginary part) vs frequency curves can be obtained. And if the theoretical impedance curves compared well with the experimental results obtained from the impedance analyzer, then one can conclude that the estimated *R* and *C* of the film are reasonable.

After obtaining the *R* and *C* of the film, the resistivity and the dielectric permittivity of the film can be calculated by using the following equations

$$\rho = R\frac{A}{t} \tag{3.9}$$

$$\varepsilon_r = \frac{Ct}{\varepsilon_o A} \tag{3.10}$$

where t is the thickness of the film, A is the area of the electrode and ε_0 is the dielectric permittivity of vacuum. This model also applies to a multilayer film. We can first estimate R and C of each single layer by using the above-mentioned procedures, then sum up all the calculated impedance of the individual layer of film by using the following equation, and then compare with the experimental result.

$$\operatorname{Re} Z = \sum_n \operatorname{Re} Z_n = \sum\nolimits_n \frac{\frac{1}{R_n}}{(\omega C_n)^2 + \left(\frac{1}{R_n}\right)^2} \tag{3.11}$$

$$\operatorname{Im} Z = \sum_n \operatorname{Im} Z_n = \sum\nolimits_n \frac{-\omega C_n}{(\omega C_n)^2 + \left(\frac{1}{R_n}\right)^2} \tag{3.12}$$

where n is the number of layers in the sample. Figure 3.2 shows the equivalent circuit of a multilayer film sample.

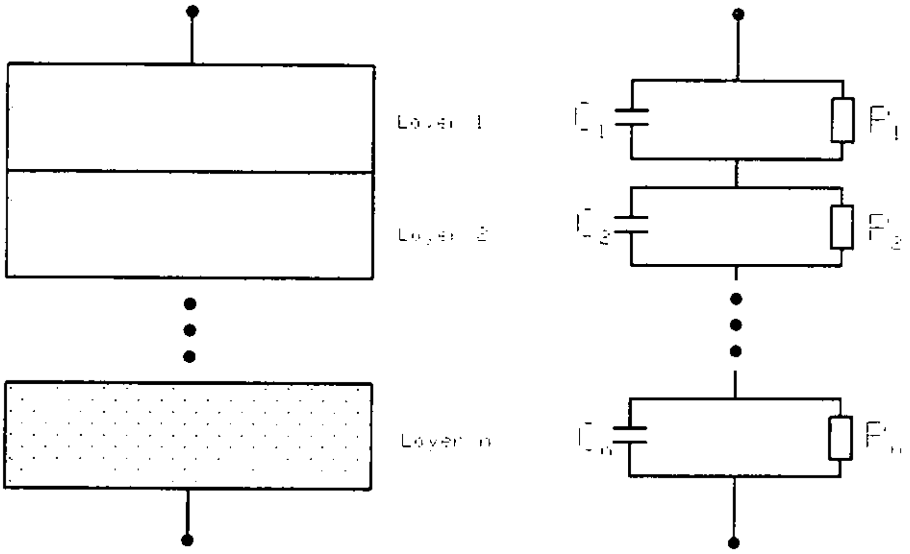

Figure 3.2 The equivalent circuit of a multilayer sample.

3.2.1 Silicon Dioxide on Silicon

In order to verify the model, a silicon wafer is considered. The surface of silicon is coated with a thin intrinsic silicon dioxide (SiO_2) layer. Aluminum was deposited on the top of the layer. Impedance can be obtained by using the setup shown in Figure 3.1. The results are shown in Figure 3.4.

In the impedance vs frequency curve, there is a maximum in the curve of *Im Z* which equals to 3 kΩ located at 15 kHz. By using eqs. (3.7) and (3.8), the estimated *R* and *C* is 6 kΩ and 1.77 nF, respectively. At high frequency, *Re Z* levels off which is equivalent to the resistance of Si (50 Ω) connect in series with the RC circuit as shown in Figure 3.3. Using eqs. (3.5) and (3.6) and the estimated values, two curves (*Re Z* and *Im Z*) were constructed. Figure 3.3 shows an equivalent circuit of SiO_2 and silicon using the estimated value. Figure 3.4 shows both the experimental and the estimated impedance of the sample.

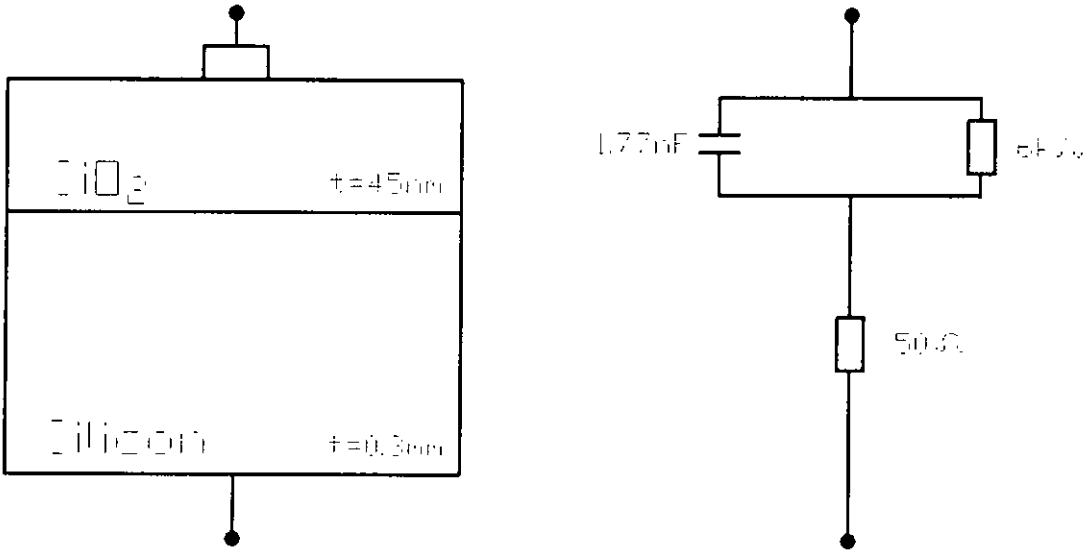

Figure 3.3 The equivalent circuit of SiO_2 and silicon. The capactiance of Si is assumed to be negligibly small.

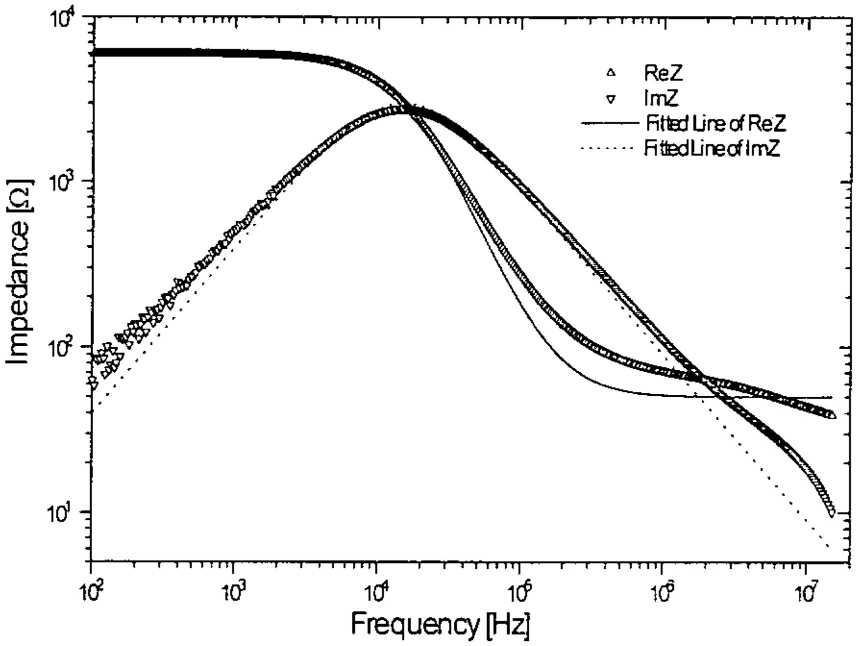

Figure 3.4 The experimental and estimated impedance of the sample.

The fitting seems to be satisfactory and the estimated value is quite appropriate. By using eqs. (3.9) and (3.10), with A = 7.85 x10^{-7} m^2 and $\varepsilon_r(SiO_2)$ = 3.75 (from literature) [28, p.12-48] the thickness and resistivity of the SiO_2 layer of the sample are found to be 45 nm and 105 kΩ-m, respectively. The board resonance peaks in all the samples are ascribed to the resonance of the equivalent RC circuits.

3.2.2 AlN Grown on Silicon (111)

In this sample, the estimated *R* and *C* is 634 kΩ and 0.13 nF, respectively. The equivalent resistance of Si is 100 Ω in series with the AlN equivalent RC circuit. The estimated impedance curves are shown in Figure 3.5.

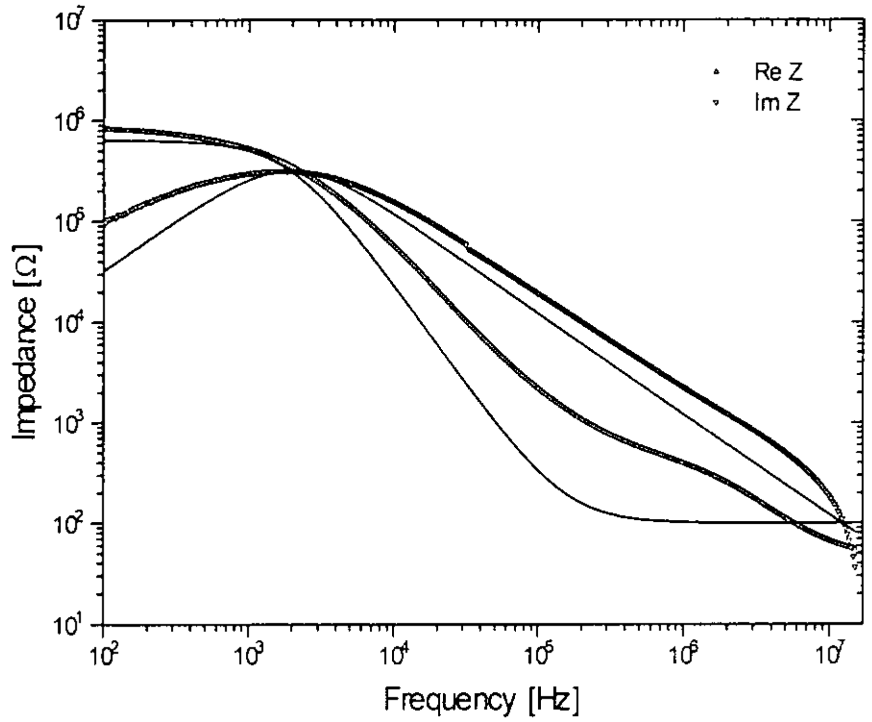

Figure 3.5 The experimental and the estimated impedance curves of the AlN/Si(111) sample.

By using eqs. (3.9) and (3.10), the estimated *R* and *C* values, $A = 7.85 \times 10^{-7}$ m^2 and the thickness of the AlN layer (450nm), the resistivity and dielectric permittivity of AlN are found to be 1.1 MΩ-m and 8.42, respectively.

The GaN/Si(111) film turns out to be quite conducting, the applied voltage cannot induce measurable displacement in this sample. This is because in the MBE process, the GaN is unintentionally doped and becomes an n-type semi-conductor.

Hence, it cannot be used in subsequent measurements and will not be discussed further.

3.2.3 GaN with AlN Buffer Layer Grown on Silicon (111)

In this sample, the estimated *R* and *C* are 218 kΩ and 0.442 nF, respectively. The equivalent resistance of Si is 300 Ω series with the GaN/AlN equivalent RC circuit. The estimated impedance curves are shown in Figure 3.6.

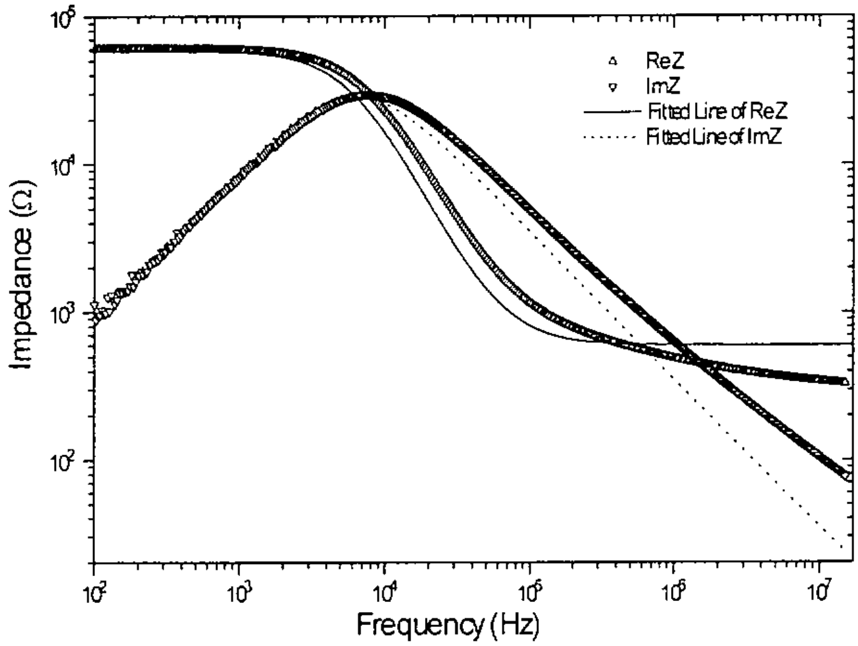

Figure 3.6 The experimental and estimated impedance curves of the GaN/AlN/Si(111) sample.

By using eqs. (3.9) and (3.10), the estimated *R* and *C* values, with $A = 7.85 \times 10^{-7}$ m^2 and the thickness of the GaN layer (140nm), the resistivity and dielectric permittivity are found to be 1.2 MΩ-m and 8.90, respectively.

3.2.4 GaN with AlN Buffer Layer Grown on Silicon (100)

In this sample, the estimated *R* and *C* are 804 kΩ and 446 pF, respectively. The equivalent resistance of Si is 400 Ω in series with the GaN/AlN RC circuit. The estimated impedance curves are shown in Figure 3.7.

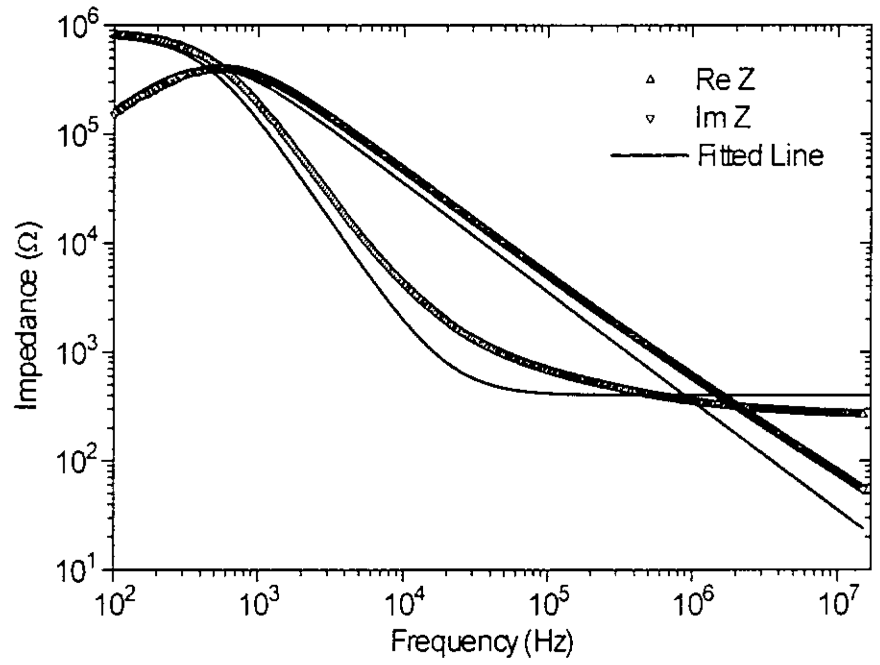

Figure 3.7 The experimental and estimated impedance curves of the GaN/AlN/Si(100) sample.

By using eqs. (3.9) and (3.10), the estimated *R* and *C* values, $A = 7.85 \times 10^{-7}$ m^2 and the thickness of the GaN layer (140nm), the resistivity and dielectric permittivity are found to be 4.5 MΩ-m and 8.99, respectively.

Table 3.1 summarizes the results obtained for the different samples

Table 3.1 The results of ρ and ε_r for different samples.

Samples	Layer	R	C [pF]	ε_r	ρ [Ω-m]	t
AlN on	AlN	634 kΩ	130	8.42	1.1 M	450 nm
Si(111)	Si	100 Ω	0	3.7	0.26	0.3 mm
GaN/AlN	GaN	218 kΩ	442	8.9	1.2 M	140 nm
On Si(111)	Si	300 Ω	0	3.7	0.785	0.3 mm
GaN/AlN	GaN	804 kΩ	446	8.99	4.5 M	140 nm
On Si(100)	Si	400 Ω	0	3.7	1.05	0.3 mm

3.3 Potential Drop Across Each Layer of the Samples

All samples used in the d_{33} measurements were thin films grown on silicon substrates. In the d_{33} measurement, the electric field was applied across the film surface and the substrate. To measure the piezoelectric coefficient, it is necessary to know the potential drop across the film and the substrate. For the two composite films, GaN/AlN/Si(111) and GaN/AlN/Si(100) in which the GaN thin film was grown on an AlN buffer layer, since AlN is also piezoelectric, the potential drop across the AlN and GaN layers is very important for the calculation of the d_{33} of GaN. In order to calculate the potential drop across each layer in the multilayer samples, certain parameters should be known, e.g. the resistance R and capacitance C of each layer of the sample. In section 3.1, we have described how to measure the R and C by using an impedance analyzer and by using the measured R and C values, we can calculate the potential drop across the layers.

It is assumed that the single layer film sample can be modeled as a resistance *R* and a capacitance *C* in parallel and the multilayer film can be represented by a number of these circuits (*R* and *C* in parallel) connected in series. Hence, for a three-layered case, an equivalent circuit can be drawn as shown in Figure 3.8.

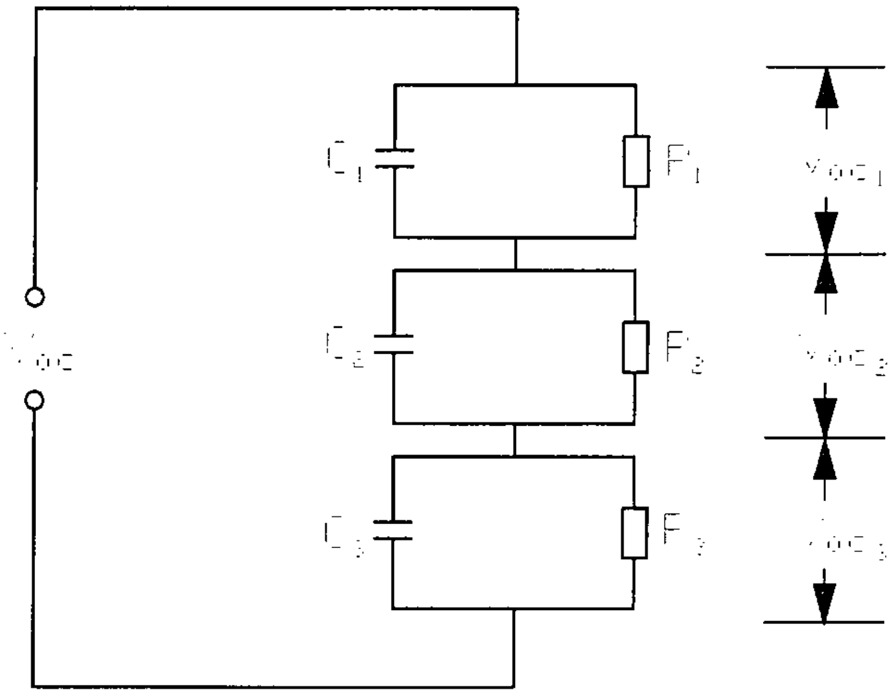

Figure 3.8 An equivalent circuit of a three-layer film sample.

$$\frac{Vac_n}{Vac} = \frac{Z_n}{\sum_n Z_n} \tag{3.13}$$

The potential drop across each layer can be calculated as a potential divider given in eq. (3.13) where Vac is the voltage supplied across the sample and Vac_n is the potential drop across layer *n*. Z_n is the impedance of layer *n*, and can be described by eq.

(3.1). The impedance depends on the frequency. A program (Appendix I) was written to solve the above equation in order to obtain the potential drop as a function of frequency across each layer.

3.3.1 Calculation Results

3.3.1.1 AlN grown on Si(111)

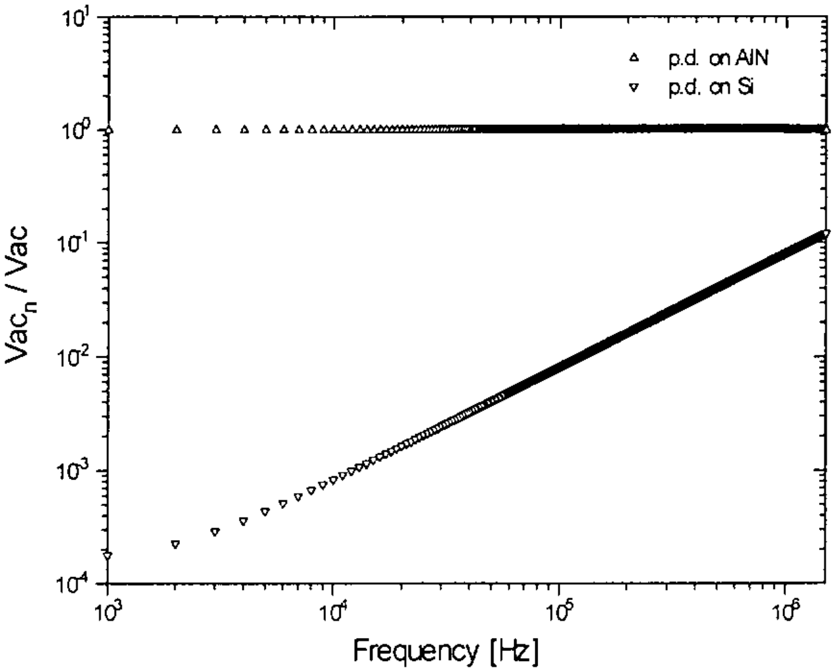

Figure 3.9 The potential drop across different layers against frequency on AlN/Si(111) sample.

Figure 3.9 – 3.11 show that the potential drops across the Si substrate are neligible small for the frequency below 10 kHz. In the GaN/AlN/Si composite films, the voltage drop across AlN is ~18% of the applied voltage.

3.3.1.2 GaN with AlN buffer layer grown Si(111)

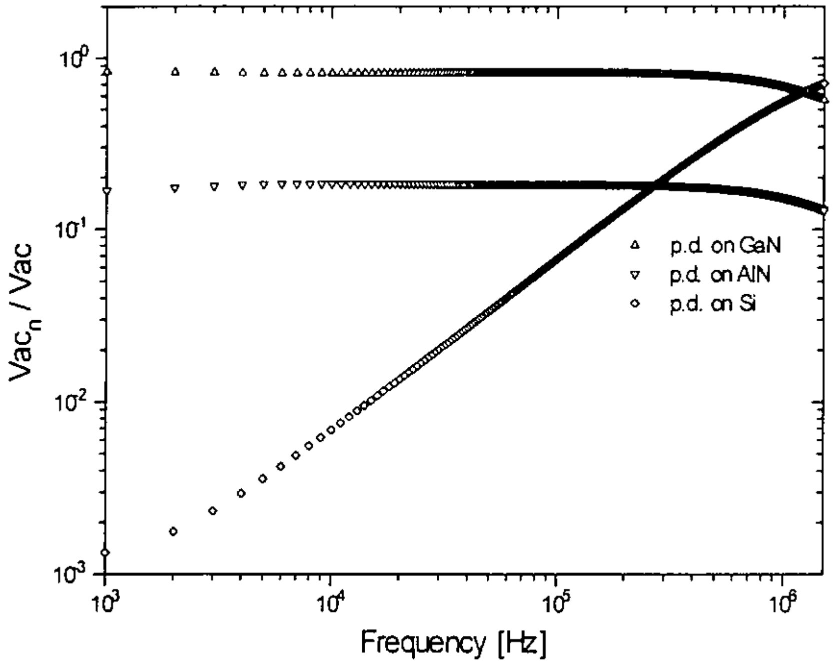

Figure 3.10 The potential drop across different layers vs frequency for the GaN/AlN/Si(111) sample.

3.3.1.3 GaN with AlN buffer layer grown on Si(100)

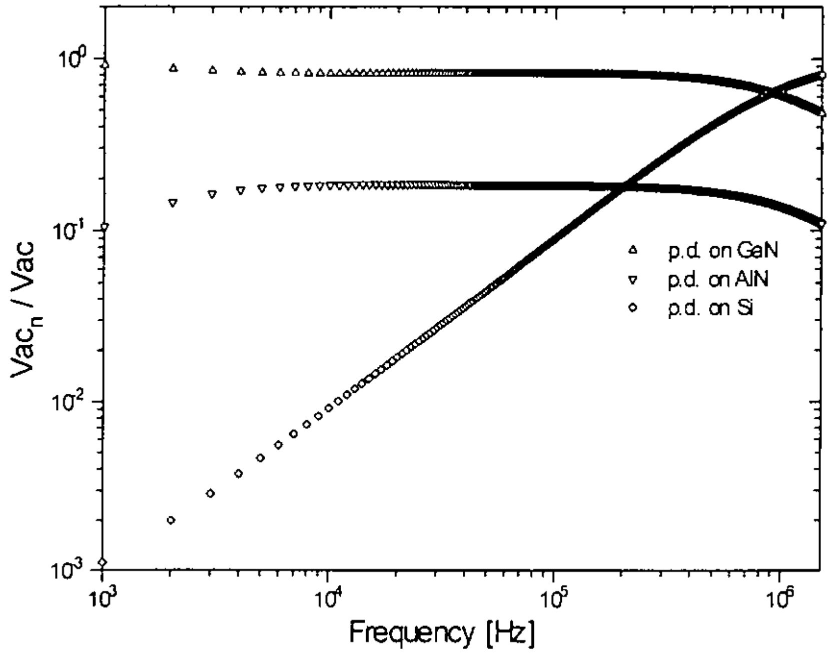

Figure 3.11 The potential drop across different layers vs frequency for the GaN/AlN/Si(100) sample.

CHAPTER FOUR

MEASUREMENT OF PIEZOELECTRIC COEFFICIENTS BY OPTICAL INTERFEROMETRY

4.1 Introduction

The piezoelectric coefficient, d_{33}, can be evaluated through the direct piezoelectric effect, i.e. by measuring the electric charge induced by an applied mechanical strain. Alternatively, it can be found through the converse effect by measuring the displacements induced by an applied electric field which is the method we use in the present work. As the displacements induced by piezoelectricity of thin films are very small (< 0.1 nm), a high-resolution detection method must be used and optical interferometry provides a good technique for doing this.

Various types of laser interferometer configurations can be used to measure the displacements induced by an applied electric field. Amongst them, the Michelson interferometer [9] and the Mach-Zehnder type interferometer [29-31] are the most popular ones.

The Michelson interferometer was first introduced by Albert Michelson in 1881. A schematic diagram of the Michelson interferometer is shown in Fig. 4.1. From an extended source of light S, beam 1 is split by a beam splitter (BS) into beam

2 and beam 3. Beams 2 and 3 are reflected by mirrors M2 and M1, respectively, where their travelling directions are reversed. After passing through the BS, beam 2 and beam 3 comes together and interference occurs.

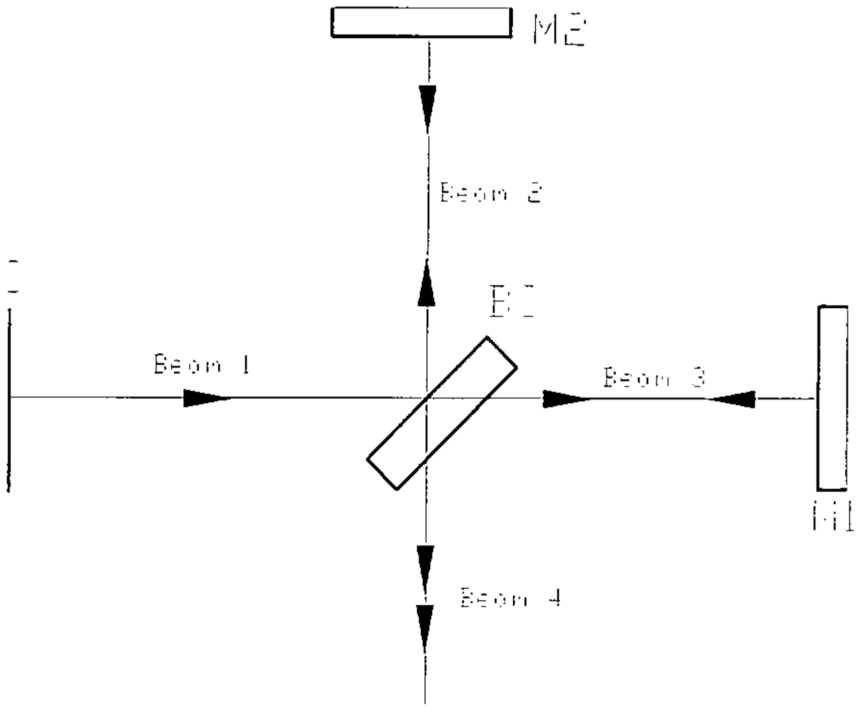

Figure 4.1 The schematic diagram of a Michelson interferometer.

In the present work, the experimental arrangement is a Mach-Zehnder type interferometer, which is different from a Michelson interferometer in that it uses heterodyne detection. An optoacoustic modulator is used to upshift the frequency of the probe beam after the BS and more details about the setup we use will be given in the next section. One of the surfaces of the sample is used to reflect the laser beam, while the opposite surface is clamped. This setup is a single beam interferometer where the laser is phase modulated by only one surface of the sample. This is different from a double beam laser interferometer arrangement where the laser is phase modulated by both of the sample surfaces. The double beam arrangement can measure the displacements induced on the surface of the sample accurately even when the sample has a bending mode vibration [32]. Nevertheless, single beam interferometer has been used successfully in determining piezoelectric coefficients [13, 29, 33, 34] of various materials.

The main objective of the present work is to use a single beam Mach-Zehnder type heterodyne interferometer to determine the piezoelectric coefficient d_{33}, of III-V nitrdes , namely AlN and GaN.

4.2 Setup of the Interferometer

Figure 4.2 shows the schematic diagram of the Mach-Zehnder type heterodyne interferometer (SH-120 from B. M. Industries, France) used to measure the displacement. A linearly polarized laser beam, L (frequency f_L; wave number $k=2\pi/\lambda$, $\lambda = 632.8\ nm$ for a He-Ne laser) is split into a reference beam, R, and a probe beam, P, by a beam splitter (BS). R propagates through a Dove prism and a polarizing beam splitter (PBS) into a photodiode. The frequency of P is upshifted by a frequency f_B (70 MHz) in a Bragg cell, and then this beam (now labeled S), is phase modulated by the surface displacement of the film sample, $x = u\cos(2\pi f_u t)$, where f_u is the vibration frequency and u is the displacement amplitude. For small u, only the sideband at $f_B + f_u$ is detected and its amplitude is

$$J_1(4\pi u/\lambda)/J_o(4\pi u/\lambda) \sim 2\pi u/\lambda = u/1007 \qquad (4.1)$$

where J_0 and J_1 are the Bessel function of the zeroth and the first order, respectively. The ratio of amplitudes of the zeroth order (centreband) to the first order (sideband) of the Bessel function gives the absolute displacement of the sample surface. The ratio, $R' = J_1(4\pi u/\lambda)/J_0(4\pi u/\lambda)$ in dBm can be measured using a spectrum analyzer (HP3589). Let $R=10^{R'/20}$, the vibration displacement is [31]

$$u=1007*R' \tag{4.2}$$

The voltage applied to the sample was measured using an oscilloscope with a 50 Ω termination connected across the sample, as the change in sample impedance with frequency will cause reflection and the 50 Ω termination will block the electrical feedback into the generator and prevent damage to the generator .

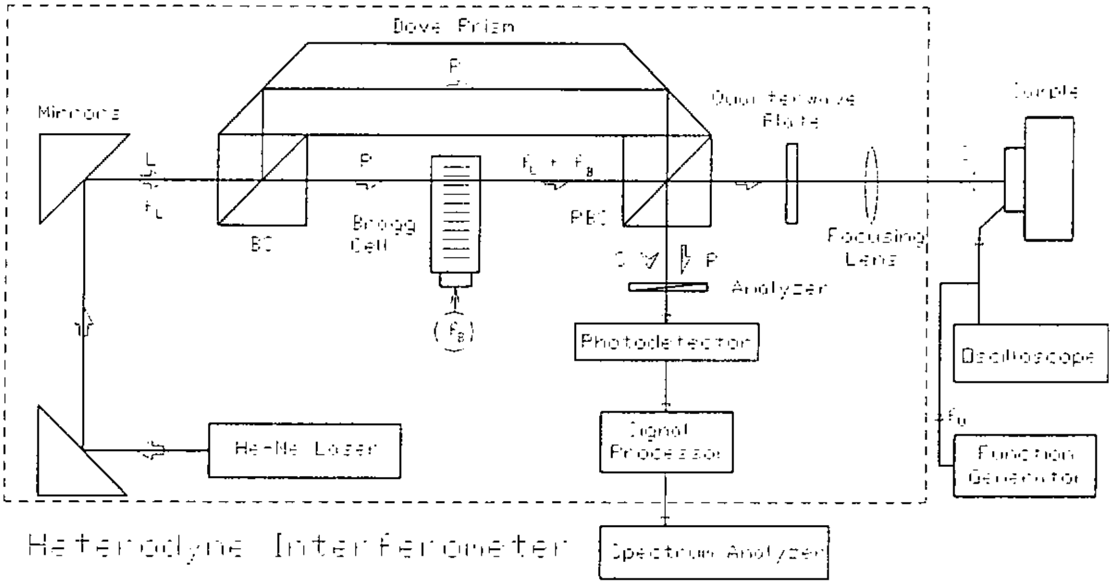

Figure 4.2 A Mach-Zehnder type heterodyne interferometer.

4.3 Theory of Operation

4.3.1 Principle of Detection

The complex amplitudes of a laser beam of frequency f_L can be written as:

$$L = e^{i2\pi f_L t} \qquad (4.3)$$

The beam is divided in the beam splitter (BS) into a reference beam and a signal (or probe) beam. The complex amplitude of the reference beam is:

$$R = e^{i2\pi f_L t} \qquad (4.4)$$

And it does not experience any perturbation.

The frequency of the signal beam was upshifted by a Bragg cell. After reflected by the surface of the sample, the phase of the beam is modulated by the displacement of the sample:

$$\phi(t) = \frac{4\pi}{\lambda} u(t) \qquad (4.5)$$

Where λ is the wavelength of the laser beam and *u(t)* is the surface displacement of the sample. Thus, the complex amplitude of the signal beam is:

$$S = s\, e^{i2\pi f_L t + i2\pi f_B t + i\phi(t)} \qquad (4.6)$$

The interference of the two beams in the photodectector delivers an electrical signal at frequency f_B, phase modulated by the displacement of the sample surface:

$$I(t) = I_0 + i(t) \qquad (4.7)$$

$$i(t) = k\cos(2\pi f_B t + \phi(t)) \qquad (4.8)$$

where k is an arbitrary constant. Half of the current *i(t)* is filtered at the frequency f_B, and phase shifted by 90°. It is then mixed with the other half which has no perturbation to yield a current:

$$
\begin{aligned}
j(t) &= \cos(2\pi f_B t + \phi(t)) \bullet \cos(2\pi f_B t + \frac{\pi}{2}) \\
&= \frac{1}{2}\cos(4\pi f_B t + \phi(t) + \frac{\pi}{2}) \bullet \cos(\phi(t) + \frac{\pi}{2}) \qquad (4.9)
\end{aligned}
$$

The signal at frequency $2f_B$ is filtered by a low pass filter, so,

$$s(t) \equiv \sin\phi(t) \qquad (4.10)$$

If the displacement is small compared with the optical wavelength, the signal can be expressed as:

$$s(t) = k\frac{4\pi}{\lambda}u(t) \qquad (4.11)$$

The final electrical signal is therefore directly proportional to the displacement of the sample surface.

4.3.2 Calibration

For a sinusoidal displacement, the complex amplitudes of the reference (*R*) and signal (*S*) beams are:

$$R = e^{i\omega_L t} \qquad (4.12)$$

$$S = s\, e^{i\omega_L t + i\omega_B t + i(4\pi u \sin\omega_0 t/\lambda)} \qquad (4.13)$$

where ω_L, ω_B and ω_o are the angular frequencies of the laser, Bragg cell and sample surface vibration, respectively. The relevant term in the detection signal is:

$$i(t) \equiv \cos(\omega_B t + \frac{4\pi}{\lambda} u \sin \omega_o t) \tag{4.14}$$

which can be expanded into a Bessel function:

$$i(t) \equiv \mathrm{Re}[e^{i\omega_B t}(J_o(\frac{4\pi u}{\lambda}) + 2iJ_1(\frac{4\pi u}{\lambda})\sin \omega_o t + 2J_2(\frac{4\pi u}{\lambda})\sin 2\omega_o t + \ldots)] \tag{4.15}$$

Figure 4.3 shows the signal *i(t)* in the frequency domain.

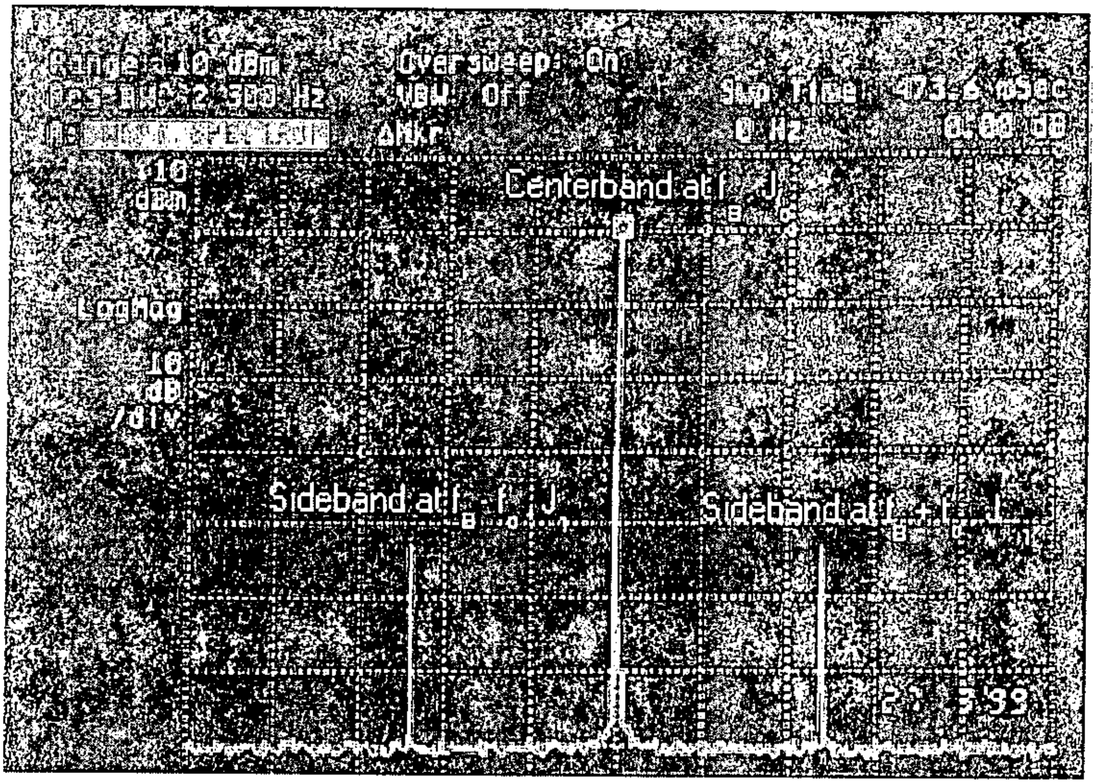

Figure 4.3 Frequency spectrum recorded by a spectrum analyzer.

The absolute value of the displacement amplitude is obtained by comparing the components at frequencies ω_B and $\omega_B + \omega_o$. If u is small compared to λ, then it becomes:

$$\frac{J_1\left(\frac{4\pi u}{\lambda}\right)}{J_0\left(\frac{4\pi u}{\lambda}\right)} \cong \frac{2\pi u}{\lambda} \qquad (4.16)$$

Table 4.1 shows the absolute amplitudes of displacement for several relative amplitudes of the two components (J_0 and J_1):

J_0 / J_1 (dB)	u (Å)
20	100
40	10
60	1
80	0.1

Table 4.1 The absolute amplitudes of displacement.

4.3.3 Direction of Displacement

The relation between the sign of the voltage and the direction of displacement depends mainly on the signal processing module. A positive voltage corresponds to the sample moving towards the optical probe. Depending on the bandwidth of detection, the sensitivity of the interferometer is (= 10^{-4} A /(Hz)$^{1/2}$) and hence can be used to detect small displacements.

4.4 Initial System Checking

The interferometer performance was checked by using a sample with known piezoelectric coefficient, d_{33}. In this work, a lithium niobate ($LiNbO_3$) crystal was used.

The Z-cut lithium niobate plate with dimensions of 14.8 mm X 7.2 mm X 0.8 mm was attached on an aluminum block using silver paint. The experimental setup is shown in Figure 4.4. The d_{33} coefficient was measured as a function of frequency from 5 kHz to 1.4 MHz.

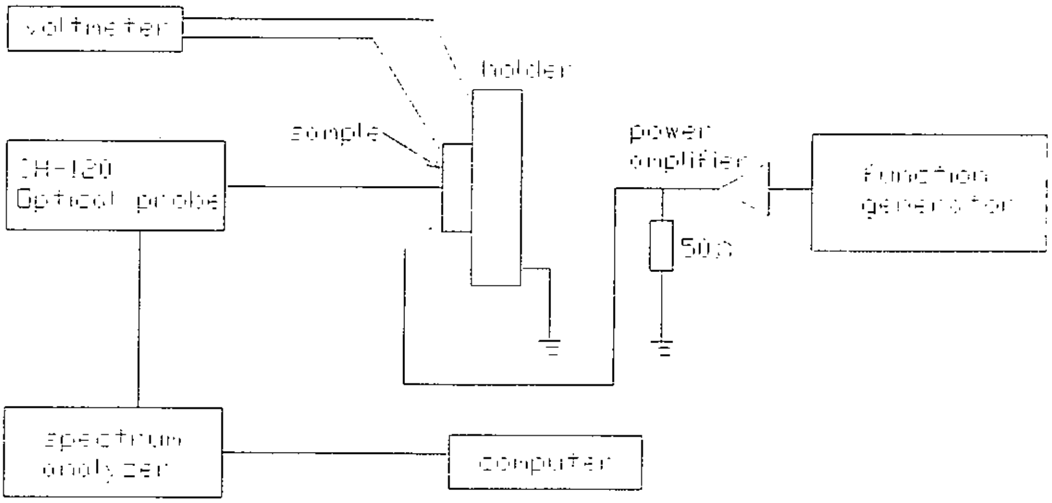

Figure 4.4 Expermental Setup.

Figure 4.5 shows the variation of the displacement with driving voltage at 10 kHz. From the slope of the fitted line, the d_{33} coefficients of the $LiNbO_3$ is found to be 9.613 pmV^{-1}. The correlation coefficient of the best-fit straight lines is 0.9994. The value found by using the single beam Mach Zehnder type heterodyne laser interferometer agreed well with the reported value (= 9.55 pmV^{-1}) in ref. [13, 31].

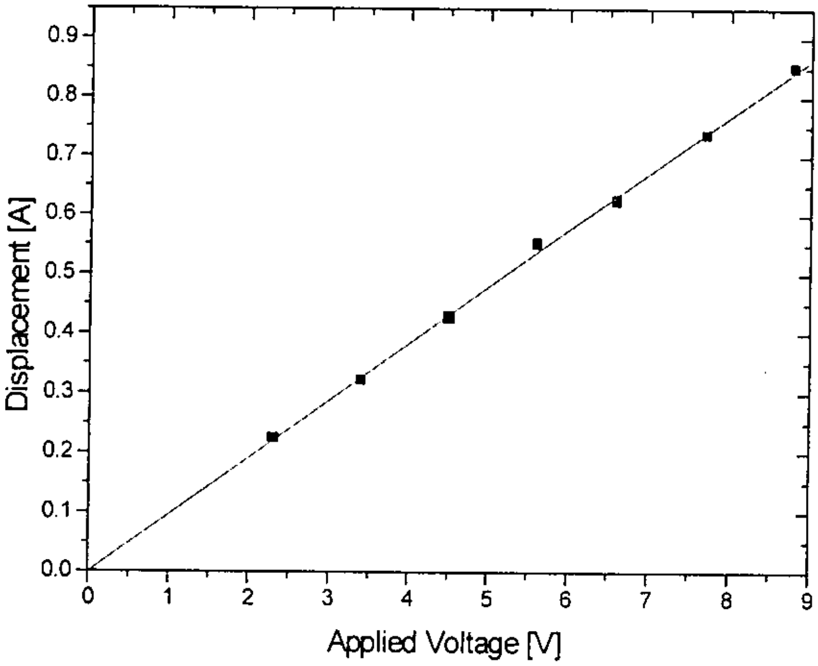

Figure 4.5 Variation of displacement with driving voltage at 10 kHz for the $LiNbO_3$ sample.

Figure 4.6 shows the variation of the measured d_{33} with frequency. It is seen that the value is approximately constant over the full range except at frequencies higher than 200 kHz, where resonance of the crystal occur.

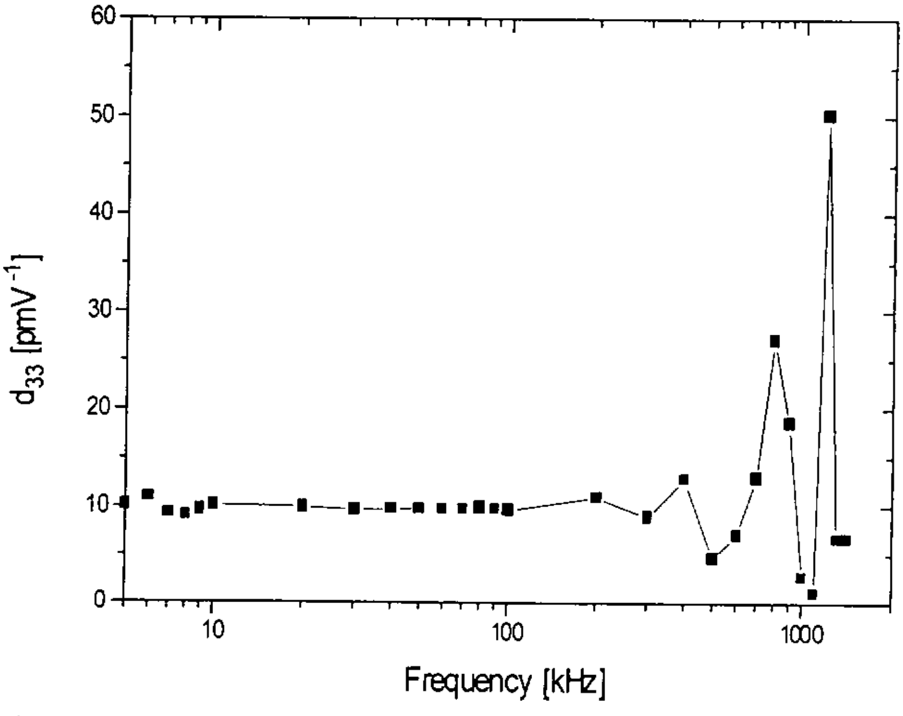

Figure 4.6 Variation of d_{33} with frequency for the $LiNbO_3$ sample.

4.5 Conclusion

The interferometric technique has high sensitivity (= 10^{-4} A /(Hz)$^{1/2}$) and will be useful for measuring piezoelectric coefficients, especially when the *d*-coefficients of the measured materials are small (e.g. less than 10 pmV^{-1}). In our work, the performance of the single beam Mach Zehnder type heterodyne laser interferometer was checked by using a lithium niobate ($LiNbO_3$) sample. In the calibration testing, it was found that the interferometer could achieve an accuracy of ± 2 % for a *d*-coefficient at the order of 10 pmV^{-1}.

CHAPTER FIVE

PIEZOELECTRIC COEFFICIENTS OF GALLIUM NITRIDE AND ALUMINUM NITRIDE

5.1 Introduction

Aluminum nitride (AlN) and gallium nitride (GaN) are III-V nitrides and the reported lattice parameters of AlN and GaN with wurtzite structure are: a = 3.11 Å, c = 4.98 Å for AlN [35] and a = 3.189 Å, c = 5.185 Å for GaN [35]. AlN and GaN have wide direct bandgaps of 6.2 [8] and 3.39 eV [36], respectively. Both of them have potential applications in devices working in high temperature and hostile environments [37]. Many different growth techniques have been used to prepare AlN and GaN films and molecular beam epitaxy (MBE) is one of the techniques that can produce high-quality epitaxial AlN and GaN films. Due to its superior properties, research in the physical properties and applications of AlN and GaN has attracted considerable interest [8]. However, to date there appears to be limited data on the piezoelectric coefficients of AlN as well as GaN. These parameters are important since both of them have potential use in microactuators, microwave, acoustic and other microelectromechanical (MEM) devices [38].

5.2 Review of Previous Work

Table 5.1 shows a summary of the piezoelectric strain coefficients, *d*, as reported in the literatures for AlN. Table 5.2 shows the theoretical piezoelectric stress coefficients, *e*, for both of AlN and GaN.

Reference	d_{31}	d_{33}	d_{15}	Method
Hutson (1963)	-2	5	4	without mention
Tsubouchi et al. (1981)	-2.65	5.53	-4.08	SAW velocity measurements
Kamiya (1996)	-2.71	6.72	-----	Hartree-Fock periodic approach
Ian Guy's (1998)	-2.6	5.1	-3.6	Laser interferometry

Table 5.1 summary of *d* coefficients (units are pmV^{-1}) for AlN.

	e_{31}	E_{33}	Theory / Group
AlN	-0.60	1.46	Berry-Phase Approach
GaN	-0.49	0.73	Berry-Phase Approach

Table 5.2 values of *e* coefficients (units are Cm^{-2}) for AlN and GaN [39].

5.3 Crystal Structures and the Piezoelectric Coefficients

The crystal structure of the nitride films are strongly influenced by the substrate material and its orientation. The equilibrium crystal structure for the III-V nitrides is the wurtzite structure. However, cubic (zinc-blende) GaN can be grown on (001) GaAs [40, 41], on cubic SiC [42], and on Si (100) [43]. All GaN grown on either Si (111) [19, 44] or GaAs (111) [19, 45] are reported to have wurtzite structure.

In principle, the wurtzite structure is similar to the zinc-blende structure. The crystal structures differ only in their stacking order. The stacking order of wurtzite structure has an ABABAB... sequence while the zinc-blende has an ABCABC... sequence (Fig. 5.1). The two crystal structures have nearly the same nearest-neighbor spacings which explains why the observed physical properties of the wurtzite and zinc-blende GaN are very similar [46].

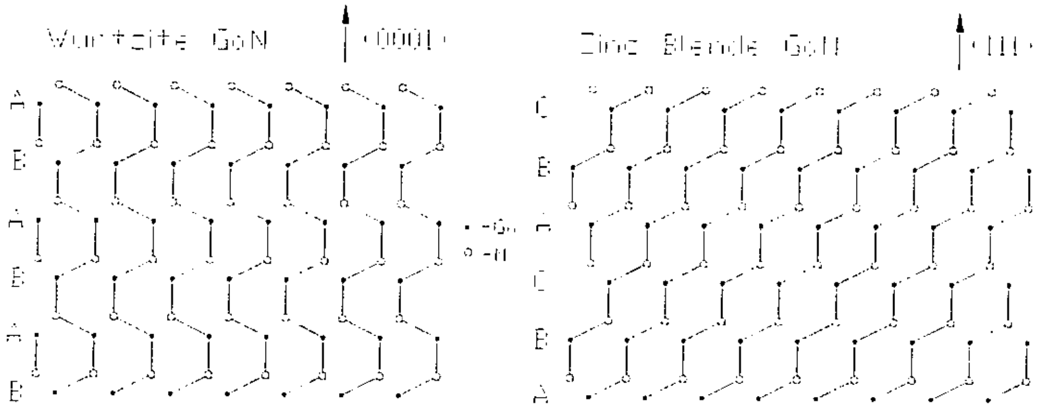

Figure 5.1 Crystal structures of the two common nitride polymorphs.

The wurtzite crystal structure has a hexagonal 6mm symmetry with four atoms in one unit cell. The piezoelectric matrix of 6mm symmetry has three independent components, which is d_{31} ($= d_{32}$), d_{33} and d_{15} ($= d_{24}$) [10, p.124]. The zinc blende structure has a cubic 43m symmetry, the piezoelectric matrix has only one component, d_{14} [10, p.124].

The relation between the two structures is that there are two tetrahedra in the wurtzite lattice, and each of them can be related with the tetrahedra in the zinc-blende lattice by a simple rotation [9]. So, a close relationship of the tensors of the physical properties can be setup between the two structures. The relationships between the piezoelectric coefficients of the two structures are [47, 48]:

$$d_{14} = \sqrt{3} d_{33}'' \tag{5.1}$$

$$d_{14} = -2\sqrt{3} d_{31}'' \tag{5.2}$$

where the unprimed quantities in the above equation are related to the zinc blende structure, while the double primed quantities are related to the wurtzite structure.

From eqs. (5.1) and (5.2), the relation between d_{31}'' and d_{33}'' can be obtained.

$$d_{31}'' = -\frac{1}{2} d_{33}'' \tag{5.3}$$

5.4 Measurement of the d_{33} Coefficient

Figure 5.2 shows the wurtzite structure. In a film with wurtzite structure, the plane of the film is usually perpendicular to the *c*-axis. The subscript 3 of d_{33} is associated with the direction of the c-axis. In order to obtain the d_{33}, an electric field is applied parallel to the *c*-axis (thickness direction) and the strain induced in the *c*-axis direction is measured. Then $d_{33} = \frac{strain}{field}$ can be evaluted.

The d_{31} can be calculated by using eq. (5.3). The physical meaning of the coefficient is the changes in the lateral dimensions of the crystal with the electric field applied in the thickness direction. Since d_{33} is defined to be positive, so, d_{31} is negative.

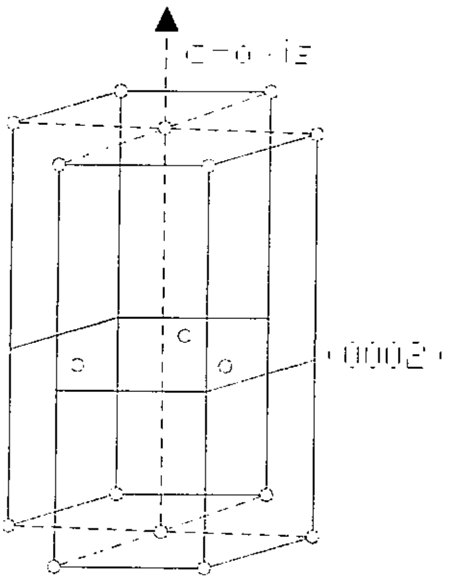

Figure 5.2 The *c*-axis of a wurtzite structure.

5.5 Experimental Details

5.5.1 Sample Geometry

In this work, several types of film samples were studied. One type is an AlN thin film (~ 450 nm thick) grown on Si (111), the other two types are composite films, with GaN thin film (~ 140 nm thick) grown on an AlN buffer layer (~ 30 nm thick) with either Si (111) or Si (100) as the substrate.

Figure 5.3 shows the schematic structure of the sample geometry of a composite film used in the interferometric measurements. The film sample has an area of about 10 mm × 10 mm. A number of aluminum spots of diameter 1 mm were thermally evaporated on the top surface of the film. Each of these spots serves as a top electrode as well as a mirror to reflect the probe beam from the interferometer. The Si substrate was glued to an aluminum block connected to ground by silver-filled epoxy that was in turn rigidly attached to a translation stage. An a. c. electric field was applied across the electrodes and the change in the film thickness was measured using a Mach-Zehnder type heterodyne interferometer.

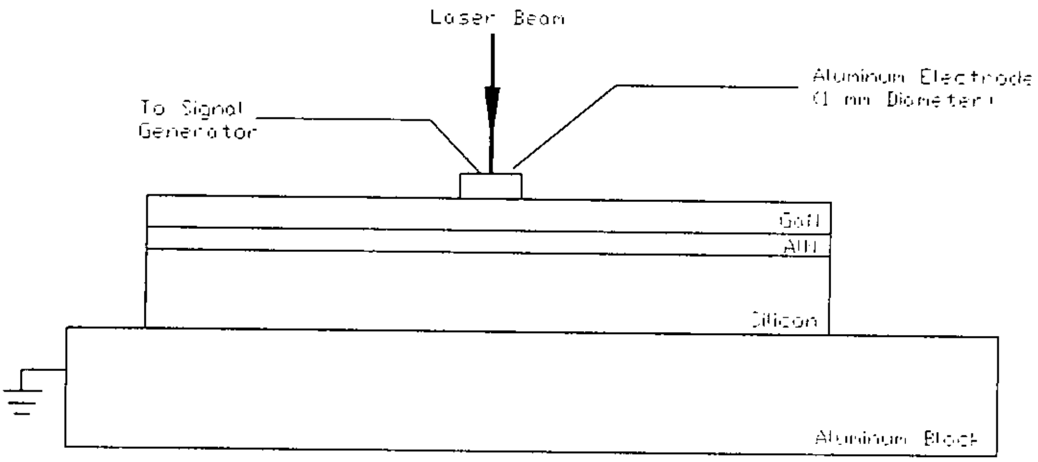

Figure 5.3 The sample geometry of a composite film.

5.5.2 Bending Effect and Sample Mounting

Using laser interferometer to measure a small displacement induced by piezoelectric properties is a simple method with high sensitivity. There is a drawback when a single beam interferometer is used. The single beam interferometer can only measure the surface displacement, which is assumed to be the displacement induced by piezoelectric sample. This assumption is only true if the back surface of the sample is rigidly mounted. However, in case of a bulk sample, the back side of the sample may deform against the bonding material applied between the sample and the holder. The deformation will get higher when bending mode occurs or when the frequency gets near to the mechanical resonance of the film [49].

In the case of thin films, it is because the piezoelectric thin films deposited by MBE are well-adhered to the substrate and the mass and thickness of the film are small compare with that of the substrate, the effect caused by thickness resonance of the film can be negligible up to a very high frequency. However, the bending of substrate as illustrated in Figure 5.4 should be considered. Suppose the field is applied in the z (or 3)-direction, it induces not only the change of film thickness *(ΔL)* in the z-direction, but also bending in the XY plane. Due to the stress in the XY plane, the substrate may change its shape as shown in Figure 5.4 [34]. Therefore, the displacement measured by a single beam interferometer *($\Delta L'$)* will include the bending mode vibration *(ΔL_b)* if the substrate is not rigidly mounted. The magnitude of ΔL_b depends on the substrate mounting and on the initial curvature of the substrate (convex or concave).

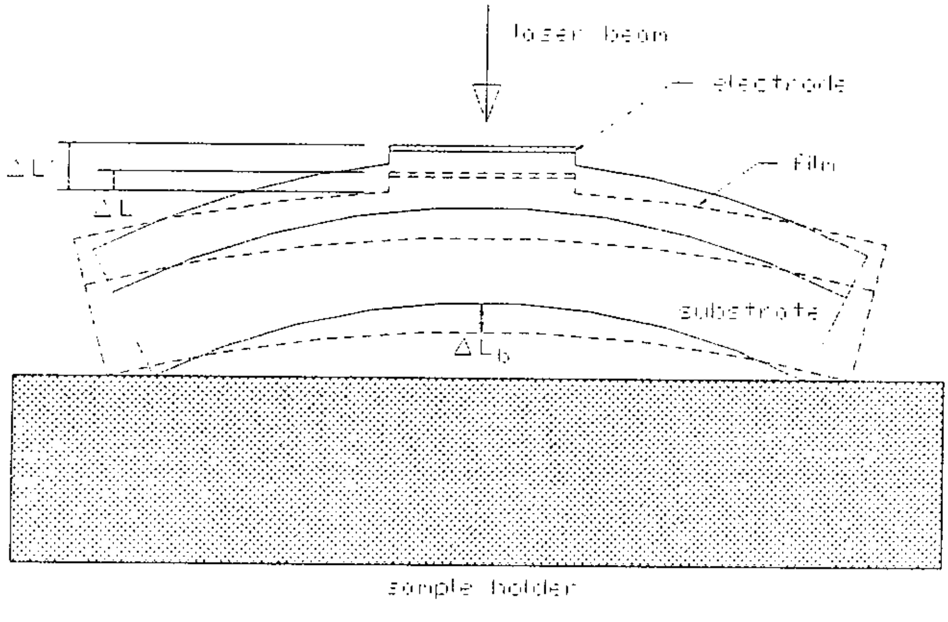

Figure 5.4 The bending mode vibration in a thin film grown on a substrate.

Kholkin [34] stated that using the equations for the static motion of a piezoelectric bimorph. One can obtain:

$$\Delta L_b = (L/2h)^2 d_{31} V \left(\frac{3kr(1+r)}{1+k^2r^4+2k(2r+3r^2+2r^3)} \right) \qquad (5.4)$$

where L is the effective length of the bimorph, when the film is partially covered with electrode, L is a function of both longitudinal sizes of the substrate and the top electrode. $r=h'/h$, *h and* h' are the thickness of the film and substrate, respectively, k is the ratio of the Young's moduli of the substrate and the film, d_{31} is the piezoelectric coefficient, and V is the driving voltage. Assume that the film is much thinner than the substrate, then the equation can be simplified to

$$\Delta L_b \approx \frac{3L^2 d_{31} V}{4kh'^2} \qquad (5.5)$$

According to eq. (5.5), we can calculate the value of the bending deflection. And also, The ratio of bending deflection to the real displacement induced by the converse piezoelectric effect can be obtained,

$$\Delta L = d_{33} V \qquad (5.6)$$

$$\left(\frac{\Delta L_b}{\Delta L} \right) \approx \left(\frac{3}{4k} \right) \left(\frac{L}{h'} \right)^2 \left(\frac{d_{31}}{d_{33}} \right) \qquad (5.7)$$

In our case, for a Si substrate covered by either an AlN or GaN thin film, the Young's moduli ratio is $k \approx 0.41$ [24, 50 p.657], the ratio of $d_{31}/d_{33} \approx -0.5$ from eq. (5.3). So, we can estimate $\Delta L_b / \Delta L$ by the following equation

$$\Delta L_b / \Delta L \approx -0.91(L/h')^2 \qquad (5.8)$$

In a common case $(L/h' \approx 10)$, then the bending contribution can be more than ninety times greater than the piezoelectric displacement of the film if the substrate is not fixed. However, these considerations are only true for low frequency quasi-static response. when frequency increases, resonance will occur and may enhance the bending mode vibration.

Consider eq. (5.8), we can see that the $\Delta L_b / \Delta L$ ratio is proportional to $(L/h')^2$. Therefore, in order to minimize the bending deflection, one can reduce L, the effective length of the bimorph (i.e. the length of the top electrode) and/or increase the substrate thickness.

When measuring the vibration displacement using an interferometer, sample mounting is crucial to ensure that only the desired thickness mode vibration is excited [9]. Other modes such as the bending mode may have a vibration amplitude may orders of magnitude larger than that of the thickness mode, hence, there is a larger error in the measurement if bending mode is also excited. One way to eliminate the bending effect is to reduce the size of the electrode and to glue the substrate to a rigid holder [34]. To ensure that no bending mode was present, the probe beam was scanned across the sample surface. As mentioned in the previous section, Al spots of diameter 1mm were deposited at different positions of the top surface for use as electrodes as well as mirrors to reflect the probe beam. Measurements of the displacement amplitudes at these different positions gave essentially the same results, indicating that no bending mode had been excited. The diameter of the probe beam, which corresponds to the spatial resolution of the measurement, was about 100 μm. As the electrode diameter was 1 mm, the probe beam was also scanned across each Al spot to test whether bending vibration was excited within the 1 mm spot. As shown in Figure 5.5, the constant vibration amplitudes observed imply that the dominant vibration is the thickness mode [9].

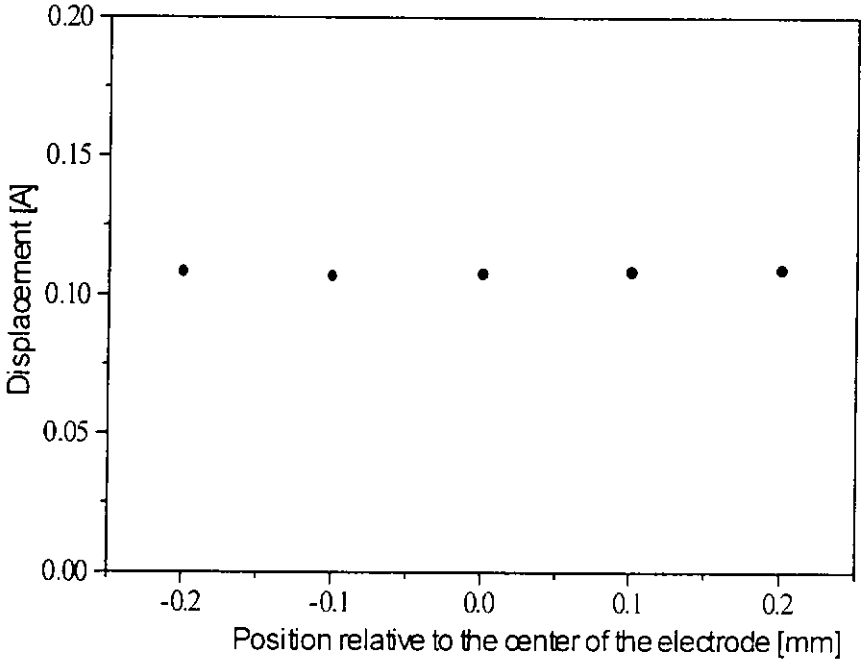

Figure 5.5 Variation of the amplitude of vibration across the surface of a 1 mm diameter Al electrode near the center of the film measured at 10 kHz.

5.6 Experimental Results

Experimental results obtained for the three samples are given in Figures 5.6 to 5.14.

5.6.1 AlN Grown on Silicon (111)

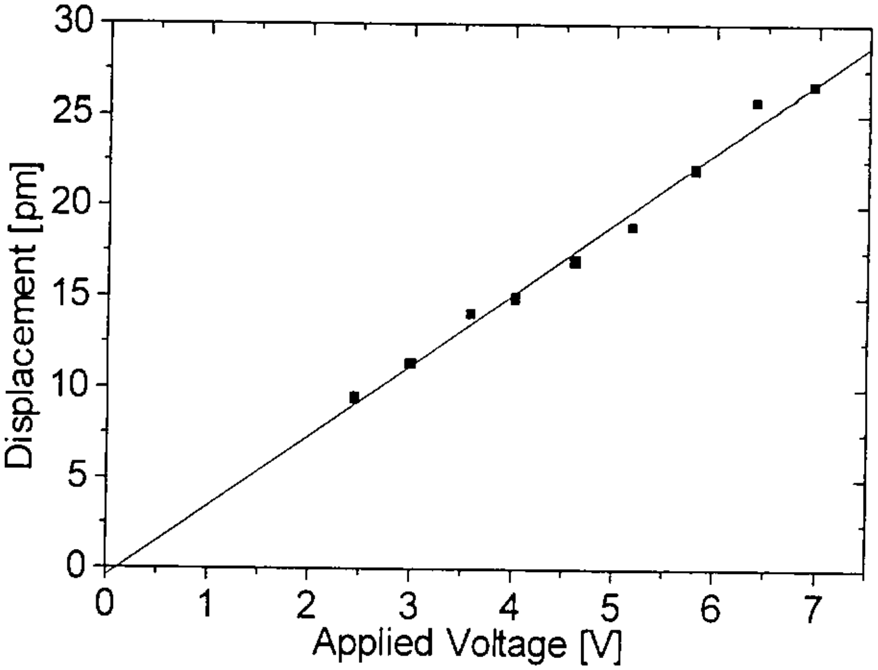

Figure 5.6 Variation of displacement with driving voltage at 10 kHz for the AlN sample.

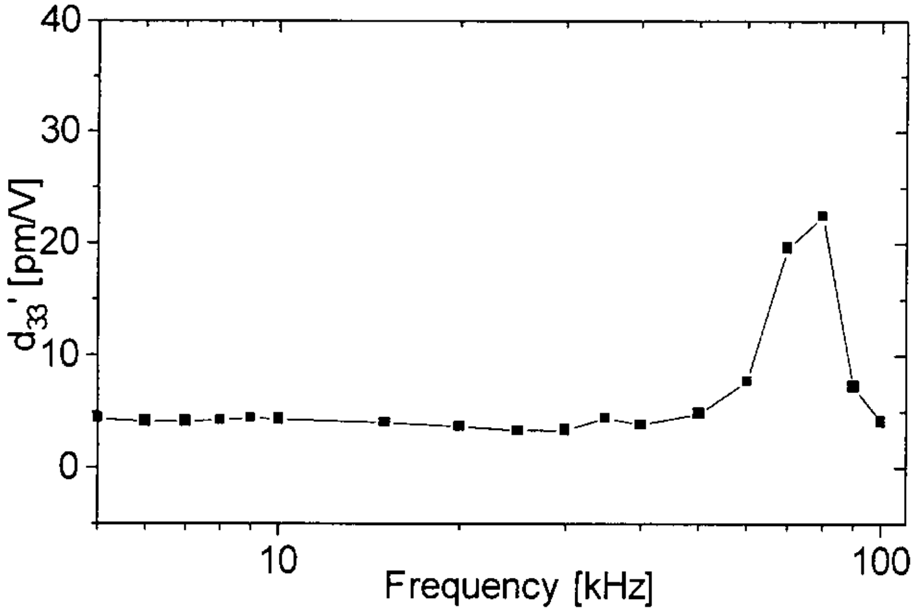

Figure 5.7 Variation of d_{33}' with frequency for the AlN sample.

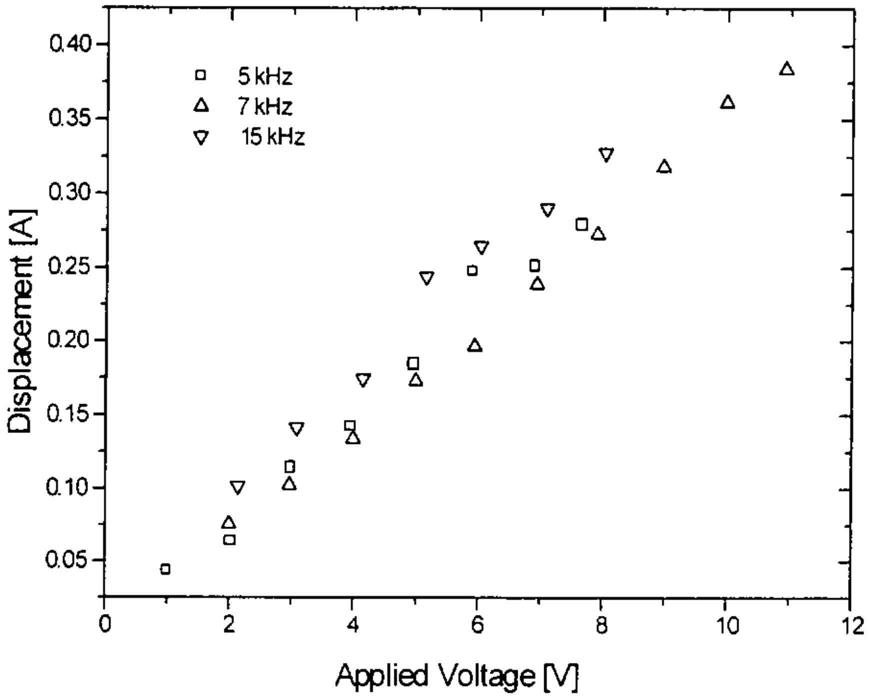

Figure 5.8 Piezoelectric response obtained with the AlN sample. Variation of mechanical displacement with driving voltage measured for the frequency in the range from 5 – 15 kHz.

From Figure 5.6, the response of the piezoelectric displacements with different driving voltages at 10 kHz is approximately linear. The correlation coefficients of the best fit straight line is 0.99475. The clamped d_{33} value (d_{33}') of the AlN grown on Si (111) can be obtained from the slope of the fitted straight line. A value of (3.90 ± 0.1) pmV^{-1} is found. The values of d_{33}' IN the frequency range of 5 – 100 kHz are shown in Figure 5.7. It is seen that the value is approximately constant over the full range except at frequency above 50 kHz where sample resonance exists.

By using eq. (5.3), the corresponding value of d_{31}' was (1.95 ± 0.1) pmV^{-1} for AlN thin film grown on Si(111).

5.6.2 GaN with AlN Buffer Layer Grown on Silicon (111)

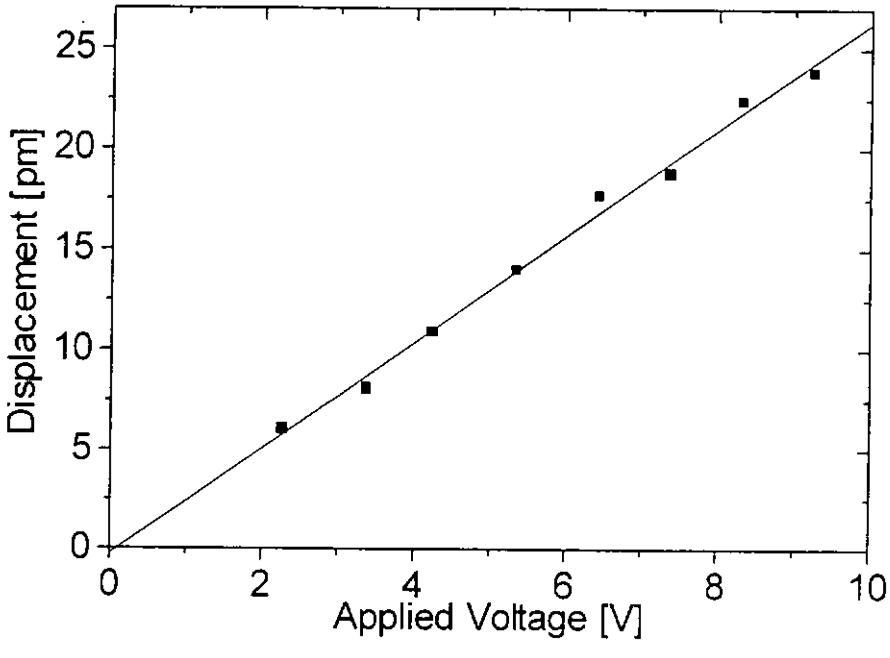

Figure 5.9 Variation of displacement with driving voltage at 10 kHz for the GaN/AlN/Si(111) composite film sample.

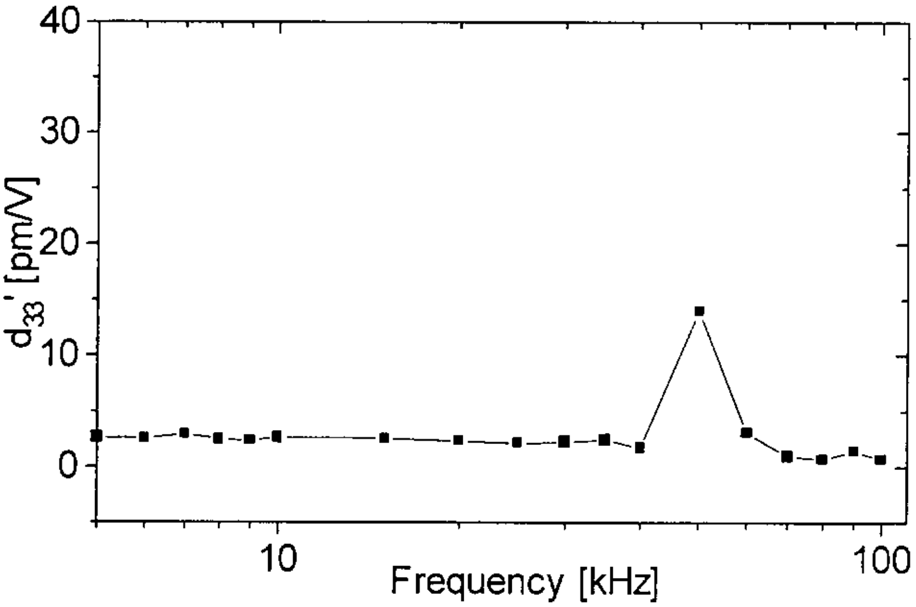

Figure 5.10 Variation of d_{33}' with frequency for the GaN/AlN/Si(111) composite film sample.

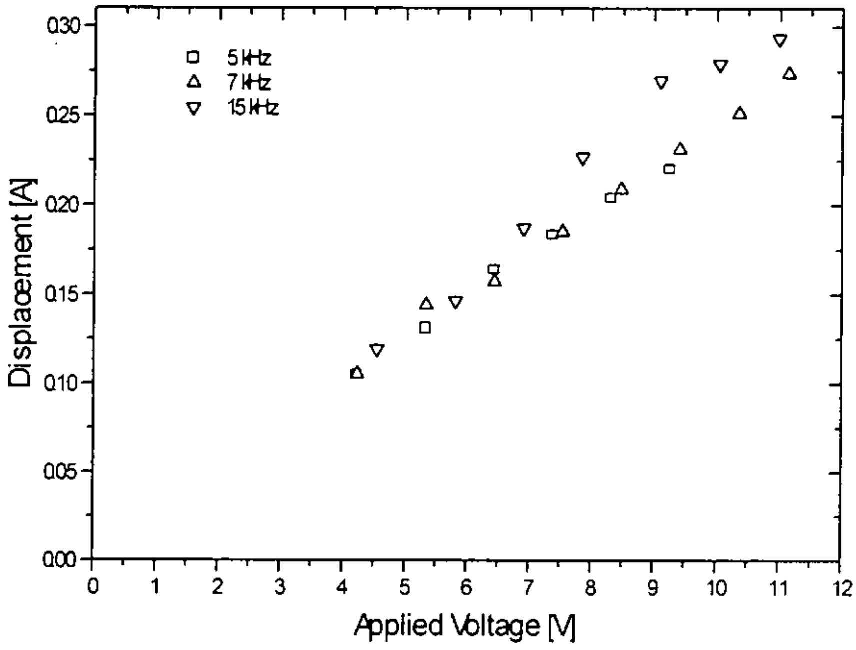

Figure 5.11 Piezoelectric response obtained with the GaN/AlN/Si(111) sample. Variation of mechanical displacement with driving voltage mesured for the frequency in the range from 5 – 15 kHz.

5.6.3 GaN with AlN Buffer Layer Grown on Silicon (100)

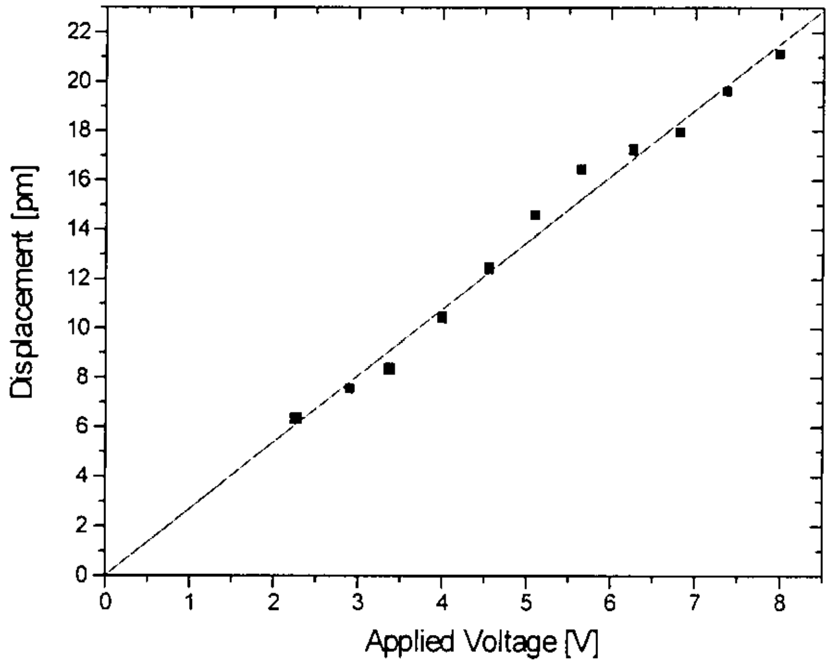

Figure 5.12 Variation of displacement with driving voltage at 10 kHz for the GaN/AlN/Si(100) composite film sample.

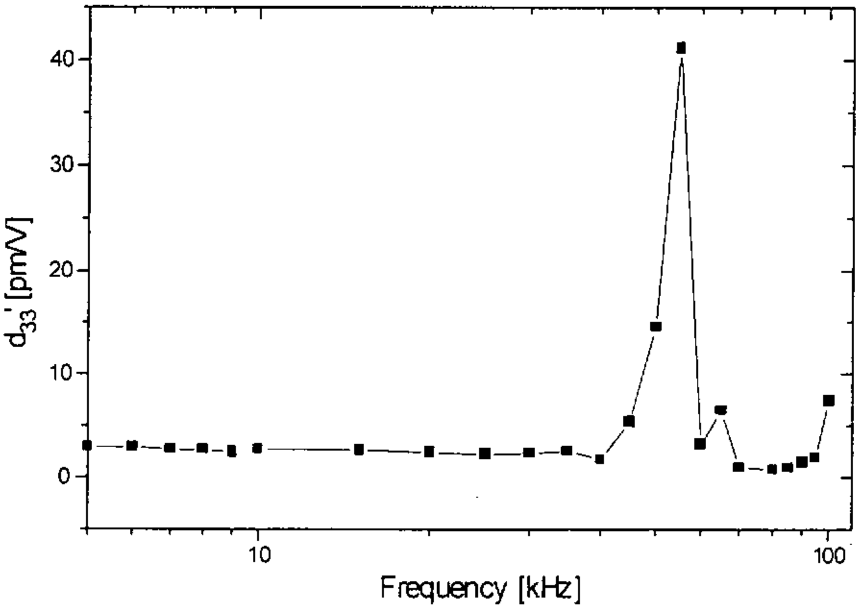

Figure 5.13 Variation of d_{33}' with frequency for the GaN/AlN/Si(100) composite film sample.

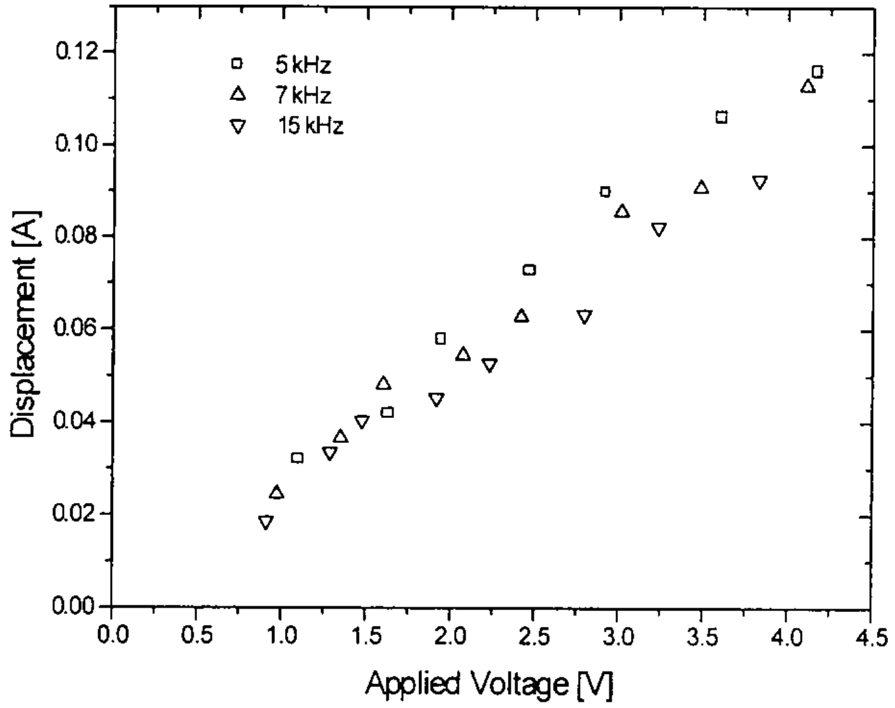

Figure 5.14 Piezoelectric response obtained with the GaN/AlN/Si(100) sample. Variation of mechanical displacement with driving voltage measured for the frequency in the range from 5 – 15 kHz.

As shown in Figure 5.9 and 5.12, the piezoelectric responses of both GaN/AlN/Si(111) and GaN/AlN/Si(100) are linear. The correlation coefficients of the best fit straight lines for them are 0.9978 and 0.9930, respectively. . The d_{33}' of GaN with AlN buffer layer grown on Si (111) and Si (100) can be obtained from the slope of the fitted straight line. A value of (2.65 ± 0.1) pmV^{-1} were found on both of the samples. Figures 5.10 and 5.13 show the variation of measured d_{33}' with frequency. d_{33}' is constant over the full frequency range except at frequencies above 50 kHz for the GaN/AlN/Si(111) and at 45 kHz for the GaN/AlN/Si(100) sample.

By using eq. (5.3), the corresponding value of d_{31}' was found to be (1.325 ± 0.1) pmV^{-1} for both the GaN/AlN/Si(111) and GaN/AlN/Si(100) sample.

5.6.4 Effect of the AlN Buffer on the Composite Films

Since AlN is also piezoelectric, the displacement $u = (u_{GaN} + u_{AlN})$ measured by the laser interferometer is actually the resultant displacements of the two layers. In order to find the displacements induced by GaN as well as by the AlN buffer layer individually, some parameters should be known. As stated in eq (3.2), d_{33} of the two different materials and the potential drop across each of the materials should be known. In Chapter three, we have calculated the potential drops across each of the layers in the composite films.

Tables 5.3 and 5.4 show the potential drops across each layer in the composite film in the frequency range of 5 – 10 kHz, which is the frequency range of the d_{33} measurements. The potential drops across the GaN and AlN layers are quite constant within this frequency range. The potential drop across the silicon substrate is negligible since it is two orders of magnitude small than that of GaN and AlN.

	5 kHz	6 kHz	7 kHz	8 kHz	9 KHz	10 kHz
Vac_{GaN} / Vac	0.817	0.816	0.816	0.816	0.815	0.815
Vac_{AlN} / Vac	0.182	0.183	0.183	0.183	0.184	0.184
Vac_{Si} / Vac	0.00359	0.00423	0.00489	0.00555	0.00622	0.00688

Table 5.3 The potential drop across each layer in the GaN/AlN/Si(111) composite sample at 5 – 10 kHz.

	5 kHz	6 kHz	7 kHz	8 kHz	9 kHz	10 kHz
Vac_{GaN} / Vac	0.828	0.824	0.821	0.819	0.818	0.817
Vac_{AlN} / Vac	0.177	0.180	0.181	0.182	0.183	0.184
Vac_{Si} / Vac	0.00466	0.00556	0.00646	0.00736	0.00826	0.00917

Table 5.4 The potential drop across each layer in the GaN/AlN/Si(100) composite sample at 5 – 10 kHz.

In the interferometry measurement, the piezoelectric coefficients are found to be (2.65 ± 0.1) pmV^{-1} for both composite samples. By using eq. (3.2), the piezoelectric coefficient of AlN reported in the literature [51] as well as the data shown in Tables 5.3 and 5.4, The d_{33}' coefficient of GaN was found to be (2.13 ± 0.1) pmV^{-1} for both samples.

5.6.5 Substrate Clamping Effect

All of the III-V nitrides used in the piezoelectric measurement were deposited on silicon substrates. The thin films were clamped by the substrate and constrained the expansion and contraction of the film which in turn affected the measured strain. As a result, the measured value of d_{33} is less than the true value of an unclamped sample. If one assumed that the thin film was clamped by the substrate and that the lateral strain is zero, then eq (1.33) can be used [13]:

$$d_{33}' = d_{33} - 2\left(\frac{d_{31}s_{13}^E}{s_{11}^E + s_{12}^E}\right) \tag{5.9}$$

where d_{33}' is the measured value and d_{33} is the true value of the piezoelectric coefficient. From eq. (5.9), the true d_{33} coefficient differs from the apparent coefficient by a corrective factor (the second term).

In order to use the above equation, the elastic compliances of AlN and GaN are required. Both AlN and GaN have a wurtzite structure, the compliances for a wurtzite structure are s_{11} (=s_{22}), s_{12}, s_{13} (=s_{23}), s_{33}, s_{44} (=s_{55}), and $s_{66} = 2 (s_{11} - s_{12})$ [2, p.141]. There are theoretical and experimental data available in the literature.

Tables 5.5 and 5.6 show several sets of the available compliance data, as well as the corrected d_{33} and d_{31} calculated by using eqs. (5.3) and (5.9).

References	S^E_{11}	S^E_{12}	S^E_{13}	d_{33}	d_{31}
Tsubouchi et al. (1981) [52] #	3.5	-1.0	-0.8	5.1	2.55
McNeil et al. (1993) [53] ##	2.9	-0.9	-0.5	4.9	2.45
Ruiz et al. (1994) [54] ###	2.5	-0.7	-0.5	5.0	2.5
Wright (1997) [55] ####	3.0	-0.9	-0.6	5.1	2.55

#	Measured from SAW phase velocity.
##	Measured from Brillouin scattering.
###	Calculated using Hartree-Fock Theory.
####	Calculated using the plane-wave pseudo potential method.

Table 5.5: Calculated values of the corrected d_{33} and d_{31} (in pmV^{-1}) coefficients for AlN film. The compliance data (in pm^{2}N^{-1}) reported in the literature used in the calculations are also included.

References	S^E_{11}	S^E_{12}	S^E_{13}	d_{33}	d_{31}
Sheleg et al. (1979) [56] @	5.1	-0.9	-2.5	3.4	1.70
Polian et al. (1996) [57] @@	2.6	-1.0	-0.6	3.0	1.50
Takagi et al. (1996) [58] @@	3.5	-0.9	-0.5	2.5	1.25
Wright (1997) [55] @@@	3.3	-1.0	-0.6	2.7	1.35

@	Measured from X-ray diffraction spectra.
@@	Measured from Brillouin scattering.
@@@	Calculated using the plane-wave pseudo potential method.

Table 5.6 Calculated values of the corrected d_{33} and d_{31} (in pmV^{-1}) coefficients for GaN film. The compliance data (in pm^{2}N^{-1}) reported in the literature used in the calculations are also included.

Table 5.5 shows the values of d_{33} and d_{31} coefficients of AlN which have been corrected for substrate clamping. Although there are different sets of reported compliances, the corrected piezoelectric coefficients based on them are quite similar. By choosing the sets of data reported from Tsubouchi et al. (1981) [52] and Wright (1997) [55], the corrected values of the d_{33} and d_{31} for AlN are found to be (5.10 ± 0.1) pmV^{-1} and (2.55 ± 0.1) pmV^{-1}, respectively.

Table 5.6 shows the values of d_{33} and d_{31} coefficients of GaN which have been corrected for substrate clamping. By choosing the sets of data reported from Takagi et al. (1996) [58] and Wright (1997) [55], since these compliances data are the most recent values reported and both of them gives two similar d_{33} values, the corrected values of the d_{33} and d_{31} for GaN are found to be (2.60 ± 0.1) pmV^{-1} and (1.30 ± 0.1) pmV^{-1}, respectively.

5.7 Piezoelectric Coefficients of Zinc Blende AlN and GaN

As described in section 5.3, both AlN and GaN can exist in either the wurtzite or zinc blende structure. The crystal structure of the nitride films are strongly influenced by the substrate material and its orientation. The zinc blende and wurtzite structures have similar physical properties, and the piezoelectric coefficients of the two structures are related by eqs. (5.1) and (5.2). The calculated piezoelectric coefficients of AlN and GaN in zinc blende structure are shown in Table 5.7.

Sample	d_{33}'' (pmV^{-1})	d_{14} (pmV^{-1})
AlN	5.1	8.8
GaN	2.6	4.5

Table 5.7 Calculated piezoelectric coefficients for AlN and GaN in zinc blende structure. Where the unprimed quantities in the above equation are related to the zinc blende structure, while the double primed quantities are related to the wurtzite structure.

5.8 Conclusions

The piezoelectric coefficients for AlN and GaN/AlN/Si have been measured by a Mach Zehnder type heterodyne interferometer. The d_{31}, d_{33}, and d_{14} of GaN have also been calculated from the composite film sample by considering the effect of the AlN buffer layer as well as the substrate.

When using laser interferometer to measure the surface vibration, sample mounting is very important. It is found that bending mode vibrations will occur even at low frequency measurements if the sample is not mounted properly. However, if the sample is rigidly mounted to the holder, the bending effects can be suppressed at low frequency measurements (below 40 kHz). One method to eliminate the bending effect is to reduce the size of the electrode.

Values of the d_{33} and d_{31} coefficients for AlN are found to be (5.10 ± 0.1) pmV^{-1} and (2.55 ± 0.1) pmV^{-1}, respectively. While the values of the d_{33} and d_{31} coefficients for GaN are found to be (2.60 ± 0.1) pmV^{-1} and (1.30 ± 0.1) pmV^{-1}, respectively. Both of the values were measured on polycrystalline thin film with correction for the substrate clamping.

CHAPTER SIX

VELOCITY CURVES, POWER FLOW ANGLES AND ELECTROMECHANICAL COUPLING COEFFICIENTS OF III-V NITRIDES

6.1 Introduction

By solving the Christoffel equation, we can find the phase velocities along different axes of a crystal with various symmetries. For a simple cubic crystal, it is possible to determine the eigenvalues by simply using the stiffness matrix. However, for other propagation directions, we need to solve the characteristic equation in order to find the phase velocities. The calculation is quite complex and time consuming if done manually. In order to solve the eigenvalue problem numerically, a program is written to solve the complex Christoffel equation and the results can provide an insight into the acoustic properties of the materials of interests.

Because of crystal anisotropy, the energy does not necessarily propagate in the direction parallel to the wave propagation. This property occurs in both optically and acoustically anistropic media. The angle between the direction of energy flow and the propagation direction is called the power flow angle. This angle depends on the shape of the inverse velocity (slowness) curve of the media. A program has also been written to calculate the power flow angle.

The electromechanical coupling coefficient is important when the piezoelectric crystal is used to convert electrical energy to mechanical energy or vice versa. This coefficient depends on the propagation direction, material stiffness matrix, piezoelectric matrix, dielectric matrix, and density. A program is written to calculate the electromechanical coupling coefficient, k_t.

6.2 Velocity Curve Calculation

6.2.1 The Christoffel Equation

The dynamic equations of motion for a 3-dimensional case are given by

$$\nabla \bullet \boldsymbol{T} = \rho \frac{\partial^2 \boldsymbol{u}}{\partial t^2} \tag{6.1}$$

$$\nabla_s \boldsymbol{u} = \boldsymbol{S} \tag{6.2}$$

where $\boldsymbol{T}$ is the stress matrix, $\boldsymbol{u}$ is the displacement matrix, ρ is the density of the material, t is time, $\boldsymbol{S}$ is the strain matrix, and ∇s is the gradient operator that transforms the displacement $\boldsymbol{u}$ into the strain matrix (it can be written as ∇_{Ij}, I = 1 to 6 and j = 1 to 3). Eq. (6.1) is the Newton's law and eq. (6.2) is the definition of strain. Our target is to manipulate these equations by using the constitutive relations and form a wave equation. Rewriting eqs. (6.1) and (6.2) in terms of $\boldsymbol{T}$ and the velocity matrix $\boldsymbol{v}$ (since $\boldsymbol{T}$ and $\boldsymbol{v}$ are in phase in both of the 1- and 3-dimensions models):

$$\nabla \bullet \boldsymbol{T} = \rho \frac{\partial \boldsymbol{v}}{\partial t} \tag{6.3}$$

$$\nabla_s \boldsymbol{u} = \frac{\partial \boldsymbol{S}}{\partial t} = \boldsymbol{s} : \frac{\partial \boldsymbol{T}}{\partial t} \tag{6.4}$$

Differentiating eq. (6.3) w.r.t. t and multiplying eq. (6.4) by the stiffness matrix $\boldsymbol{c}$, we have:

$$\nabla \bullet \frac{\partial \boldsymbol{T}}{\partial t} = \rho \frac{\partial^2 \boldsymbol{v}}{\partial t^2} \tag{6.5}$$

$$\nabla_s \boldsymbol{u} = \boldsymbol{c} : \boldsymbol{s} : \frac{\partial \boldsymbol{T}}{\partial t} = \frac{\partial \boldsymbol{T}}{\partial t} \tag{6.6}$$

Combining eqs. (6.5) and (6.6), we obtain:

$$\nabla \bullet \frac{\partial \boldsymbol{T}}{\partial t} = \nabla \bullet \boldsymbol{c} : \nabla_s \boldsymbol{v} = \rho \frac{\partial^2 \boldsymbol{v}}{\partial t^2} \tag{6.7}$$

Eq. (6.7) is the three-dimension wave equation. ($\nabla_s = \nabla_{Ij}$, where $I = 1$ to 6 and $j = 1$ to 3, and $\nabla\bullet$ is the transpose of ∇_{Ij}. So, $\nabla\bullet = \nabla_{iJ}$ where $i = 1$ to 3 and $J = 1$ to 6). Therefore, the three dimensional wave equation becomes:

$$\nabla_{iK} c_{KL} \nabla_{Lj} v_j = \rho \frac{\partial^2 v_i}{\partial t^2} \tag{6.8}$$

Let us now consider a plane wave propagating in a direction $\hat{l}$ (which is arbitrary) in the medium.

$$\hat{l} = l_x \hat{i} + l_y \hat{j} + l_z \hat{k} \tag{6.9}$$

where l_x, l_y and l_z are the projections of the unit vector $\hat{l}$ on the three axes. We know that the fields have the time and space dependence of

$$v \propto e^{j(\omega t - k\hat{l}\bullet r)} \tag{6.10}$$

where, $\boldsymbol{r} = x\hat{i} + y\hat{j} + z\hat{k}$ and $k = \omega / v_a$. we differentiate $e^{j(\omega t - k\hat{l}\bullet r)}$ r. w. t. x to obtain:

$$\frac{\partial}{\partial x} e^{j(\omega t - k\hat{l}\bullet r)} = -jkl_x e^{j(\omega t - k\hat{l}\bullet r)} = -jkl_x v \tag{6.11}$$

Analogous to x, the y and z components can be derived in a similar fashion. By using the result of eq. (6.11), the gradient and divergence operator matrices will become,

$$\nabla_{Lj}=\begin{bmatrix}\frac{\partial}{\partial x} & 0 & 0\\ 0 & \frac{\partial}{\partial y} & 0\\ 0 & 0 & \frac{\partial}{\partial z}\\ 0 & \frac{\partial}{\partial z} & \frac{\partial}{\partial y}\\ \frac{\partial}{\partial z} & 0 & \frac{\partial}{\partial x}\\ \frac{\partial}{\partial y} & \frac{\partial}{\partial x} & 0\end{bmatrix}\longrightarrow -jk\begin{bmatrix}l_x & 0 & 0\\ 0 & l_y & 0\\ 0 & 0 & l_z\\ 0 & l_z & l_y\\ l_z & 0 & l_x\\ l_y & l_x & 0\end{bmatrix}=-jkl_{Lj} \qquad (6.12)$$

and

$$\nabla_{iK}\longrightarrow -jk\begin{bmatrix}l_x & 0 & 0 & 0 & l_z & l_y\\ 0 & l_y & 0 & l_z & 0 & l_x\\ 0 & 0 & l_z & l_y & l_x & 0\end{bmatrix}=-jkl_{iK} \qquad (6.13)$$

So, we can rewrite eq. (6.8) in a simpler form:

$$\nabla_{iK}c_{KL}\nabla_{Lj}v_j\longrightarrow -(k^2 l_{iK}c_{KL}l_{Lj})v_j=-k^2\Gamma_{ij}v_j=-\rho\omega^2 v_i \qquad (6.14)$$

where

$$\Gamma_{ij}=l_{iK}c_{KL}l_{Lj} \qquad (6.15)$$

is called the Christoffel matrix. This matrix is a 3 X 3 matrix depending only on the propagation direction of the wave and the stiffness matrix of the crystal. Solving the Christoffel matrix involves solving an eigenvalue problem. The eigenvalues are the three real numbers that represent the three phase velocities of the waves. In addition, the three corresponding eigenvectors are the particle velocity directions, which are defined as the acoustic polarization. [59, p.60].

6.2.2 Christoffel Equation for Piezoelectric Crystals

Table 6.1 shows the electrical and acoustic equations

Electrical	*Acoustic*
Faraday's law $\nabla \times \boldsymbol{E} = -\frac{\partial \boldsymbol{B}}{\partial t}$ Ampere's law $\nabla \times \boldsymbol{H} = \frac{\partial \boldsymbol{D}}{\partial t} + \boldsymbol{J}$ $\boldsymbol{B} = \mu \boldsymbol{H}$	Newton's law $\nabla \bullet \boldsymbol{T} = \rho \frac{\partial v}{\partial t}$ Definition of strain $\nabla_s v = \frac{\partial S}{\partial t}$
Uncoupled (nonpiezoelectric)	
$\boldsymbol{D} = \varepsilon \bullet \boldsymbol{E}$	$\boldsymbol{T} = c : \boldsymbol{S}$
coupled (piezoelectric)	
$\boldsymbol{D} = \varepsilon^S \bullet \boldsymbol{E} + \boldsymbol{e} : \boldsymbol{S}$ (6.16)	$\boldsymbol{T} = -\boldsymbol{e} : \boldsymbol{E} + \boldsymbol{c}^E : \boldsymbol{S}$ (6.17)

Table 6.1 The electrical and acoustic equations.

The fundamental physical laws are not altered by piezoelectricity. Multiplying the strain equation by c^E and differentiating Eq. (6.17) w. r. t. t, we obtain:

$$\boldsymbol{c}^E : \nabla_s v = \boldsymbol{c}^E : \frac{\partial S}{\partial t} \qquad (6.18)$$

$$c^E : \frac{\partial S}{\partial t} = \frac{\partial T}{\partial t} + e : \frac{\partial E}{\partial t} \tag{6.19}$$

Substitute eq. (6.18) into eq. (6.19), we obtain:

$$\frac{\partial T}{\partial t} = c^E : \nabla_s v - e : \frac{\partial E}{\partial t} \tag{6.20}$$

Now, substituting eq. (6.20) into eq. (6.5), we have

$$\nabla \bullet c^E : \nabla_s v - \nabla \bullet e : \frac{\partial E}{\partial t} = \rho \frac{\partial^2 v}{\partial t^2} \tag{6.21}$$

Eq. (6.21) is the Christoffel equation with an electrical perturbation.

We now consider the electromagnetic wave equation in three dimensions:

$$-\nabla \times \nabla \times E = \mu_o \frac{\partial^2 D}{\partial t^2} \tag{6.22}$$

Substitute eq. (6.16) into eq. (6.22), we obtain

$$-\nabla \times \nabla \times E = \mu_o \varepsilon^S : \frac{\partial^2 E}{\partial t^2} + \mu_o e : \frac{\partial^2 S}{\partial t^2} \tag{6.23}$$

Eliminating the strain term by substituting eq. (6.4) into eq. (6.23) gives,

$$-\nabla \times \nabla \times E = \mu_o \varepsilon^S : \frac{\partial^2 E}{\partial t^2} + \mu_o e : \nabla_s \frac{\partial v}{\partial t} \tag{6.24}$$

Eq. (6.24) is the electromagnetic wave equation with an acoustic perturbation term. Both eqs. (6.21) and (6.24) are the desired equations which couple the electric field ***E*** into the acoustic field ***v***.

We now consider the coupling terms in eqs. (6.21) and (6.24). The electrical perturbation term in eq. (6.21) is

$$\nabla \bullet e : \frac{\partial E}{\partial t} \longrightarrow \nabla_{iJ} e_{Jk} \frac{\partial E_k}{\partial t} \xrightarrow[\text{planewave}]{} -jkl_{iJ} e_{Jk} \frac{\partial E_k}{\partial t} \tag{6.25}$$

while the acoustic perturbation term in the electromagnetic wave equation is

$$\mu_o e : \nabla_s \frac{\partial v}{\partial t} \longrightarrow \mu_o e_{il} \nabla_{lj} v_j \xrightarrow[planewave]{} \mu_o e_{il} (-jkl_{lj}) v_j \qquad (6.26)$$

In eqs. (6.21) and (6.24), we have assumed that the presence of the acoustic wave does not cause electromagnetic radiation in the medium. i.e. there is no coupling between ***E*** (created by the wave) and ***H***, and there is no electromagnetic energy induced due to the acoustic wave. This assumption is called the quasi-static approximation [59, p.140].

The approximation also assume that there is no coupling to electromagnetic wave with an acoustic wave, thus no magnetic field is generated by the acoustic wave, that implies:

$$\nabla \times \boldsymbol{E} = 0 \qquad (6.27)$$

From eq. (6.27), one can write the electric field as the gradient of a scalar potential:

$$\boldsymbol{E} = -\nabla \Phi \qquad (6.28)$$

Substituting eq. (6.28) into eq. (6.21) and taking the divergence of (6.24), we have

$$\nabla \bullet c^E : \nabla_s v + \nabla \bullet e : \frac{\partial \nabla \Phi}{\partial t} = \rho \frac{\partial^2 v}{\partial t^2} \qquad (6.29)$$

$$0 = -\mu_o \nabla \bullet \varepsilon^S : \frac{\partial^2 \nabla \Phi}{\partial t^2} + \mu_o \nabla \bullet \left(e : \nabla_s \frac{\partial v}{\partial t} \right) \qquad (6.30)$$

We now convert to the plane wave formalism. For eq. (6.29):

$$-k^2 (l_{iK} c_{KL} l_{Lj}) v_j + \rho \omega^2 v_i = j\omega k^2 (l_{iK} e_{Kj} l_j) \Phi \qquad (6.31)$$

It is because $\nabla \Phi \rightarrow (-jk)(l_j \Phi)$, so

$$0 = \omega^2 k^2 (l_i \varepsilon_{ij} l_j) \Phi - j\omega k^2 (l_i e_{iL} l_{Lj}) v_j \qquad (6.32)$$

By solving eq. (6.31) and (6.32), one gives

$$\Phi = \frac{1}{j\omega}\left(\frac{(l_i e_{iL} l_{Lj})v_j}{l_i \varepsilon_{ij}^S l_j}\right) \tag{6.33}$$

Substituting eq. (6.33) into eq. (6.31) gives the Christoffel equation for piezoelectric crystals.

$$k^2\left(l_{iK}\left(c_{KL}^E + \frac{(e_{Kj}l_j)(l_i e_{iL})}{l_i \varepsilon_{ij}^S l_j}\right)l_{Lj}\right)v_j = \rho\omega^2 v_i \tag{6.34}$$

By comparison with the non-piezoelectirc Christoffel equation (6.14)

$$(k^2 l_{iK} c_{KL} l_{Lj})v_j = \rho\omega^2 v_i$$

We can see that both Christoffel equations having the same form. However, there is an extra terms in the piezoelectric stiffened one. The piezoelectric and permittivity matrices are added to the stiffness matrix. Therefore, we can say that the components of the stiffness matrix have been piezoelectrically stiffened.

6.2.3 Solution to the Christoffel Equation

After solving the Christoffel equation, we will have three solutions (one is the velocity of the longitudinal wave while the other two are the shear waves). Each mode of the wave is associated with its particular stiffness constant. For some simple directions of propagation, the required velocity can be deduced from the stiffness matrix. However, for some off-axis directions, the solutions cannot be easily found, they are combinations of different stiffness components. The calculation is quite cumbersome if done manually.

In Appendix II, a computer program, called Christoffel, is given to solve the Christoffel matrix. The program is written in the Turbo PASCAL 6.0 language for the PC. With known material stiffness matrix, piezoelectric matrix, dielectric matrix, and density, the program solves the Christoffel equation in a chosen propagation direction (reference axes). The program can be used to plot the acoustic phase velocity as a function of the angle in a designated crystal plane. The program can also show both of the stiffened and unstiffened phase velocity curve. However, velocity curves for the unstiffened ones are not shown here.

The program is divided into five blocks:

1: Input of the stiffness matrix (GPa), piezoelectric matrix (Cm^{-2}), dielectric matrix, and density of the material (g/cm^{-3}). Since the form of the stiffness matrix is determined by the symmetry of the material, it is not necessary to input the symmetry classes.

2: Input of the propagation direction. By in-putting two perpendicular axes that can be positioned arbitrarily in the three dimensional space. The propagation direction l is the normal of the plane formed by the two input axes.

3: Formation of the Christoffel matrix.

$$\Gamma_{ij} = l_{iK}\left(c_{KL} + \frac{[e_{Kj} l_j][l_i e_{iL}]}{l_i \varepsilon_{ij}^{S} l_j} \right) l_{Lj} \qquad (6.35)$$

where l_{iK} and l_{Lj} are the 3 X 6 and 6 X 3 matrices, respectively, and l_i and l_j are the 1 X 3 and 3 X 1 matrices.

4: Solving the eigenvalue problem.

$$|\Gamma - \lambda| = 0 \qquad (6.36)$$

5: Γ is a 3 X 3 matrix. After solving eq. (6.36), Γ will become a cubic equation. The computer then can find the other solutions.

6.2.4 Results

In order to use the program, the stiffness matrix, piezoelectric matrix, dielectric matrix, and density of the AlN and GaN must be known. From the reports of L.E. McNeil *et al.* (1993) and R.B. Schwarz *et al.* (1997), we obtained the stiffness matrix components of AlN [53] and GaN [60], respectively. Table 6.1 shows the stiffness data reported by them.

	c_{11}	c_{33}	c_{44}	c_{12}	c_{13}
AlN	410.5	388.5	124.6	148.5	98.9
GaN	377	209	81.4	160	114

Table 6.2 The stiffness matrix components (in the units of GPa) of AlN and GaN.

In the program, we should input the piezoelectric stress coefficients (i.e. *e*-coefficients). However, In this work, we have measured the piezoelectric strain coefficients (i.e. *d*-coefficients). In order to use the program. We have transformed the *d*-coefficients into *e*-coefficients by using the following equations [61].

$$e_{14} = d_{14}c_{44}^{E} \tag{6.37}$$

$$e_{15} = d_{15}c_{44}^{E} \tag{6.38}$$

$$e_{31} = d_{31}(c_{11}^{E} + c_{12}^{E}) + d_{33}c_{13}^{E} \tag{6.39}$$

$$e_{33} = 2d_{31}c_{13}^{E} + d_{33}c_{33}^{E} \tag{6.40}$$

By using the stiffness data quoted in Table 6.1, the values of d_{15} for AlN and GaN together with (–3.6 pmV^{-1} and –3.1 pmV^{-1}, respectively, reported by S. Muensit *et al.* [62]) the measured d_{33} and d_{31} in this work, we can obtain the *e*-coefficients of AlN and GaN. Table 6.2 shows the results of the calculation.

	Hexagonal Structure			Cubic structure
	e_{31}	e_{33}	e_{15}	e_{14}
AlN	-0.92	1.48	-0.45	1.10
GaN	-0.40	0.25	-0.25	0.37

Table 6.3 The piezoelectric stress coefficients (in units of Cm^{-2}) of AlN and GaN.

The components of dielectric matrix of a hexagonal structure are two non zero constants, ε_{11} and ε_{33}. From the literature, we can obtained ε_{11} and ε_{33} for AlN as 9 and 11, respectively [63], while the values of ε_{11} and ε_{33} for GaN are 9.5 and 10.4, respectively [64]. The density of wurtzite AlN and GaN are 3230 kgm^{-3} and 6150 kgm^{-3}, respectively.

6.2.4.1 Wurtzite AlN

The complied data for wurtzite AlN are shown in Figure 6.1 and the velocity curves of AlN in the XY plane and in the plane containing the vectors (1,1,1) and (-2,1,1) are shown in Figure 6.2 and 6.3, respectively.

410.5	148.5	98.9	0	0	0	0	0	-0.92
148.5	410.5	98.9	0	0	0	0	0	-0.92
98.9	98.9	388.5	0	0	0	0	0	1.48
0	0	0	124.6	0	0	0	-0.45	0
0	0	0	0	124.6	0	-0.45	0	0
0	0	0	0	0	131	0	0	0
0	0	0	0	-0.45	0	9	0	0
0	0	0	-0.45	0	0	0	9	0
-0.92	-0.92	1.48	0	0	0	0	0	11

Figure 6.1 The elasto-piezo-dielectric matrix of AlN (The unit of stiffness constants is GPa, while the piezoelectric stress constants is Cm^{-2}).

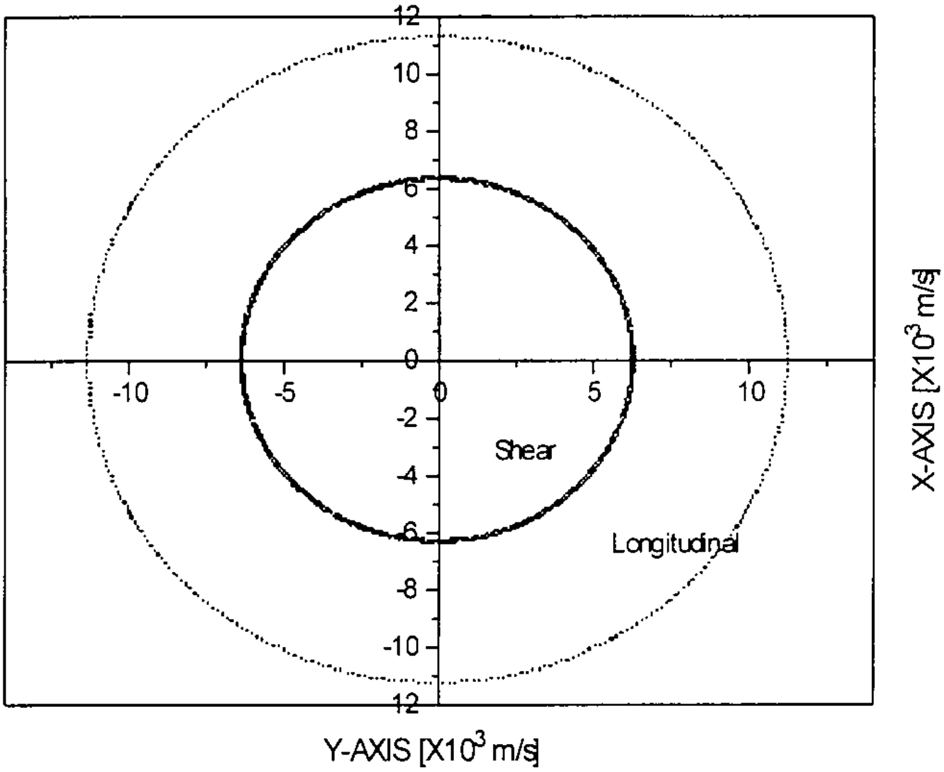

Figure 6.2 The velocity curve of AlN in the XY plane.

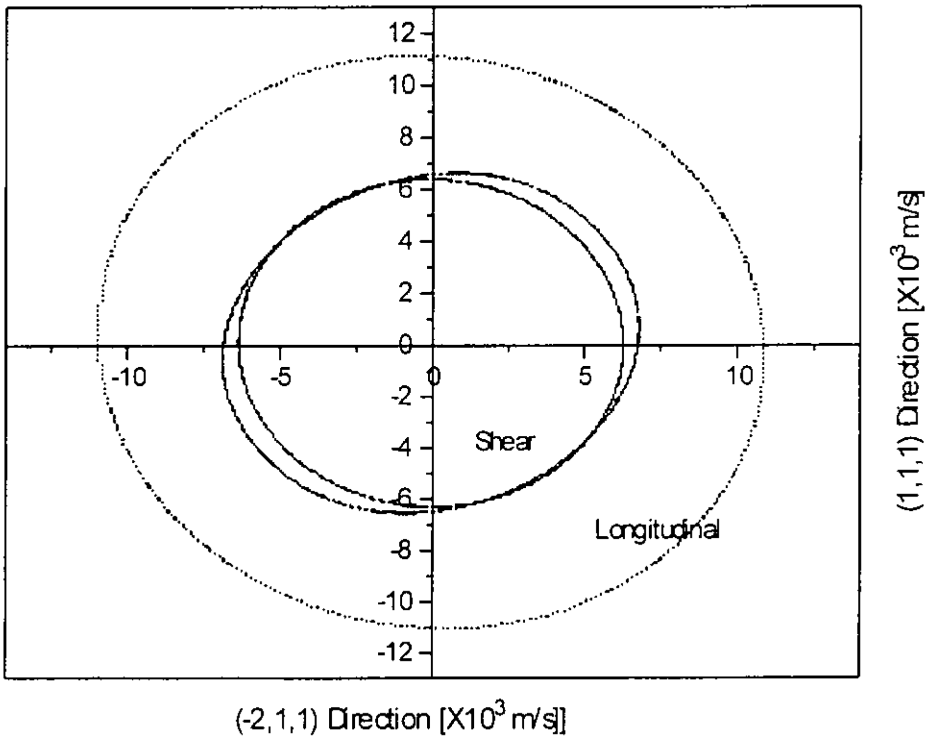

Figure 6.3 The velocity curve of AlN in the plane containing the vectors (1,1,1) and (-2,1,1).

6.2.4.2 Wurtzite GaN

The complied data for wurtzite GaN are shown in Figure 6.4 and the velocity curves of GaN in the XY plane and in the plane containing the vectors (1,1,1) and (-2,1,1) are shown in Figures 6.5 and 6.6, respectively.

377	160	114	0	0	0	0	0	-0.40
160	377	114	0	0	0	0	0	-040
114	114	209	0	0	0	0	0	0.25
0	0	0	81.4	0	0	0	-0.25	0
0	0	0	0	81.4	0	-0.25	0	0
0	0	0	0	0	108.5	0	0	0
0	0	0	0	-0.25	0	9.5	0	0
0	0	0	-0.25	0	0	0	9.5	0
-0.40	-0.40	0.25	0	0	0	0	0	10.4

Figure 6.4 The elasto-piezo-dielectric matrix of GaN (The unit of stiffness constants is GPa, while the piezoelectric stress constants is Cm^{-2}).

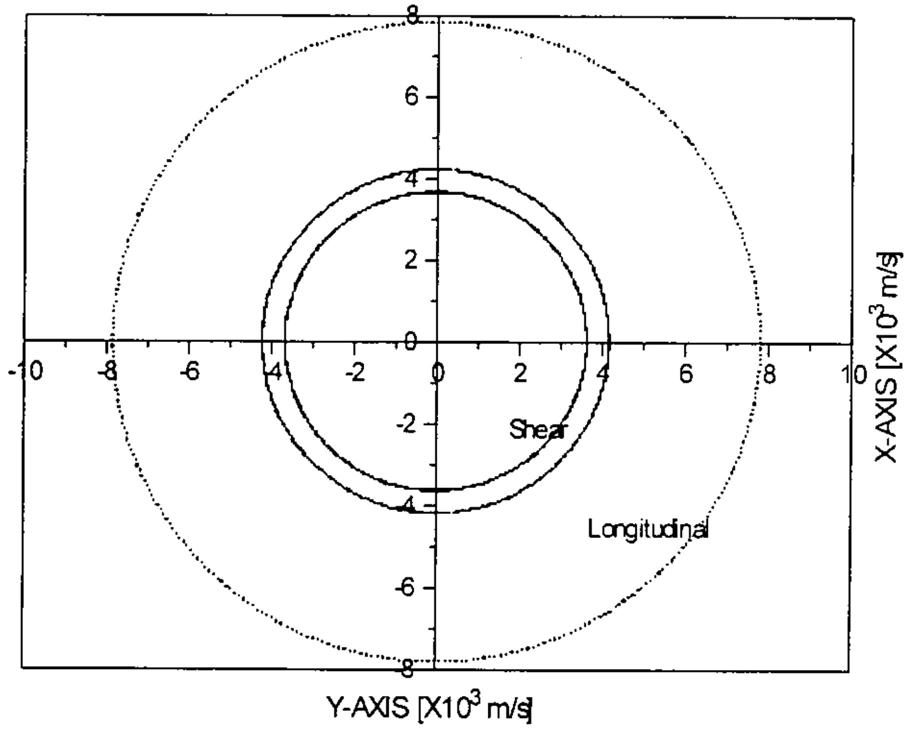

Figure 6.5 The velocity curve of GaN in the XY plane.

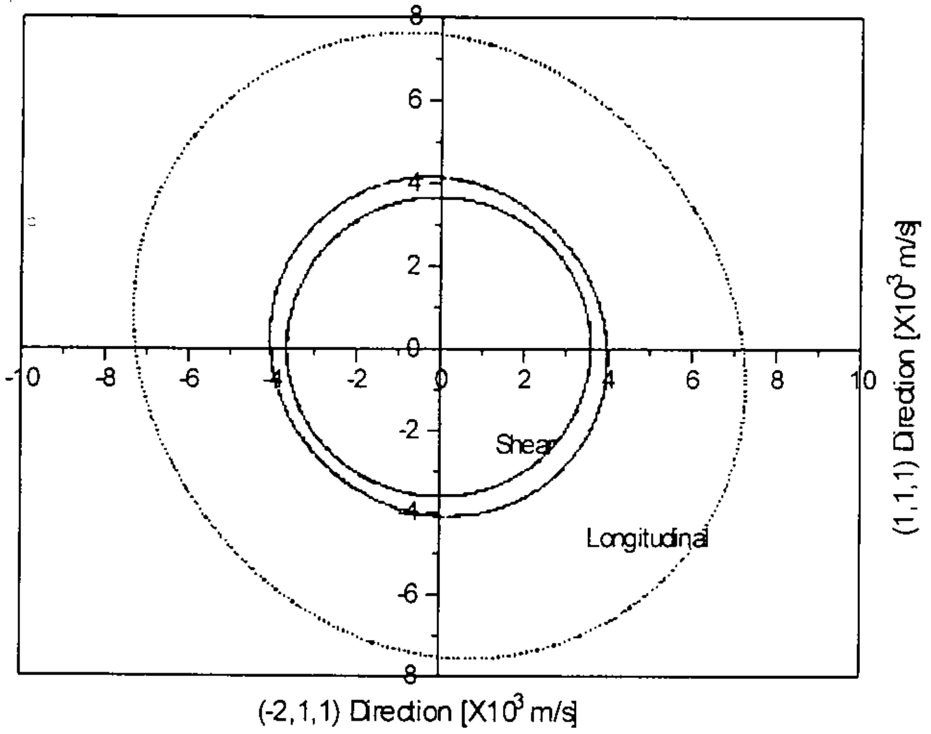

Figure 6.6 The velocity curve of GaN on the plane of consisted by vectors (1,1,1) and (-2,1,1).

6.2.4.3 Wurtzite ZnO

The complied data for wurtzite ZnO are shown in Figure 6.7 and the velocity curves of ZnO in the XY plane and in the plane containing the vectors (1,1,1) is shown in Figure 6.8.

210	121	105	0	0	0	0	0	-0.57
121	210	105	0	0	0	0	0	-0.57
105	105	211	0	0	0	0	0	1.32
0	0	0	43	0	0	0	-0.48	0
0	0	0	0	43	0	-0.48	0	0
0	0	0	0	0	44.5	0	0	0
0	0	0	0	-0.48	0	8.6	0	0
0	0	0	-0.48	0	0	0	8.6	0
-0.57	-0.57	1.32	0	0	0	0	0	10

Figure 6.7 The elasto-piezo-dielectric matrix of ZnO [59] (The unit of stiffness constants is GPa, while the piezoelectric stress constants is Cm^{-2}).

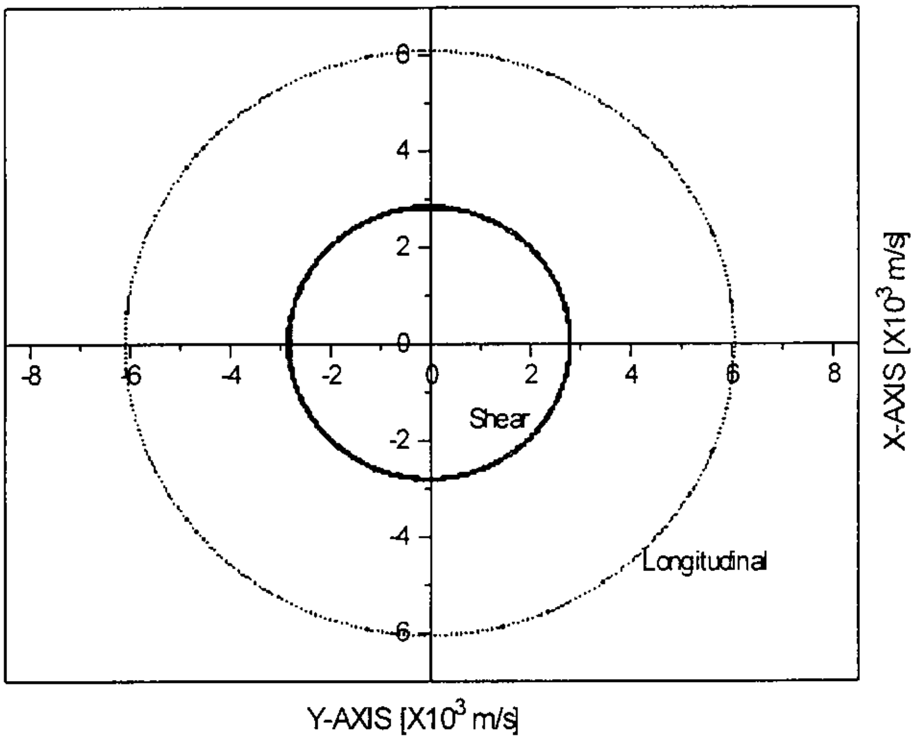

Figure 6.8 shows the velocity curve of ZnO on the XY plane. The density of ZnO is 5700 kgm^{-3} [59].

6.2.4.4 Zinc Blende GaAs

The complied data for zinc blende GaAs are shown in Figure 6.9 and the velocity curves of GaAs in the XY plane is shown in Figure 6.10.

119	53.8	53.8	0	0	0	0	0	0
53.8	119	53.8	0	0	0	0	0	0
53.8	53.8	119	0	0	0	0	0	0
0	0	0	59.4	0	0	0.154	0	0
0	0	0	0	59.4	0	0	0.154	0
0	0	0	0	0	59.4	0	0	0.154
0	0	0	0.154	0	0	12.5	0	0
0	0	0	0	0.154	0	0	12.5	0
0	0	0	0	0	0.154	0	0	12.5

Figure 6.9 The elasto-piezo-dielectric matrix of GaAs [59] (The unit of stiffness constants is GPa, while the piezoelectric stress constants is Cm^{-2}).

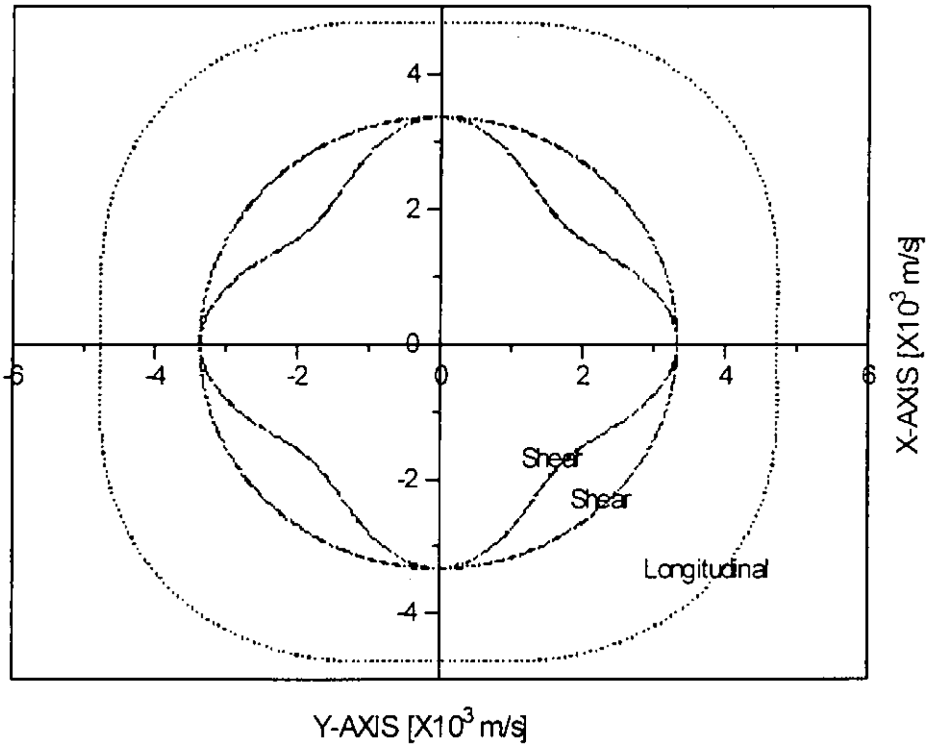

Figure 6.10 The velocity curve of GaAs on the XY plane. The density of GaAs is 5300 kgm^{-3} [59].

6.3 Power Flow Angle Calculation

6.3.1 The Power Flow Angle

When we calculate the power flow angle, two equations are needed:

$$\delta k \bullet v_e = 0 \tag{6.41}$$

$$\hat{l} \bullet v_e = v_a \tag{6.42}$$

where v_e is a vector showing the velocity of energy propagation (equal to the group velocity). The derivation of eqs. (6.41) and (6.42) are given by M. Born and E. Wolf [65]. These equations can be used to calculate the property of optical and acoustical waves in anistropic media.

Consider a section of an arbitrary slowness (1/velocity) curve shown in Figure 6.11. The magnitudes of the vectors for a given frequency are:

$$\left|\frac{k_1}{\omega}\right| = \frac{1}{v_{a1}} \quad (6.43) \qquad \text{and} \qquad \left|\frac{k_2}{\omega}\right| = \frac{1}{v_{a2}} \quad (6.44)$$

Taking the limit where $k_2 \rightarrow k_1$, the vector $\delta k/\omega$ becomes the tangent to the slowness curve. The direction of this tangent vector with respect to the coordinate axes depends on $\hat{l}$. Eq. (6.41) shows that the energy velocity (or group velocity) is normal to the vector $\delta k/\omega$ (i.e. normal to the slowness curve) because the scalar product of them is zero. Therefore, the angle between the energy velocity vector and the propagation direction vector depends on the shape of the slowness curve. From eq. (6.42), we can have the following relation:

$$v_a = |v_e|\cos\phi \tag{6.45}$$

where ϕ is called the power flow angle. According to eqs. (6.43) and (6.44), in order to find the power flow angle, we should have the slowness curve of the materials (the slowness is the inverse of the velocity). To obtain the slowness curve by using the Christoffel program, we only need to invert the phase velocities obtained from the program.

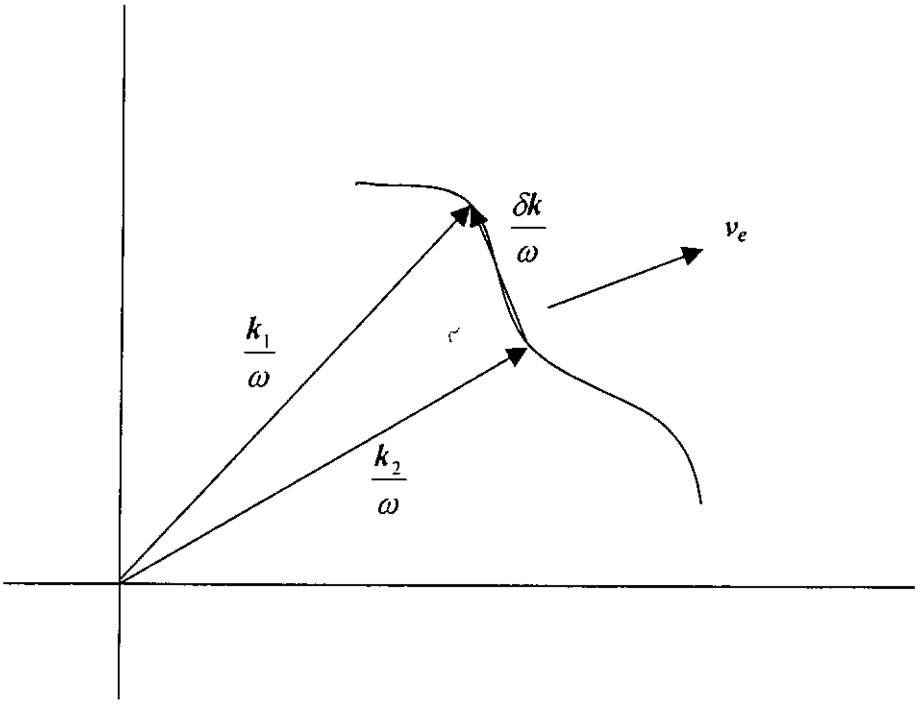

Figure 6.11 Part of an arbitrary slowness curve.

6.3.2 Solution of the Power Flow Angle

In Appendix III, a computer program called PFA is given which is an extension of the program Christoffel. It can be used to calculate the power flow angle of different materials. The inputs to the program PFA are similar to the program Christoffel, we should input the propagation direction (reference axes), material stiffness matrix, piezoelectric matrix, dielectric matrix, and density. The program plots the power flow angle, ϕ, as a function of the angle relative to the reference axes, θ.

In addition to the five steps in the program Christoffel to solve the Christoffel equation, the program PFA have four more steps in order to find the power flow angle. These are:

1: Form the vector as shown in eq. (6.46)

$$\frac{\delta k}{\omega} = \frac{\hat{l}_2}{v_{a2}} - \frac{\hat{l}_1}{v_{a1}} \qquad (6.46)$$

2: Normalize the vector

3: Rotate the vector by 90°

4: Form the dot product with either $\hat{l}_1$ or $\hat{l}_2$:

$$\frac{\delta k}{\omega} \bullet \hat{l}_2 = \cos\phi \qquad (6.47)$$

6.3.3 Results

6.3.3.1 Wurtzite AlN

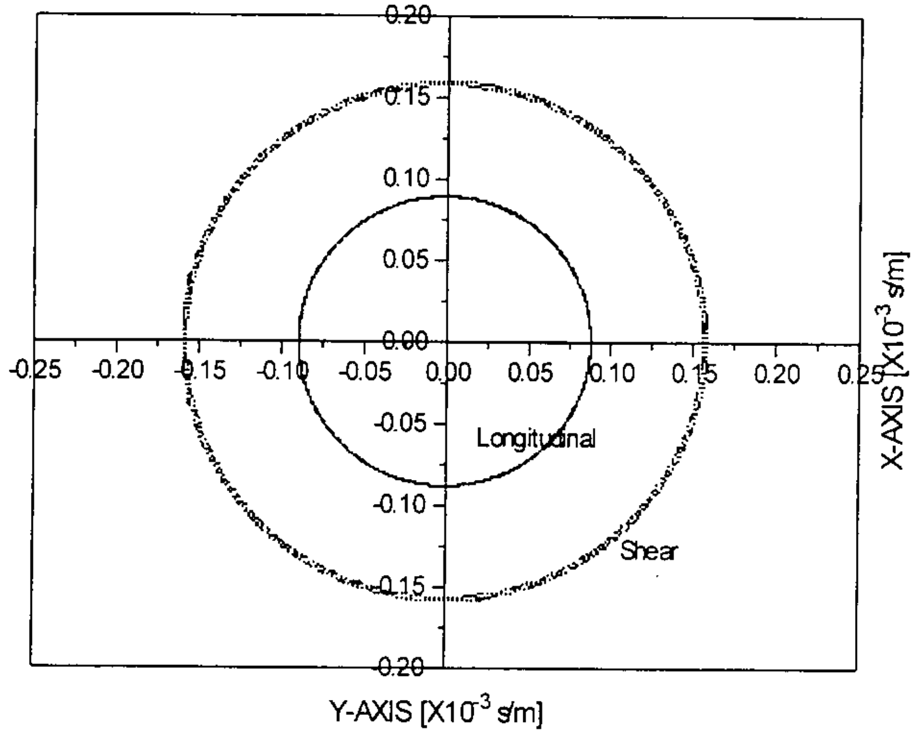

Figure 6.12 The slowness curve of wurtzite AlN in the XY plane.

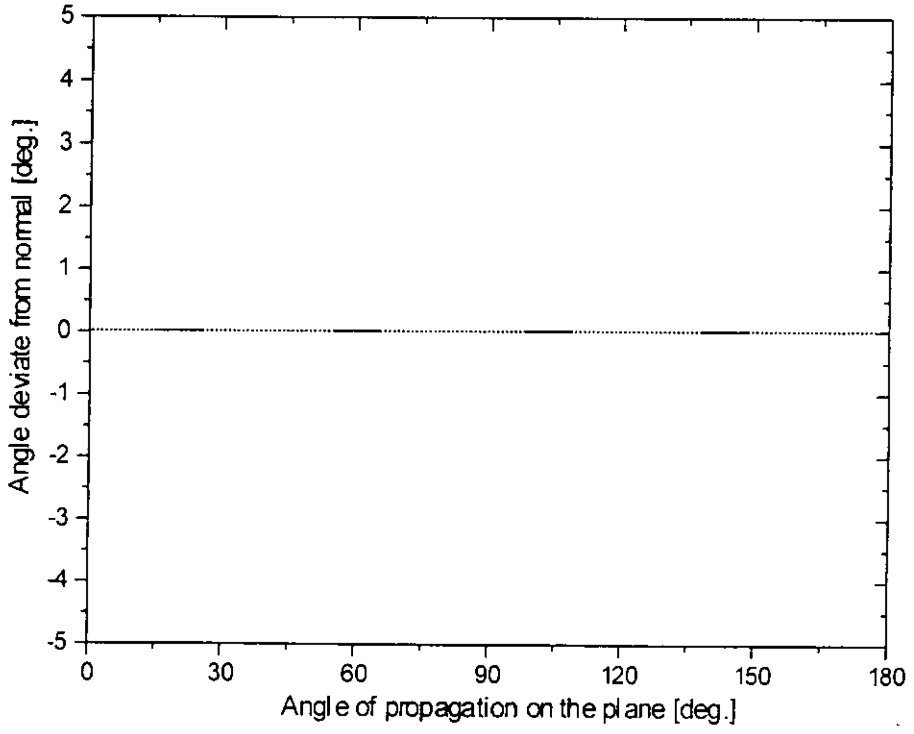

Figure 6.13 The power flow angle of wurtzite AlN in the XY plane.

6.3.3.2 Wurtzite GaN

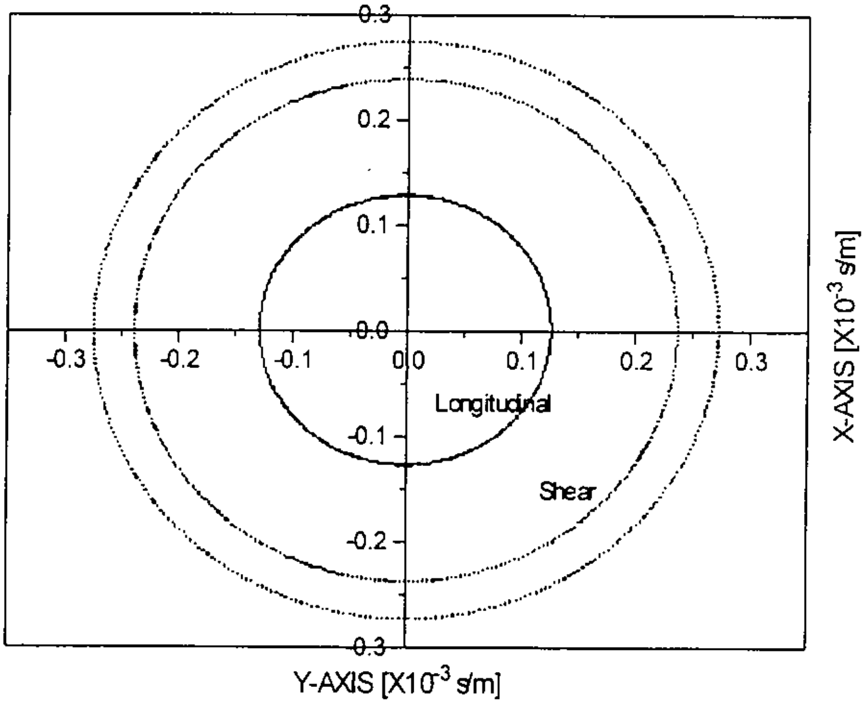

Figure 6.14 The slowness curve of wurtzite GaN in the XY plane.

From Figures 6.12 and 6.14, we found that the slowness curves of AlN and GaN in the XY plane are circular in shape. By using the program PFA to calculate the power flow angle, it is found that the power flow angle of wurtzite AlN and GaN in the XY plane are zero.

6.3.3.3 Wurtzite ZnO

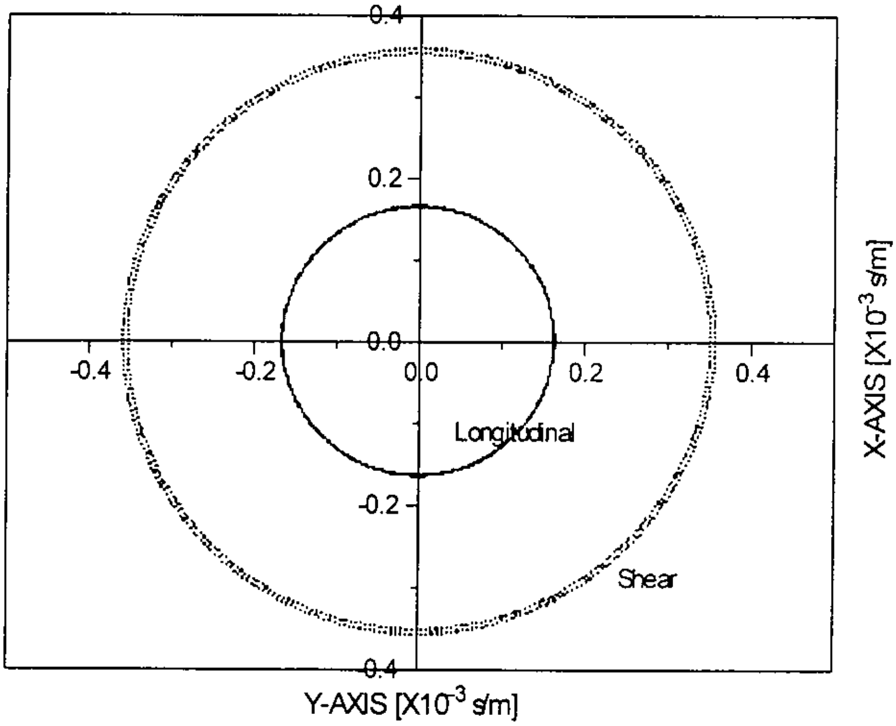

Figure 6.15 The slowness curve of wurtzite ZnO in the XY plane.

From Figure 6.15, we found that the slowness curves of ZnO in the XY plane are circular in shape. By using the program PFA to find the power flow angle, it is found that the power flow angles of wurtzite ZnO in the XY plane are zero.

6.3.3.4 Zinc blende GaAs

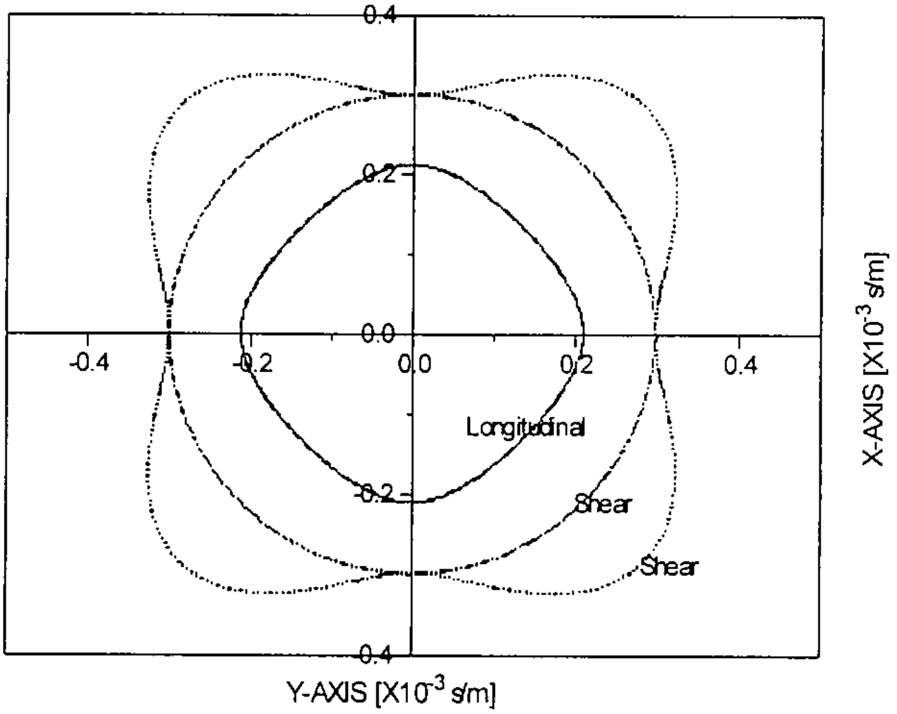

Figure 6.16 The slowness curve of zinc blende GaAs in the XY plane.

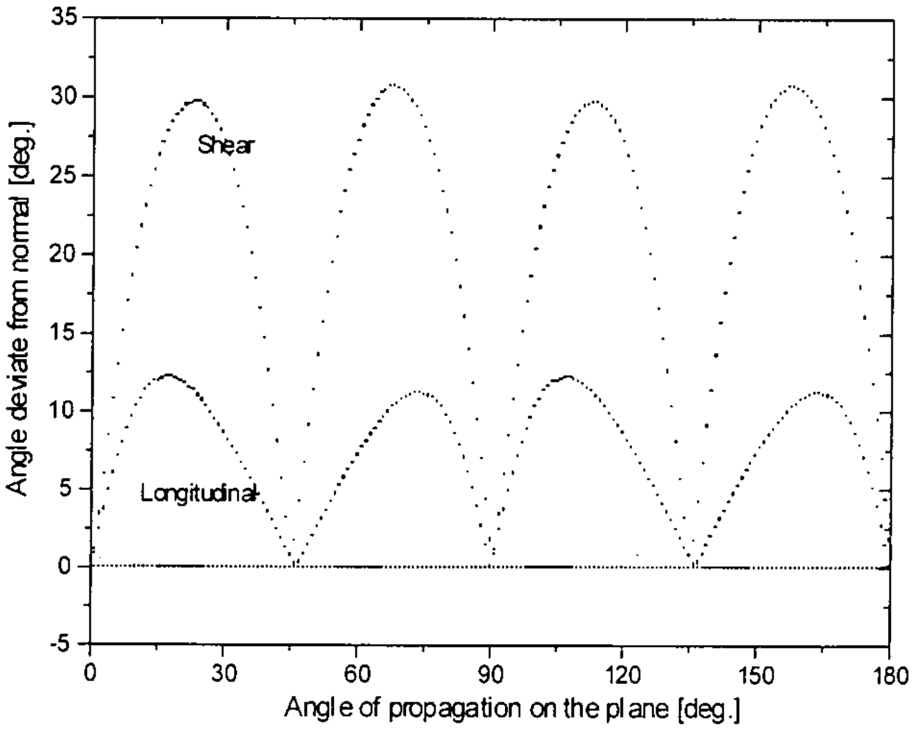

Figure 6.17 The power flow angle of zinc blende GaAs in the XY plane.

From Figure 6.17, it is found that the power flow angle of GaAs can be as high as 30° in some off-axis direction.

6.4 Electromechanical Coupling Coefficient Calculation

6.4.1 The Electromechanical Coupling Constant

In section 6.2, we mentioned that the piezoelectric corrections to the stiffness matrix depend not only on the piezoelectric stress e-matrix, but also on the crystal symmetry and the direction of propagation. Therefore, while a crystal is strongly piezoelectric along certain directions, the effect may completely disappear in a different direction [59, p.146].

From eq. (6.35), the stiffened phase velocity is

$$v_a^{'} = \sqrt{\frac{c'^E}{\rho}} = \sqrt{\frac{c^E + e^2/\varepsilon^S}{\rho}} \qquad (6.48)$$

where all the variables in eq. (6.48) depend on the direction of propagation $\hat{l}$. In order to determine the piezoelectric correction quantitatively, we first find the unstiffened phase velocity:

$$v_a = \sqrt{\frac{c^E}{\rho}} \qquad (6.49)$$

Rewriting eq. (6.48), it becomes

$$v_a^{'} = v_a(1+K^2)^{1/2} \qquad (6.50)$$

where

$$K^2 = \frac{e^2}{c^E \varepsilon^S} \tag{6.51}$$

K^2 is called the piezoelectric coupling coefficient and the electromechanical coupling coefficient k_t as:

$$k_t^2 = \frac{K^2}{1+K^2} \tag{6.52}$$

6.4.2 Solution of the Electromechanical Coupling Coefficient

In Appendix IV. a computer program called EMCC is written which is another variation of the program Christoffel. It can be used to calculate th electromechanical coupling coefficient of different materials. We should input the propagation directions (reference axes), material stiffness matrix, piezoelectric matrix, dielectric matrix, and density. The program plots the electromechanical coupling coefficient, k_t, as a function of the angle relative to the reference axes, θ.

An alternative technique to determine k_t is by using eq. (6.48) for any crystal in any direction of acoustic propagation direction.

1: Solve the Christoffel equation and determine the phase velocities without using the piezoelectric stress matrix.

2: Solve the Christoffel equation by using the piezoelectric stress matrix.

3: Form the ratio on each of the mode:

$$K^2 = \frac{(v_a' - v_a)^2}{v_a'} \approx \frac{2\Delta v_a}{v_a'} \tag{6.53}$$

where v_a' and v_a are the stiffened and unstiffened veloicities and Δv_a is their difference.

4: Form the ratio:

$$k_t = \sqrt{\frac{K^2}{1+K^2}} \tag{6.54}$$

6.4.3 Results

6.4.3.1 Wurtzite AlN

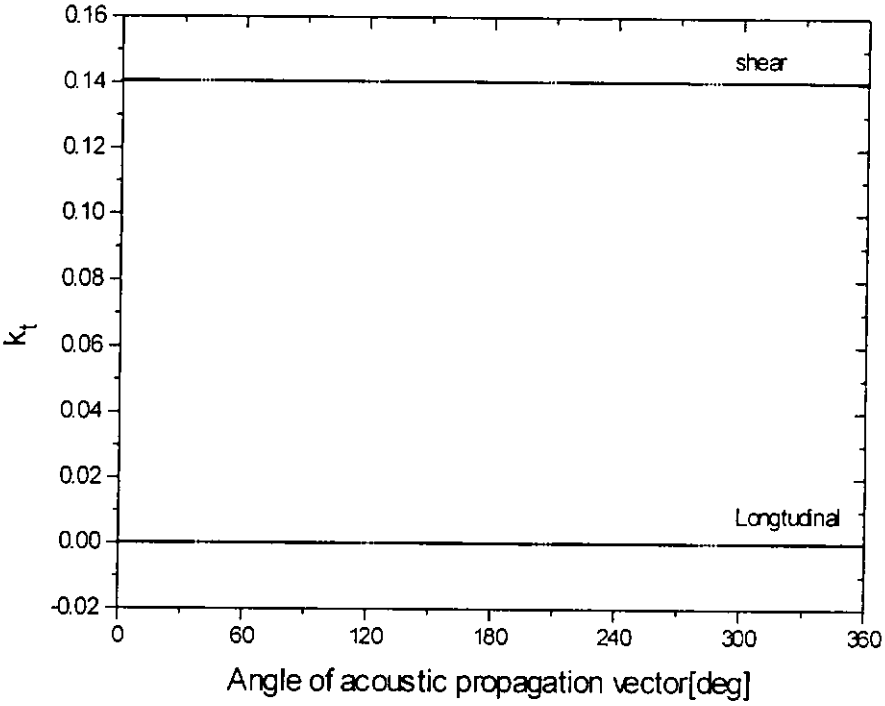

Figure 6.18 The electromechanical coupling coefficient of wurtzite AlN in the XY plane.

6.4.3.2 Wurtzite GaN

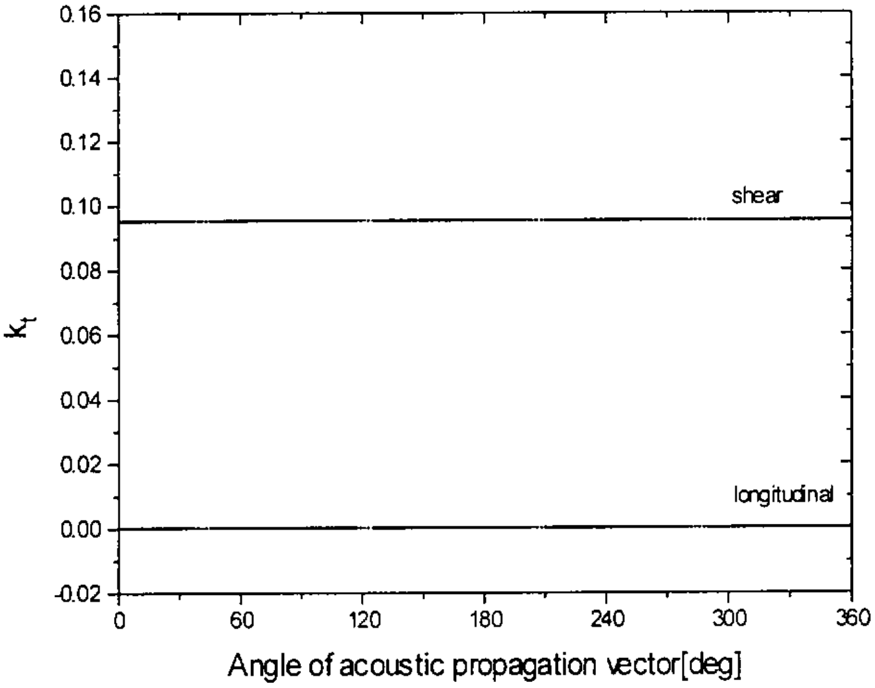

Figure 6.19 The electromechanical coupling coefficient of wurtzite GaN in the XY plane.

6.4.3.3 Wurtzite ZnO

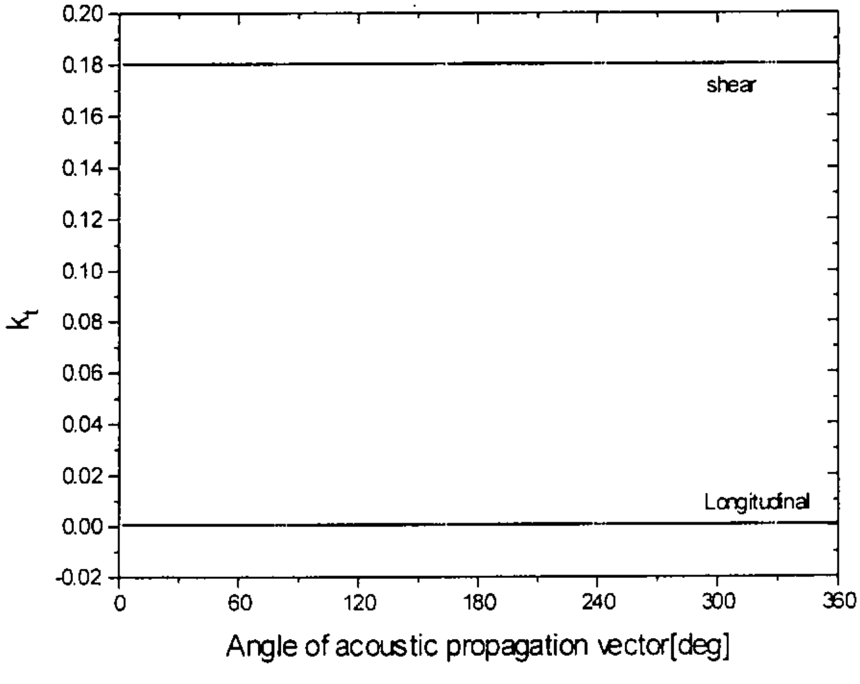

Figure 6.20 The electromechanical coupling coefficient of wurtzite ZnO in the XY plane.

6.4.3.4 Zinc blende GaAs

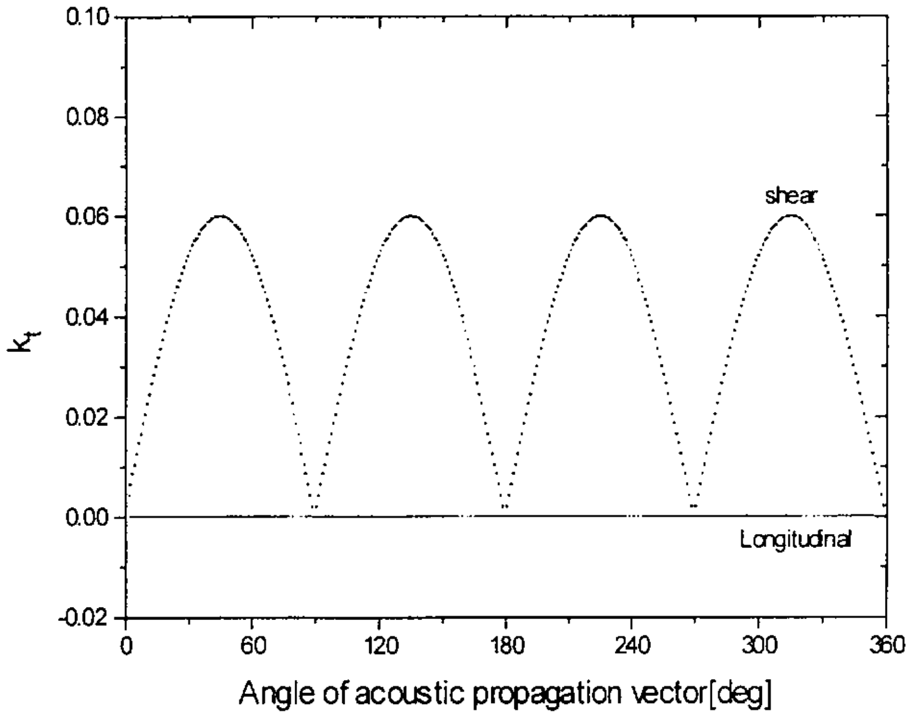

Figure 6.21 The electromechanical coupling coefficient of wurtzite GaAs in the XY plane.

From Figures 6.18 – 6.20, we found that the electromechanical coupling coefficients of AlN, GaN and ZnO in the XY plane are constant over the acoustic propagation angle, and there is only one shear mode wave has a non-zero k_t (This is only true for the case when we consider the XY plane, since the k_t depends on the propagation direction also). However, when we look at the k_t of zinc blende GaAs, there is also only one shear mode wave having a non-zero k_t and it is not a constant w.r.t. the acoustic propagation angle.

6.5 Conclusions

	Longitudinal Wave velocity along		*Shear Wave velocity along*		*Shear wave velocity along*	
	X-axis	*Y*-axis	*X*-axis	*Y*-axis	*X*-axis	*Y*-axis
AlN	11.3	11.3	6.37	6.37	6.27	6.27
GaN	7.83	7.83	4.2	4.2	3.65	3.65
ZnO	6.07	6.07	2.84	2.84	2.79	2.79
GaAs	4.74	4.74	3.35	3.35	3.35	3.35

Table 6.3 The phase velocities (in the units of $\times 10^3$ ms^{-1}) along different major directions obtained from the velocity curve calculations in different samples.

The velocity curves, power flow angles and electromechanical coupling coefficients in different materials were found. It is important to know the phase velocity and k_t of the sensor materials as well as power flow angle when fabricating an acoustic sensor. Table 6.3 shows the phase velocities (including longitudinal and shear wave) in different directions calculated for different materials. AlN has the highest phase velocities for the longitudinal and shear wave. The second is GaN and the third is ZnO, and velocity is the lowest in GaAs. However, when we consider the k_t, we found that ZnO has the highest value (0.18), the second is AlN (0.14), while the third is GaN (0.095), and the lowest is GaAs (Figure 6.21). These data give us useful information for our future work in fabricating acoustic wave sensors using these materials.

From the velocity (slowness) curves shown above, it is found that the shape of the velocity (slowness) curves depends on the crystal symmetry of the materials. Taking the four materials as examples, in AlN, GaN, and ZnO with a wurtzite symmetry, the shape of the velocity (slowness) curves is circular for both of longitudinal and shears waves. However, in GaAs with a zinc blende symmetry, the shapes of the curves are very different. And also we have tried some other materials with different symmetries, the shapes of the velocity curves are varied and must be treated case by case.

The power flow angle calculation shows that the angle depends on the shape of the slowness curves. i.e., the angle also depends on the symmetry of the material. From the above results, we know that the power flow angles of materials having wurtzite structure are zero both in the longitudinal and shear waves. However, for GaAs material, the power flow angles of the longitudinal and forone of the shear waves is non-zero. Suppose the group velocity (energy) travels along a direction different to its phase velocity, it is necessary to know where the energy is heading in order to place the transducer at the correct position to receive the acoustic energy. These are very important in surface acoustic wave sensor designs in which a pair of interdigital transducers (IDT) is placed opposite to each other. Hence, the power flow angles are also important information necessary for the design of sensor configurations.

CHAPTER SEVEN

CONCLUSIONS AND SUGGESTIONS FOR FUTURE WORK

In the present work, interferometric technique has been used in determining the piezoelectric coefficients of III-V nitrides, namely aluminum nitride (AlN) and composite gallium nitride /aluminum nitride (GaN/AlN) thin films on Si substrates. The interferometer arrangement used in this work was a Mach-Zehnder type heterodyne interferometer.

Two types of samples were used in the measurements. The AlN/Si and GaN/Si were prepared by molecular beam epitaxy (MBE), setup in The Hong Kong Polytechnic University Electronic and Information Engineering Department. Both of the thin films were grown on silicon (111) substrate. The other composite films (GaN/AlN/Si(111) and GaN/AlN/Si(100)) were also prepared by MBE in USA.

From the Rutherford Backscattering Spectrometry (RBS), the cluster sizes and crystal quality of the samples are determined. It is found that the composite sample, GaN/AlN/Si(111), has a better crystal quality than other samples. The in-plane orientation of that sample is GaN $[11\bar{2}0]$ || Si $[\bar{1}11]$ and also there is no angular misorientation between the [0001] GaN and [111] Si direction.

From the X-Ray Diffractometry (XRD), the lattice parameters of all the samples were measured. Furthermore, the phases (cubic and/or hexagonal structure) existed in the samples have been identified. It is very important to identify the phase in the films, since different crystal structure has different piezoelectric coefficient(s). For example, a cubic structure have only one non-zero coefficient, d_{14}, while a hexagonal structure having three non-zero coefficients, named d_{31}, d_{33}, and d_{15}. In the measurement, we found that all the samples have the hexagonal phase except the sample GaN/AlN/Si(111). By using the method reported by Tsuchiya *et al.*, we found that there is 98 % of wurtzite (hexagonal) phase and 2 % of zinc blende (cubic) phase in that sample.

As the samples used in the d_{33} measurement are thin films grown on silicon and some of them are composite films with AlN buffer layers, it is important to investigate the effect of the substrate as well as the buffer layer on the measurement. From the resistivity and dielectric permittivity measurements, we can obtain information of resistivity, dielectric permittivity, and capacitance of the sample. The data can be used in the calculation of potential drops across each layer as a function of frequency in GaN, AlN and the silicon substrate.

The piezoelectric coefficients for AlN and GaN/AlN/Si have been measured by a Mach Zehnder type heterodyne interferometer. The d_{31}, d_{33}, and d_{14} of GaN have also been calculated from the composite film samples taking into account the effect of the AlN buffer layer and the substrate.

When using a laser interferometer to measure the surface vibration, the sample mounting is very important. It is found that bending mode vibrations will occur even at low frequency measurements if the sample is not mounted properly. However, if the sample is rigidly mounted to the holder, the bending effects can be suppressed for low frequency measurements (below 40 kHz). Another method to eliminate the bending effect is to reduce the size of the electrode.

The values of the d_{33} and d_{31} coefficients for AlN are found to be (5.10 ± 0.1) pmV^{-1} and (2.55 ± 0.1) pmV^{-1}, respectively. While the values of the d_{33} and d_{31} coefficients for GaN are found to be (2.60 ± 0.1) pmV^{-1} and (1.30 ± 0.1) pmV^{-1}, respectively. Both values were measured in thin film samples and have corrected for the substrate clamping.

Three programs were written to calculate the phase velocity curves, power flow angles and the electromechanical coupling coefficients in different materials. These are important parameters if we wish to fabricate acoustic sensors using these materials. In the calculation, we found that the AlN have the highest phase velocities in the longitudinal and shear waves compared to GaN, ZnO and GaAs. We also found that the power flow angles of material having hexagonal structure is zero. However, in other crystal symmetry, the power flow angles is not necessary zero. These can give us information for designing different sensor configurations.

In this work, we have measured the piezoelectric coefficients of AlN and the composite GaN/AlN/Si thin films, and the piezoelectric coefficients of GaN is calculated from these results. As the GaN thin film grown directly on a silicon substrate by MBE high conductivity [46], it cannot be used in the piezoelectric measurement in the present study. In the future, we need to use compensation doping during the GaN film growth to yield a film with higher resistivity and then we can directly measure the piezoelectric properties of GaN.

In the group of the III-V nitrides (AlN, GaN, and InN), The physical properties, film growth and applications of AlN and GaN have been widely reported. However, the attention InN received is not as much as the other two. InN has the same wurtzite structure as AlN and GaN and the measurement of piezoelectric coefficients of InN can be an extension of this work.

We have mentioned before, when we used a single beam interferometer to measure the surface vibration, the sample mounting is very important. However, even when the sample is rigidly mounted, the bending effects may still occur at several kHz. In order to measure the piezoelectric properties at a higher frequency, one should use a double beam laser interferometer because the double beam arrangement can measure the displacement induced on the sample surface accurately even if a bending mode vibration has been excited in the sample. Work is in progress in our group in constructing a double beam heterodyne interferometer and the details of this work will be reported in the future.

REFERENCES

[1] W.P. Mason, *Piezoelectric Crystals and their Application to Ultrasonics*, D. Van Nostrand Company, New York (1950).

[2] S. Nakamura, M. Senoh, S. Nagahama, N. Iwasa, T. Yamada, T. Matsushita, H. Kiyoku, Y. Sugimoto, *Jpn. J. Appl. Phys.* Part 2 (letters) 35 1B, L74 (1996)

[3] S. Nakamura, T. Mukai and M. Senoh, *J. Appl. Phys.* 76(12), 8189 (1994).

[4] M. Razeghi and A. Rogalski, *J. Appl. Phys.* 79(10), 7433 (1996).

[5] A. Bykhovski, B. Gelmont and M. Shur, *J. Appl. Phys.* 77(4), 1616 (1995).

[6] R. Gaska, J. Yang, A. Osinsky, A.D. Byhovski and M.S. Shur, *Appl. Phys. Lett.* 71(25), 3673 (1997).

[7] M. Dubois, P. Muralt and L. Sagalowicz, *Ferroelectrics* 224, 243 (1999).

[8] S. Strite and H. Morkoc, "GaN, AlN, and InN: A review", *J. Vac. Sci. Technol.* B 10, 1237 (1992).

[9] S. Muensit, and I.L. Guy, " The piezoelectric coefficient of gallium nitride thin films", *Appl. Phys. Lett.* 59, 1896 (1998).

[10] J.F. Nye, *Physical properties of crystals*, Oxford University Press, Oxford (1976).

[11] T. Ikeda, *Fundamental of Piezoelectricity*, Oxford University Press, New York (1990).

[12] IEEE Standard on Piezoelectricity, ANSI/IEEE Standard 176-1987, The Institute of Electrical and Electronics Engineers, Inc., New York (1988).

[13] D. Royer and V. Kmetik, "Measuremetn of Piezoelectric Constants Using an Optical Heterodyne Interferometer", *Electronics Lett.* 28, 1828 (1992).

[14] J.R. Arthur, "Molecular Beam Epitaxy Workshop 1983", Proc. 5th USA MBE Workshop; *J. Vac. Sci. Technol.* B 2, no. 2 (1984).

[15] G.Y. Robinson, "Molecular Beam Epitaxy Workshop 1985", Proc. 6th USA MBE Workshop; *J. Vac. Sci. Technol.* B 4, no. 2 (1986).

[16] H. Morkoc, "Molecular Beam Epitaxy Workshop 1982", Proc. 4th USA MBE Workshop; *J. Vac. Sci. Technol.* B 1, no. 2 (1983).

[17] M.A. Herman and H. Sitter, "Molecular Beam Epitaxy", Springer-Verlag Berlin Heidelberg, New York (1996).

[18] Michihiro Miyauchi, Yukari Ishikawa, and Noriyoshi Shibata, "Growth of aluminum nitride films on silicon by electron-cyclotron-resonance-assisted molecular beam epitaxy", *Jpn. J. Appl. Phys.* 31, L 1714 (1992).

[19] H. Amano, N. Sawaki, I. Akasaki, and Y. Toyoda, "Metalorganic vapor phase epitaxial growth of a high quality GaN film using an AlN buffer layer", *Appl. Phys. Lett.* 48, 353 (1986).

[20] Y. Morimoto, K. Uchiho and S. Ushio, "Vapor phase epitaxial growth of GaN on GaAs, GaP, Si, and sapphire substrates from GaBr3 and NH3", *J. Electrochem. Soc.* 120, 1783 (1973).

[21] T.D. Moustakas, T. Lei and R.J. Molnar, "Growth of GaN by ECR-assisted MBE", *Physica* B 185, 36 (1993).

[22] C. Richard Brundle, Charles A. Evans, Jr., and Shaun Wilson, *Encyclopedia of Materials Characterization*, Butterworth-Heinemann (1992).

[23] L.C. Feldman, J.W. Mayer, and S.T. Picraus. *Materials Analysis by Ion Channeling*. Academic Press, New York (1982).

[24] D.V. Morgan. *Channeling*. John Wiley & Sons, London (1973).

[25] V.W.L. Chin, T.L. Tansley, and T. Osotchan, "Electron mobilities in gallium, indium, and aluminum nitrides", *J. Appl. Phys.* 75, 7365 (1994).

[26] B. D. Cullity, *Elements of X-ray Diffraction*, ed. M. Cohen, Addison-Wesley (1956).

[27] H. Tsuchiya, K. Sunaba, S. Yonemura, T. Suemasu, and F. Hasegawa, "Cubic dominant GaN growth on (001) GaAs substrates by hydride vapor phase epitaxy", *Jpn. J. Appl. Phys.* 36, L1 (1997).

[28] David R. Lide, *CRC Handbook of Chemistry and Physics*, 74th edition, Chemical Rubber Publishing Company, Florida (1993/1994).

[29] D. Royer, and E. Dieulesaint, "Optical probing of the mechanical impulse response of a transducer", *Appl. Phys. Lett.* 49, 1056 (1986).

[30] S. Muensit, B. Zhou, D.JJ. Wilson, I.L. Guy and T.L. Tansley, "Study of the Piezoelectric Effect in Gallium Nitride Films Using A Modified Michelson Interferometer", Proc. of the conference on Optoelectronics and Microelectronic Materials and Devices 1996.

[31] Z. Zhao, H.L.W. Chan, and C.L. Choy, "Determination of the piezoelectric coefficient d_{33} at high frequency by laser interferometry", *Ferroelectrics*, 195, 35 (1997).

[32] W.Y. Pan, and L.E. Cross, "A sensitive double beam laser interferometer for studying high-frequency piezoelectric and electrostrictive strains", *Rev. Sci. Instrum.* 60, 2701 (1989).

[33] Q.M. Zhang, W.Y. Pan, and L.E. Cross, "Laser interferometer for the study of piezoelectric and electrostrictive strains", *J. Appl. Phys.* 63, 2492 (1987).

[34] A.L. Kholkin, Ch. Wutchrich, D.V. Taylor, and N. Setter, "Interferometric measurements of electric field-induced displacements on piezoelectric thin films", *Rev. Sci. Instrum.* 67, 1936 (1996).

[35] M.S. Shur, and M.A. Khan, "GaN/AlGaN Heterostructure Devices: Photodetectors and Field-Effect Transistors", *Mat. Res. Bull.*, 22 (2), 44 (1997).

[36] H.P. Maruska, and J.J. Tietjen, "The preparation and properties of vapor-deposited single crystal", *Appl. Phys. Lett.*, 59, 327 (1969).

[37] A.D. Bykhovski, V.V. Kaminski, M..S. Shur, Q.C. Chen and M.A. Khan, " Piezoresistive effect in wurtzite n-type GaN" *Appl. Phys. Lett.*, 68, 818 (1996).

[38] S.N. Mohammad, A.A. Salvador, and H. Morkoç, "Emerging gallium nitride based devices", *Proc. of the IEEE*, 83, 1306 (1995).

[39] F. Bernardini, and V. Fiorentini, and D. Vanderbilt "Spontaneous polarization and piezoelectric constants of III-V nitrides", *Phys. Rev.* B 56, R10024 (1997).

[40] M. Mizuta, S. Fujieda, Y. Matsumoto, and T. Kawamura, *Jpn. J. Appl. Phys.* 25, L945 (1986).

[41] H. Okumura, S. Misawa, and S. Yoshida, "Epitaxial growth of cubic and hexagonal GaN on GaAs by gas-source molecular-beam epitaxy", *Appl. Phys. Lett.* 59, 1058 (1991).

[42] M.J. Paisley, Z. Sitar, J.B. Posthill, and R.F. Davis, *J. Vac. Sci. Technol.* A7, 701 (1989).

[43] T. Lei, M. Fanciulli, R.J. Molnar, T.D. Moustakas, R.J. Graham, and J. Scanlon, "Epitaxial growth of zinc blende and wurtzitic gallium nitride thin films on (001) silicon", *Appl. Phys. Lett.* 59, 944 (1991)

[44] T. Lei, T.D. Moustakas, R.J. Graham, Y. He and S.J. Berkowitz, "Epitaxial growth and characterization of zinc-blende gallium nitride on (001) silicon", *J. Appl. Phys.* 71, 4933 (1992).

[45] D.K. Gaskill, N. Bottka and M.C. Lin, "Growth of GaN films using trimethylgallium and hydrazine ", *Appl. Phys. Lett.* 48, 1449 (1986).

[46] S. Strite, M.E. Lin, and H. Morkoç, "Progress and prospects for GaN and the III-V nitride semiconductors", *Thin Solid Films* 231, 197 (1993).

[47] J. L. Birman, "Theory of the piezoelectric effect in the zincblende structure", *Phys. Rev.* 111, 1510 (1958).

[48] D. Berlincourt, H. Jaffe, and L.R. Shiozawa, "Electroelastic properties of the sulfides, selenides, and tellurides of zinc and cadmium", *Phys. Rev.* 129, 1009 (1963).

[49] J.F. Li, P. Moses and D. Viehland, "Simple, high-resolution interferometer for the measurement of frequency-dependent complex piezoelectric responses in ferroelectric ceramics", *Rev. Sci. Instrum.* 66, 215 (1995).

[50] S.M. Sze, *VLSI Technology*, McGraw-Hill International Editions, New York (1988).

[51] A.R. Hutson, "Piezoelectric devices utilizing AlN", *U.S. Patent*, 3090876 (May 21, 1963).

[52] K. Tsubouchi, K. Sugai and N. Mikoshiba, *Proc. IEEE Ultrason. Symp.* 375 (1981).

[53] L.E. McNeil, M. Grimsditch and R.H. French, *J. Am. Ceram. Soc.* 76, 1132 (1993).

[54] E. Ruiz, S. Alvarez and P. Alemany, Phys. Rev. B 49, 5188 (1994).

[55] A.F. Wright, *J. Appl. Phys.* 82, 2833 (1997).

[56] A.U. Sheleg and V.A. Savastenko, Izv. Akad. Nauk. SSSR, Neorg. Mater. 15, 1598 (1979).

[57] A. Polian, M. Grimsditch and I. Grzegory, *J. Appl. Phys.* 79, 3343 (1996).

[58] Y. Takagi, M. Ahart, T. Azuhata, T. Sota, K. Suzuki and S. Nakamura, *Physica B* 219 & 220, 547 (1996).

[59] Joel F. RosenBaum, *Bulk Acoustic Wave Theory and Devices*, Artech House, Boston, London (1988).

[60] R.B. Schwarz, K. Khachaturyan, and E.R. Weber, "Elastic moduli of gallium nitride", *Appl. Phys. Lett.* 70, 1122 (1997).

[61] B.A. Auld, *Acoustic Fields and Waves in Solids Voume I*, Krieger Publishing Company, Malabas, Florida (1990).

[62] S. Muensit, *PhD Thesis*, Macquarie University, Australia (1998).

[63] G. John Gualtieri, A. John Kosinski, and Arthur Ballato, "Piezoelectric materials for acoustic wave applications", *IEEE Trans. on Ultrason., Ferroel., and Freq. Control* 41, 53 (1994).

[64] A.S. Barker, Jr. and M. Ilegems, "Infrared lattice vibrations and free-electron dispersion in GaN", *Phys. Rev.* B 7, 743 (1973).

[65] M. Born and E. Wolf, *Priciples of Optics*, Pergamon, London (1975).

APPENDIX

Appendix I: The Program for Calculation of Potential Drop

```
program Potential_drop;
        uses
            dos, crt, ucompl;
        var
           R1, R2, R3, C1, C2, C3, I1, I2, I3,
           ANSWER1, ANSWER2, ANSWER3            :REAL;
           COMP1, COMP2, COMP3, DC1, DC2, DC3, DENORM,
           ANS1, ANS2, ANS3:COMPLEX;
           F, G:LONGINT;
           ofile:text;
        CONST
                C_1  :COMPLEX=(RE:1; IM:0)   ;
BEGIN
     ASSIGN(OFILE,'R2.DAT');
     REWRITE(OFILE);
     READLN(R1, C1);
     READLN(R2, C2);
     READLN(R3, C3);
{r2:=}
     FOR G:= 1 TO 1500
     DO
     BEGIN
     F:=G*1000;
     I1:=2*PI*F*C1;
     I2:=2*PI*F*C2;
     I3:=2*PI*F*C3;

     COMPL(COMP1,1/R1,I1);
     COMPL(COMP2,1/R2,I2);
     COMPL(COMP3,1/R3,I3);

     CDIV(DC1,C_1,COMP1);
     CDIV(DC2,C_1,COMP2);
     CDIV(DC3,C_1,COMP3);

     CADD(DENORM,DC1,DC2);
     CADD(DENORM,DENORM,DC3);
     CDIV(ANS1,DC1,DENORM);
     CDIV(ANS2,DC2,DENORM);
     CDIV(ANS3,DC3,DENORM);
     ANSWER1:=CABS(ANS1);
     ANSWER2:=CABS(ANS2);
     ANSWER3:=CABS(ANS3);
     WRITELN(OFILE,F,' ',ANSWER1,' ',ANSWER2,' ',ANSWER3);
     WRITELN(ANSWER1);
     WRITELN(ANSWER2);
     WRITELN(ANSWER3);
     WRITELN(F);
     END;
     CLOSE(OFILE);
END.
```

Appendix II: The Program for Velocity Curve Calculation

```
PROGRAM Christoffel;

USES    crt, rgsn, graph, dos;

var     T33, R1 : array[1..3,1..3] of extended;
        L13, SS : array[1..1 ,1..3] of extended;
        CL63, L63 : array[1..6,1..3] of extended;
        L36 : array[1..3,1..6] of extended;
        ROOT, AA, BB, VEL : array[1..3] of extended;
        L31, EL31      :array[1..3,1..1] of extended;
        LE16 :array[1..1,1..6] of extended;
        EL61 :array[1..6,1..1] of extended;
        CC66, CS66 :array[1..6,1..6] of extended;
        x1, x2, y1, y2: real;

        an, bn, dot, dens, dens1, xx,
        theta, p, q, r, a, b, x, y: extended;
        a2, a3, r2, p1, sp, z, d: extended;
        i, n, o, l, m: integer;
        ofile:text;

const   C66: array[1..6,1..6] of extended=
        ((410.5,148.5,98.9,0,0,0), (148.5,410.5,98.9,0,0,0),
            (98.9,98.9,388.5,0,0,0),  (0,0,0,124.6,0,0),
            (0,0,0,0,124.6,0), (0,0,0,0,0,131));
            {C66 is the Stiffness matrix}
         E36: array[1..3,1..6] of extended=
        ((0,0,0,0,-0.45,0), (0,0,0,-0.45,0,0),
            (-0.92,-0.92,1.48,0,0,0));
            {E36 is piezoelectric stress matrix}
              EP33: array[1..3,1..3] of extended=
              ((9,0,0), (0,9,0), (0,0,11));
            {EP36 is the dielectric matrix}

begin
   assign(ofile,'aln_vc2.dat');
   rewrite(ofile);
   for m:=1 to 6 do begin
      for l:=1 to 3 do begin
         L36[l,m]:=0;
      end;
   end;

   DENS:= 3.23;
   write('X AXIS IS:');
   readln(AA[1], AA[2], AA[3]);
   write('Y AXIS IS:');
   readln(BB[1], BB[2], BB[3]);

   AN:= SQRT(AA[1]*AA[1]+ AA[2]*AA[2] + AA[3]*AA[3]);
   BN:= SQRT(BB[1]*BB[1]+ BB[2]*BB[2] + BB[3]*BB[3]);
   DOT := AA[1] * BB[1] + AA[2] * BB[2] + AA[3] * BB[3];

   IF ABS(DOT) > 0.001 THEN BEGIN
      writeln('AXES ARE NOT ORTHOGONAL');
      exit;
```

```
end;
R1[1, 1]:= AA[1] / AN;
R1[1, 2]:= AA[2] / AN;
R1[1, 3]:= AA[3] / AN;
R1[2, 1]:= BB[1] / BN;
R1[2, 2]:= BB[2] / BN;
R1[2, 3]:= BB[3] / BN;
R1[3, 1]:= R1[1, 2] * R1[2, 3] - R1[2, 2] * R1[1, 3];
R1[3, 2]:= R1[2, 1] * R1[1, 3] - R1[2, 3] * R1[1, 1];
R1[3, 3]:= R1[1, 1] * R1[2, 2] - R1[2, 1] * R1[1, 2];

XX:= 8;
initrgraph;
cls; offset (3.0, 3.0);

x1:=-12;
x2:=12;
y1:=-12;
y2:=12;
init (x1, x2, 18.0,0,y1, y2, 18.0, 0);

sym(x1,0,0);
lin(x2,0,0);
sym(0,y1,0);
lin(0,y2,0);
xytext('Y(m/s) X10E3',3);
xytext('X(m/s) X10E3',0);
xytext('compare the stiffened and unstiffened velocity curves',2);

FOR N:= 1 TO 3 do
begin
  for i:=0 to 360 do begin
     theta:=i*pi/180;
     SS[1, 1]:= COS(THETA);
     SS[1, 2]:= SIN(THETA);
     SS[1, 3]:= 0;

     for m:=1 to 3 do begin
        L13[1,m]:=0;
        for l:=1 to 3 do begin
           L13[1,m]:=L13[1,m]+SS[1,l]*R1[l,m];
        end;
     end;

     for m:=1 to 3 do begin
        for l:=1 to 6 do begin
           L36[m,l]:=0;
        end;
     end;

     L36[1, 1]:= L13[1, 1];
     L36[2, 2]:= L13[1, 2];
     L36[3, 3]:= L13[1, 3];
     L36[1, 5]:= L13[1, 3];
     L36[1, 6]:= L13[1, 2];
     L36[2, 4]:= L13[1, 3];
     L36[2, 6]:= L13[1, 1];
     L36[3, 4]:= L13[1, 2];
     L36[3, 5]:= L13[1, 1];
```

```
     for m:=1 to 3 do begin
        for l:=1 to 6 do begin
           L63[l,m]:=L36[m,l];
        end;
     end;
{COPIED}
        for m:=1 to 6 do begin
        for l:=1 to 3 do begin
           CL63[m,l]:=0;
           for o:=1 to 6 do begin
               CL63[m,l]:=CL63[m,l]+C66[m,o]*L63[o,l];
           end;
        end;
     end;

     for m:=1 to 3 do begin
        for l:=1 to 3 do begin
           T33[m,l]:=0;
           for o:=1 to 6 do begin
              T33[m,l]:=T33[m,l]+L36[m,o]*CL63[o,l];
           end;
        end;
     end;

     P:= -(T33[1, 1] + T33[2, 2] + T33[3, 3]);
     Q:= T33[1, 1] * T33[3, 3] + T33[1, 1] * T33[2, 2] + T33[2, 2]
   * T33[3,3];
     Q:= Q - (T33[2, 1]*T33[2, 1] + T33[2, 3]*T33[2, 3] + T33[3,
   1]*T33[3,1]);
     R:= T33[1, 1] * T33[3, 2]*T33[3, 2] + T33[3, 3]* T33[1,
   2]*T33[1, 2] + T33[2, 2] * T33[1, 3]*T33[1, 3];
     R:= R - T33[1, 1] * T33[2, 2] * T33[3, 3] - 2 * T33[1, 2] *
   T33[1, 3] * T33[2, 3];

     A:= (3 * Q - P * P)/3;
     B:= (2 * P * P * P - 9 * P * Q + 27 * R) / 27;
     X:= 0;

     if B <> 0 THEN begin
        A2:= B * B / 4 + A * A * A / 27;
        IF A2 > 0 THEN A2:= 0;
        A2:= -A2;
        D:= SQRT(A2);
        A3:= -B / 2;
        R2:= SQRT(A3 * A3 + D * D);
        IF A3 >= 0 THEN P1:= ARCTAN(D / A3)
                   else P1:= (PI) -ARCTAN(D / A3);
        R2:= EXP(LN(R2) / 3);
        P1:= P1 / 3;
        X:= R2 * COS(P1);
        X:= X * 2;
     end;

     ROOT[1]:= X - P / 3;
     Z:= (P + ROOT[1]) / 2;
     SP:= Z * Z + R / ROOT[1];
     SP:= ABS(SP);
     ROOT[2]:= -Z + SQRT(SP);
```

```
        ROOT[3]:= -Z - SQRT(SP);

        VEL[1]:= sqrt(ROOT[1] / DENS);
        VEL[2]:= sqrt(ROOT[2] / DENS);
        VEL[3]:= sqrt(ROOT[3] / DENS);
        X:= (VEL[N] * COS(THETA));
        Y:= (VEL[N] * SIN(THETA));
        writeln(ofile,x,' ',y);
        if N=1 then color:=yellow;
        if n=2 then color:=lightblue;
        if n=3 then color:=white;
        sym (x,y,0);

        for l:=1 to 3 do begin      {TRANSPOSE OF L13}
            L31[l,1]:=L13[1,l];
        end;

        for m:=1 to 3 do begin      {EL31 = EP33:L31}
           for l:=1 to 1 do begin
              EL31[m,l]:=0;
              for o:=1 to 3 do begin
                  EL31[m,l]:=EL31[m,l]+EP33[m,o]*L31[o,l];
              end;
           end;
        end;

DENS1:=EL31[1,1]*L13[1,1]+EL31[2,1]*L13[1,2]+EL31[3,1]*L13[1,3];
        DENS1:=DENS1*0.008854;

        for:=1 to 1 do begin        {LE16 = L31xE36}
           for l:=1 to 6 do begin
              LE16[m,l]:=0;
              for o:=1 to 3 do begin
                  LE16[m,l]:=LE16[m,l]+L13[m,o]*E36[o,l];
              end;
           end;
        end;

        for l:=1 to 6 do begin
            EL61[l,1]:=LE16[1,l];
        end;

        for m:=1 to 6 do begin      {CC66 = EL61xLE16}
           for l:=1 to 6 do begin
              CC66[m,l]:=0;
              for o:=1 to 1 do begin
                  CC66[m,l]:=CC66[m,l]+EL61[m,o]*LE16[o,l];
              end;
           end;
        end;

        DENS1:=1/DENS1;

        for m:=1 to 6 do begin
           for l:=1 to 6 do begin
              CC66[m,l]:=CC66[m,l]*DENS1;
           end;
        end;
```

```
         for m:=1 to 6 do begin      {CS66 = C66 + CC66}
            for l:=1 to 6 do begin
               CS66[m,l]:=C66[m,l]+CC66[m,l];
            end;
         end;

 {NEW PART END}
         L36[1, 1]:= L13[1, 1];
         L36[2, 2]:= L13[1, 2];
         L36[3, 3]:= L13[1, 3];
         L36[1, 5]:= L13[1, 3];
         L36[1, 6]:= L13[1, 2];
         L36[2, 4]:= L13[1, 3];
         L36[2, 6]:= L13[1, 1];
         L36[3, 4]:= L13[1, 2];
         L36[3, 5]:= L13[1, 1];

         for m:=1 to 3 do begin
            for l:=1 to 6 do begin
               L63[l,m]:=L36[m,l];
            end;
         end;

        {COPY}
         for m:=1 to 6 do begin
            for l:=1 to 3 do begin
               CL63[m,l]:=0;
               for o:=1 to 6 do begin
                   CL63[m,l]:=CL63[m,l]+CS66[m,o]*L63[o,l];
                   { CHANGE C66 INTO CS66 TO FIND THE DIFFERENT }
               end;
            end;
         end;
         for m:=1 to 3 do begin
            for l:=1 to 3 do begin
               T33[m,l]:=0;
               for o:=1 to 6 do begin
                  T33[m,l]:=T33[m,l]+L36[m,o]*CL63[o,l];
               end;
            end;
         end;

         P:= -(T33[1, 1] + T33[2, 2] + T33[3, 3]);
         Q:= T33[1, 1] * T33[3, 3] + T33[1, 1] * T33[2, 2] + T33[2, 2]
* T33[3,3];
         Q:= Q - (T33[2, 1]*T33[2, 1] + T33[2, 3]*T33[2, 3] + T33[3,
1]*T33[3,1]);
         R:= T33[1, 1] * T33[3, 2]*T33[3, 2] + T33[3, 3]* T33[1,
2]*T33[1, 2] + T33[2, 2] * T33[1, 3]*T33[1, 3];
         R:= R - T33[1, 1] * T33[2, 2] * T33[3, 3] - 2 * T33[1, 2] *
T33[1, 3] * T33[2, 3];

         A:= (3 * Q - P * P)/3;
         B:= (2 * P * P * P - 9 * P * Q + 27 * R) / 27;
         X:= 0;

         if B <> 0 THEN begin
            A2:= B * B / 4 + A * A * A / 27;
            IF A2 > 0 THEN A2:= 0;
```

```
            A2:= -A2;
            D:= SQRT(A2);
            A3:= -B / 2;
            R2:= SQRT(A3 * A3 + D * D);
            IF A3 >= 0 THEN P1:= ARCTAN(D / A3)
                       else P1:= (PI) -ARCTAN(D / A3);
            R2:= EXP(LN(R2) / 3);
            P1:= P1 / 3;
            X:= R2 * COS(P1);
            X:= X * 2;
         end;

         ROOT[1]:= X - P / 3;
         Z:= (P + ROOT[1]) / 2;
         SP:= Z * Z + R / ROOT[1];
         SP:= ABS(SP);
         ROOT[2]:= -Z + SQRT(SP);
         ROOT[3]:= -Z - SQRT(SP);

         VEL[1]:= sqrt(ROOT[1] / DENS);
         VEL[2]:= sqrt(ROOT[2] / DENS);
         VEL[3]:= sqrt(ROOT[3] / DENS);
         X:= (VEL[N] * COS(THETA));
         Y:= (VEL[N] * SIN(THETA));
         writeln(ofile,x,'          ',y);
         if N=1 then color:=GREEN;
         if n=2 then color:=RED;
         if n=3 then color:=lightgreen;
         sym (x,y,0);
      end;
    end;
  {COPY}

    color:=WHITE;
    gltext('UNSTIFFENED',18.5,10);
    color:=yellow;
    gltext('Longitud',18.5,11);
    color:=lightblue;
    gltext('Shear',18.5,12);
    color:=white;
    gltext('Shear',18.5,13);

    color:=WHITE;
    gltext('STIFFENED',18.5,16);
    color:=green;
    gltext('Longitud',18.5,17);
    color:=red;
    gltext('Shear',18.5,18);
    color:=lightgreen;
    gltext('Shear',18.5,19);

    repeat until keypressed;
    closegraph;
    close(ofile);
END.
```

Appendix III: The Program for Power Flow Angle Calculation

```
PROGRAM PFA;

USES    crt, rgsn, graph, dos;

var     T33, R1 : array[1..3,1..3] of extended;
        L13, SS : array[1..1 ,1..3] of extended;
        CL63, L63 : array[1..6,1..3] of extended;
        L36 : array[1..3,1..6] of extended;
        ROOT, AA, BB, VEL, V : array[1..3] of extended;
        x1, x2, y1, y2: real;

        an, bn, dot, dens, xx, theta, p, q, r, a, b, x, y: extended;
        a2, a3, r2, p1, sp, z, d:
extended;
        i, n, o, l, m:
integer;
        AA1, BB1, NN1, R4, R5, DT, PSI :EXTENDED;
        ofile:text;

const   C66: array[1..6,1..6] of extended=
        ((141,62.5,62.5,0,0,0), (62.5,141,62.5,0,0,0),
(62.5,62.5,141,0,0,0),
         (0,0,0,70.5,0,0), (0,0,0,0,70.5,0), (0,0,0,0,0,70.5));



begin
   assign(ofile,'pfa.dat');
   rewrite(ofile);

   for m:=1 to 6 do begin
      for l:=1 to 3 do begin
         L36[l,m]:=0;
      end;
   end;

   DENS:= 4.3;
   write('X AXIS IS:');
   readln(AA[1], AA[2], AA[3]);
   write('Y AXIS IS:');
   readln(BB[1], BB[2], BB[3]);

   AN:= SQRT(AA[1]*AA[1]+ AA[2]*AA[2] + AA[3]*AA[3]);
   BN:= SQRT(BB[1]*BB[1]+ BB[2]*BB[2] + BB[3]*BB[3]);
   DOT := AA[1] * BB[1] + AA[2] * BB[2] + AA[3] * BB[3];

   IF ABS(DOT) > 0.001 THEN BEGIN
      writeln('AXES ARE NOT ORTHOGONAL');
      exit;
   end;

   R1[1, 1]:= AA[1] / AN;
   R1[1, 2]:= AA[2] / AN;
   R1[1, 3]:= AA[3] / AN;
   R1[2, 1]:= BB[1] / BN;
   R1[2, 2]:= BB[2] / BN;
   R1[2, 3]:= BB[3] / BN;
```

```
R1[3, 1]:= R1[1, 2] * R1[2, 3] - R1[2, 2] * R1[1, 3];
R1[3, 2]:= R1[2, 1] * R1[1, 3] - R1[2, 3] * R1[1, 1];
R1[3, 3]:= R1[1, 1] * R1[2, 2] - R1[2, 1] * R1[1, 2];
XX:= 8;
initrgraph;
cls; offset (2.0, 2.0);

x1:=-0;
x2:=180;
y1:=-0;
y2:=40;

init (x1, x2, 18.0,         0,          y1, y2, 18.0, 0);
sym(x1,0,0);
lin(x2,0,0);
sym(0,y1,0);
lin(0,y2,0);

FOR N:= 1 TO 3 do begin
if n=1 then color:=YELLOW;
if n=2 then color:=lightblue;
if n=3 then color:=white;

  for i:=0 to 180{360} do begin
     theta:=i*pi/180;
     SS[1, 1]:= COS(THETA);
     SS[1, 2]:= SIN(THETA);
     SS[1, 3]:= 0;

     for m:=1 to 3 do begin
        L13[1,m]:=0;
        for l:=1 to 3 do begin
           L13[1,m]:=L13[1,m]+SS[1,l]*R1[l,m];
        end;
     end;

     for m:=1 to 3 do begin
        for l:=1 to 6 do begin
           L36[m,l]:=0;
        end;
     end;

     L36[1, 1]:= L13[1, 1];
     L36[2, 2]:= L13[1, 2];
     L36[3, 3]:= L13[1, 3];
     L36[1, 5]:= L13[1, 3];
     L36[1, 6]:= L13[1, 2];
     L36[2, 4]:= L13[1, 3];
     L36[2, 6]:= L13[1, 1];
     L36[3, 4]:= L13[1, 2];
     L36[3, 5]:= L13[1, 1];

     for m:=1 to 3 do begin
        for l:=1 to 6 do begin
           L63[l,m]:=L36[m,l];
        end;
     end;

     for m:=1 to 6 do begin
```

```
        for l:=1 to 3 do begin
          CL63[m,l]:=0;
          for o:=1 to 6 do begin
             CL63[m,l]:=CL63[m,l]+C66[m,o]*L63[o,l];
          end;
        end;
      end;

      for m:=1 to 3 do begin
        for l:=1 to 3 do begin
          T33[m,l]:=0;
          for o:=1 to 6 do begin
            T33[m,l]:=T33[m,l]+L36[m,o]*CL63[o,l];
          end;
        end;
      end;

      P:= -(T33[1, 1] + T33[2, 2] + T33[3, 3]);
      Q:= T33[1, 1] * T33[3, 3] + T33[1, 1] * T33[2, 2] + T33[2, 2]
* T33[3, 3];
      Q:= Q - (T33[2, 1]*T33[2, 1] + T33[2, 3]*T33[2, 3] + T33[3,
1]*T33[3, 1]);
      R:= T33[1, 1] * T33[3, 2]*T33[3, 2] + T33[3, 3]* T33[1,
2]*T33[1, 2] + T33[2, 2] * T33[1, 3]*T33[1, 3];
      R:= R - T33[1, 1] * T33[2, 2] * T33[3, 3] - 2 * T33[1, 2] *
T33[1, 3] * T33[2, 3];


      A:= (3 * Q - P * P)/3;
      B:= (2 * P * P * P - 9 * P * Q + 27 * R) / 27;
      X:= 0;

      if B <> 0 THEN begin
        A2:= B * B / 4 + A * A * A / 27;
        IF A2 > 0 THEN A2:= 0;
        A2:= -A2;
        D:= SQRT(A2);
        A3:= -B / 2;
        R2:= SQRT(A3 * A3 + D * D);
        IF A3 >= 0 THEN P1:= ARCTAN(D / A3)
                   else P1:= (PI) -ARCTAN(D / A3);
        R2:= EXP(LN(R2) / 3);
        P1:= P1 / 3;
        X:= R2 * COS(P1);
        X:= X * 2;
      end;

      ROOT[1]:= X - P / 3;
      Z:= (P + ROOT[1]) / 2;
      SP:= Z * Z + R / ROOT[1];
      SP:= ABS(SP);
      ROOT[2]:= -Z + SQRT(SP);
      ROOT[3]:= -Z - SQRT(SP);

      VEL[1]:= sqrt(ROOT[1] / DENS);
      VEL[2]:= sqrt(ROOT[2] / DENS);
      VEL[3]:= sqrt(ROOT[3] / DENS);

      if theta=0 then begin
```

```
            SYM(0,0,0);
            V[1]:=vel[1];
            V[2]:=VEL[2];
            V[3]:=VEL[3];
            R4:=SS[1,1];
            R5:=SS[1,2];
         end

         ELSE
         BEGIN
              AA1:=(SS[1,1]/VEL[N])-(R4/V[N]);
              BB1:=(SS[1,2]/VEL[N])-(R5/V[N]);
              NN1:=SQRT((AA1*AA1+BB1*BB1));
              AA1:=AA1/NN1;
              BB1:=BB1/NN1;

              DT:=AA1*SS[1,1]+BB1*SS[1,2];
              PSI:=arctan(SQRT(1/(DT*DT)-1));
              PSI:=ABS(PSI);
              PSI:=PSI*180/PI;
              PSI:=PSI-90;
              PSI:=ABS(PSI);


              IF PSI<0.51 THEN SYM(THETA*180/PI,0,0)
                   ELSE SYM(THETA*180/PI,PSI,0);{}

              writeln(ofile,THETA*180/PI,' ',PSI);
              V[1]:=vel[1];
              V[2]:=VEL[2];
              V[3]:=VEL[3];
              R4:=SS[1,1];
              R5:=SS[1,2];

      end;
    SYM(0,0,0);
    end;
    end;
    color:=yellow;
    gltext('Longitudinal',18.5,17);
    color:=lightblue;
    gltext('Shear',18.5,18);
    color:=white;
    gltext('Shear',18.5,19);

    repeat until keypressed;
    closegraph;
    CLOSE(OFILE);

END.
```

Appendix IV: The Program for Electromechanical Coupling Coefficient Calculation

```
PROGRAM EMCC;

USES    crt, rgsn, graph, dos;

var     T33, R1 : array[1..3,1..3] of extended;
        L13, SS : array[1..1 ,1..3] of extended;
        CL63, L63 : array[1..6,1..3] of extended;
        L36 : array[1..3,1..6] of extended;
        ROOT, AA, BB, VEL, SVEL : array[1..3] of extended;
        L31, EL31      :array[1..3,1..1] of extended;
        LE16 :array[1..1,1..6] of extended;
        EL61 :array[1..6,1..1] of extended;
        CC66, CS66 :array[1..6,1..6] of extended;
        x1, x2, y1, y2: real;

        an, bn, dot, den, dens, xx, theta, p, q, r, a, b, x, y:
extended;
        STIFF, UNSTIFF, KK, KT,
        ktkt, delta,C, a2, a3, r2, p1, sp, z, d, SX, SY, UX, UY:
extended;
        i, n, o, l, m:
integer;
        ofile:text;
const   C66: array[1..6,1..6] of extended=
        ((410.5,148.5,98.9,0,0,0), (148.5,410.5,98.9,0,0,0),
(98.9,98.9,388.5,0,0,0),
         (0,0,0,124.6,0,0), (0,0,0,0,124.6,0), (0,0,0,0,0,131));

         E36: array[1..3,1..6] of extended=
        ((0,0,0,0,-0.45,0), (0,0,0,-0.45,0,0), (-0.92,-
0.92,1.48,0,0,0));

        EP33: array[1..3,1..3] of extended=
        ((9,0,0), (0,9,0), (0,0,11));

begin
   assign(ofile,'AlN_st.dat');
   rewrite(ofile);

   for m:=1 to 6 do begin
      for l:=1 to 3 do begin
         L36[l,m]:=0;
      end;
   end;

   DENS:= 3.23;
   write('X AXIS IS:');
   readln(AA[1], AA[2], AA[3]);
   write('Y AXIS IS:');
   readln(BB[1], BB[2], BB[3]);

   AN:= SQRT(AA[1]*AA[1]+ AA[2]*AA[2] + AA[3]*AA[3]);
   BN:= SQRT(BB[1]*BB[1]+ BB[2]*BB[2] + BB[3]*BB[3]);
   DOT := AA[1] * BB[1] + AA[2] * BB[2] + AA[3] * BB[3];
```

```
IF ABS(DOT) > 0.001 THEN BEGIN
   writeln('AXES ARE NOT ORTHOGONAL');
   exit;
end;

R1[1, 1]:= AA[1] / AN;
R1[1, 2]:= AA[2] / AN;
R1[1, 3]:= AA[3] / AN;
R1[2, 1]:= BB[1] / BN;
R1[2, 2]:= BB[2] / BN;
R1[2, 3]:= BB[3] / BN;
R1[3, 1]:= R1[1, 2] * R1[2, 3] - R1[2, 2] * R1[1, 3];
R1[3, 2]:= R1[2, 1] * R1[1, 3] - R1[2, 3] * R1[1, 1];
R1[3, 3]:= R1[1, 1] * R1[2, 2] - R1[2, 1] * R1[1, 2];

XX:= 8;
initrgraph;
cls; offset (3.0, 3.0);

x1:=0;
x2:=360;
y1:=0;
y2:=0.8;

init (x1, x2, 18.0,         0,         y1, y2, 18.0, 0);

sym(x1,0,0);
lin(x2,0,0);
sym(0,y1,0);
lin(0,y2,0);
xytext('Theta',0);
xytext('Electromechanical coupling constant, kt',3);
xytext('The Kt at the plane you chosen for AlN',2);

FOR N:= 1 TO 3 do
begin
  for i:=0 to 360 do begin
     theta:=i*pi/180;
     SS[1, 1]:= COS(THETA);
     SS[1, 2]:= SIN(THETA);
     SS[1, 3]:= 0;

     for m:=1 to 3 do begin
        L13[1,m]:=0;
        for l:=1 to 3 do begin
           L13[1,m]:=L13[1,m]+SS[1,l]*R1[l,m];
        end;
     end;

     for m:=1 to 3 do begin
        for l:=1 to 6 do begin
           L36[m,l]:=0;
        end;
     end;

     L36[1, 1]:= L13[1, 1];
     L36[2, 2]:= L13[1, 2];
     L36[3, 3]:= L13[1, 3];
```

```
         L36[1, 5]:= L13[1, 3];
         L36[1, 6]:= L13[1, 2];
         L36[2, 4]:= L13[1, 3];
         L36[2, 6]:= L13[1, 1];
         L36[3, 4]:= L13[1, 2];
         L36[3, 5]:= L13[1, 1];

         for m:=1 to 3 do begin
            for l:=1 to 6 do begin
               L63[l,m]:=L36[m,l];
            end;
         end;
    {COPIED}
            for m:=1 to 6 do begin
            for l:=1 to 3 do begin
               CL63[m,l]:=0;
               for o:=1 to 6 do begin
                   CL63[m,l]:=CL63[m,l]+C66[m,o]*L63[o,l];
               end;
            end;
         end;

         for m:=1 to 3 do begin
            for l:=1 to 3 do begin
               T33[m,l]:=0;
               for o:=1 to 6 do begin
                  T33[m,l]:=T33[m,l]+L36[m,o]*CL63[o,l];
               end;
            end;
         end;

         P:= -(T33[1, 1] + T33[2, 2] + T33[3, 3]);
         Q:= T33[1, 1] * T33[3, 3] + T33[1, 1] * T33[2, 2] + T33[2, 2]
* T33[3, 3];
         Q:= Q - (T33[2, 1]*T33[2, 1] + T33[2, 3]*T33[2, 3] + T33[3,
1]*T33[3, 1]);
         R:= T33[1, 1] * T33[3, 2]*T33[3, 2] + T33[3, 3]* T33[1,
2]*T33[1, 2] + T33[2, 2] * T33[1, 3]*T33[1, 3];
         R:= R - T33[1, 1] * T33[2, 2] * T33[3, 3] - 2 * T33[1, 2] *
T33[1, 3] * T33[2, 3];


         A:= (3 * Q - P * P)/3;
         B:= (2 * P * P * P - 9 * P * Q + 27 * R) / 27;
         X:= 0;

         if B <> 0 THEN begin
            A2:= B * B / 4 + A * A * A / 27;
            IF A2 > 0 THEN A2:= 0;
            A2:= -A2;
            D:= SQRT(A2);
            A3:= -B / 2;
            R2:= SQRT(A3 * A3 + D * D);
            IF A3 >= 0 THEN P1:= ARCTAN(D / A3)
                       else P1:= (PI) -ARCTAN(D / A3);
            R2:= EXP(LN(R2) / 3);
            P1:= P1 / 3;
            X:= R2 * COS(P1);
            X:= X * 2;
```

```
         end;

         ROOT[1]:= X - P / 3;
         Z:= (P + ROOT[1]) / 2;
         SP:= Z * Z + R / ROOT[1];
         SP:= ABS(SP);
         ROOT[2]:= -Z + SQRT(SP);
         ROOT[3]:= -Z - SQRT(SP);

         VEL[1]:= sqrt(ROOT[1] / DENS);
         VEL[2]:= sqrt(ROOT[2] / DENS);
         VEL[3]:= sqrt(ROOT[3] / DENS);
         UX:= (VEL[N] * COS(THETA));
         UY:= (VEL[N] * SIN(THETA));

         if N=1 then color:=yellow;
         if n=2 then color:=lightblue;
         if n=3 then color:=white;
           {COPIED}

      {TRANSPOSE OF L13}
         for l:=1 to 3 do begin
             L31[l,1]:=L13[1,l];
         end;

         for m:=1 to 3 do begin
            for l:=1 to 1 do begin
               EL31[m,l]:=0;
               for o:=1 to 3 do begin
                   EL31[m,l]:=EL31[m,l]+EP33[m,o]*L31[o,l];
               end;
            end;
         end;


DEN:=EL31[1,1]*L13[1,1]+EL31[2,1]*L13[1,2]+EL31[3,1]*L13[1,3];
         DEN:=DEN*0.008854;

         for m:=1 to 1 do begin
            for l:=1 to 6 do begin
               LE16[m,l]:=0;
               for o:=1 to 3 do begin
                   LE16[m,l]:=LE16[m,l]+L13[m,o]*E36[o,l];
               end;
            end;
         end;

         for l:=1 to 6 do begin
             EL61[l,1]:=LE16[1,l];
         end;

         for m:=1 to 6 do begin
            for l:=1 to 6 do begin
               CC66[m,l]:=0;
               for o:=1 to 1 do begin
                   CC66[m,l]:=CC66[m,l]+EL61[m,o]*LE16[o,l];
               end;
            end;
         end;
```

```
      DEN:=1/DEN;

      for m:=1 to 6 do begin
        for l:=1 to 6 do begin
          CC66[m,l]:=CC66[m,l]*DEN;
        end;
      end;

      for m:=1 to 6 do begin
        for l:=1 to 6 do begin
          CS66[m,l]:=C66[m,l]+CC66[m,l];
        end;
      end;

{NEW PART END}

      for m:=1 to 3 do begin
        for l:=1 to 6 do begin
          L63[l,m]:=L36[m,l];
        end;
      end;


     {COPY}
      for m:=1 to 6 do begin
        for l:=1 to 3 do begin
          CL63[m,l]:=0;
          for o:=1 to 6 do begin
             CL63[m,l]:=CL63[m,l]+CS66[m,o]*L63[o,l];
{_______CHANGE C66 INTO CS66 TO FIND THE DIFFERENT }
          end;
        end;
      end;

      for m:=1 to 3 do begin
        for l:=1 to 3 do begin
          T33[m,l]:=0;
          for o:=1 to 6 do begin
            T33[m,l]:=T33[m,l]+L36[m,o]*CL63[o,l];
          end;
        end;
      end;

      P:= -(T33[1, 1] + T33[2, 2] + T33[3, 3]);
      Q:= T33[1, 1] * T33[3, 3] + T33[1, 1] * T33[2, 2] + T33[2, 2]
* T33[3, 3];
      Q:= Q - (T33[2, 1]*T33[2, 1] + T33[2, 3]*T33[2, 3] + T33[3,
1]*T33[3, 1]);
      R:= T33[1, 1] * T33[3, 2]*T33[3, 2] + T33[3, 3]* T33[1,
2]*T33[1, 2] + T33[2, 2] * T33[1, 3]*T33[1, 3];
      R:= R - T33[1, 1] * T33[2, 2] * T33[3, 3] - 2 * T33[1, 2] *
T33[1, 3] * T33[2, 3];


      A:= (3 * Q - P * P)/3;
      B:= (2 * P * P * P - 9 * P * Q + 27 * R) / 27;
      X:= 0;
```

```
        if B <> 0 THEN begin
           A2:= B * B / 4 + A * A * A / 27;
           IF A2 > 0 THEN A2:= 0;
           A2:= -A2;
           D:= SQRT(A2);
           A3:= -B / 2;
           R2:= SQRT(A3 * A3 + D * D);
           IF A3 >= 0 THEN P1:= ARCTAN(D / A3)
                      else P1:= (PI) -ARCTAN(D / A3);
           R2:= EXP(LN(R2) / 3);
           P1:= P1 / 3;
           X:= R2 * COS(P1);
           X:= X * 2;
        end;

        ROOT[1]:= X - P / 3;
        Z:= (P + ROOT[1]) / 2;
        SP:= Z * Z + R / ROOT[1];
        SP:= ABS(SP);
        ROOT[2]:= -Z + SQRT(SP);
        ROOT[3]:= -Z - SQRT(SP);

        SVEL[1]:=sqrt(ROOT[1] / DENS);
        SVEL[2]:=sqrt(ROOT[2] / DENS);
        SVEL[3]:=sqrt(ROOT[3] / DENS);
        SX:= (SVEL[N] * COS(THETA));
        SY:= (SVEL[N] * SIN(THETA));
        A:=sX-uX; B:=sY-uY;
        delta:=sqrt(a*a+b*b);

       STIFF:=SQRT(SX*SX+SY*SY);
        kk:=2*delta/stiff;
        ktkt:=kk/(1+kk);
        kt:=sqrt(ktkt);
        if N=1 then color:=blue;
        if n=2 then color:=RED;
        if n=3 then color:=yellow;
        writeln(ofile,THETA*180/PI,'         ',kt);
        SYM(THETA*180/PI,kt,0);
     end;
   end;
 {COPY}

   color:=WHITE;
   gltext('Color represent:',18.5,16);
   color:=blue;
   gltext('Longitud',18.5,17);
   color:=red;
   gltext('Shear',18.5,18);
   color:=lightgreen;
   gltext('Shear',18.5,19);

   repeat until keypressed;
   closegraph;
   close(ofile);
END.
```

Appendix V: List of Publications

1. C.M. Lueng, H.L.W. Chan, C. Surya, W.K. Fong, C.L. Choy, P. Chow and M. Rosamond, 'Piezoelectric coefficient of GaN measured by laser interferometry', accepted by J. Non-crystalline Solids.

2. C.M. Lueng, H.L.W. Chan, C. Surya, W.K. Fong, and C.L. Choy, 'Piezoelectric coefficients of aluminum nitride and gallium nitride', accepted by Materials Reseach Society 1999 spring meeting.

3. C.M. Lueng, H.L.W. Chan, C. Surya and C.L. Choy, 'Piezoelectric coefficients of aluminum nitride and gallium nitride by laser interferometry', submitted to J. Appl. Phys.